Algerian Republic Democratic and Popular
Ministry of Higher Education and Scientific Research

UNIVERSITY OF RELIZANE
Faculty of Sciences and Technologies
Department of Electrical Engineering and
Automation

DOCTORAL THESIS 3rd cycle LMD

Major : Automation
Specialization : Automation

Mr MEGHRAOUI Mohamed Hamza

Thesis topic

OPTIMIZATION OF PARAMETERS FOR CLASSIFIERS IN THE ANALYSIS OF ARTERIAL PRESSURE WAVEFORMS

Before the jury composed of:

President	YSSAAD Benyssaad	Prof.	Univ. of Relizane
Thesis Director	BENAIRED Noreddine	MCA	Univ. of Relizane
Thesis Co-Director	BENSELAMA Zoubir Abdeslem	Prof	Univ. of Blida 1
Examiner	MELIANI Bouziane	MCA	Univ. of Relizane
Examiner	ALLAOUI Tayeb	Prof	Univ. of Tiaret
Examiner	TALEB Rachid	Prof	Univ. of Chlef

Academic year: 2023/2024

Dedication

In the name of Allah, Most Gracious, Most Merciful

To Allah be all praise and gratitude for blessing me with the ability and opportunity to complete this thesis. Truly all praise is due to Him, the Most High.

I dedicate this thesis to my family for their unwavering support throughout my academic journey. Thank you for encouraging me to pursue my dreams and for your constant prayers and guidance which have brought me to this day.

I also dedicate this work to my teachers and mentors who have invested their knowledge and wisdom in me. I am especially grateful to my advisors, Dr. Benaired and Pr. Benselama, whose support and expertise made this thesis possible.

Most of all, I dedicate this achievement to Maria. Your patience, kindness and words of encouragement meant the world to me during the challenges of this PhD journey. Thank you for standing by my side every step of the way and supporting me. This success is as much yours as it is mine.

It is with sincere appreciation and gratitude that I dedicate this thesis to all those who invested in me and never stopped encouraging me to fulfill my dreams. To Allah be all praise.

Acknowledgements

I would like to thank my supervisors Dr. Benaired and Dr. Benselama for their continuous guidance and support throughout this research. Their valuable feedback and insights were instrumental in improving the quality of this work. I am also grateful to the staff and faculty at the GIDD laboratory in Relizane University and the LATSI laboratory in Blida1 University for providing the necessary facilities and resources to conduct this research.

I acknowledge the Frepik platform (https://freepik.com) for allowing me to use their images under a Creative Commons license. Figures I.1-I.5 were adapted from images originally created by Servier Medical Art (https://creativecommons.org/licenses/by/4.0/). I would like to thank Servier for making their resources available under an open license.

Abstract

Rising global burden of cardiovascular disease (CVD) has spurred research exploring artificial intelligence (AI) and machine learning (ML) approaches for developing monitoring systems using biomedical signals. Photoplethysmography (PPG) has emerged as a viable biosensing option due to its non-invasive, affordable nature and inherent relationship to cardiovascular physiology. Current literature predominantly investigates two approaches - leveraging PPG signals to classify individuals at risk of CVD or to classify specific disease states. While generating high-performing ML classifiers, limitations remain in broad risk profiling or narrow disease classification for effective clinical translation. Clinical integration requires evidence-based predictions providing targeted insights to inform diagnostic plan formulation.

An underexplored solution lies in the analysis of arterial pressure waveforms, as CVDs are known to influence their morphology, leading to distinct abnormal arterial pulse (AAP) patterns. This thesis aims to leverage the combination of PPG signals and ML classifiers to identify abnormal arterial pressure waveform patterns that are predictive of specific AAP manifestations, thereby providing healthcare practitioners with more targeted diagnostic insights. To address the challenges in obtaining labeled clinical datasets of AAP waveforms, the work explores the use of the MIMIC-III database, which contains synchronous arterial blood pressure (ABP) and PPG recordings from intensive care unit patients.

The key methodological aspects of this research involve optimizing the classifiers' parameters through both internal and external optimization techniques. The internal optimization focuses on fine-tuning the classifiers' hyperparameters using Bayesian optimization approaches, which can efficiently explore the high-dimensional hyperparameter space to identify optimal configurations. In parallel, the external optimization techniques aim to enhance the input predictors by extracting physiologically meaningful parameters from the PPG signals. This includes the application of dimensionality reduction methods, such as transformation-based techniques and metaheuristic optimization algorithms, to compress the feature space while preserving the most informative characteristics. Additionally, feature importance analysis is employed to identify the most relevant input predictors for the classification tasks.

This dual-pronged approach of internal and external optimization aimed at enhancing the classifiers' performance in predicting both AAP patterns and blood pressure (BP) levels, addressing the prevalent issues of CVD and hypertension. Abnormal arterial pulses were first identified by referencing pathological examples, while BP levels followed clinical guidelines. Various ML classifiers are empirically evaluated to classify these variables, with some providing impressive performances attaining 100% accuracy. The proposed system is designed to be applicable for both clinical integration and consumer-oriented applications, with the former focusing on physiologically-relevant parameters and the latter emphasizing efficient and less complex preprocessing requirements for wearable device integration.

Overall, this thesis presents a comprehensive framework for developing efficient PPG-based classifiers. Results suggest potential for convenient clinical-grade blood pressure monitoring beyond healthcare settings. Additionally, the system shows clinical potential as a non-invasive, cost-effective solution for applications such as doctor-assisted diagnosis, remote post-surgery monitoring, nursing alerts, and personalized health management through timely notifications, addressing needs while reducing the risks of current invasive practices.

Keywords: *Abnormal arterial pulse pattern, Artificial intelligence, Blood pressure, Classification, Machine learning, Optimization, Photoplethysmography, Arterial pressure.*

Résumé

Le fardeau mondial croissant des maladies cardiovasculaires (MCV) a stimulé la recherche explorant les approches d'intelligence artificielle (IA) et d'apprentissage automatique (AA) pour développer des systèmes de surveillance utilisant des signaux biomédicaux. La photopléthysmographie (PPG) est apparue comme une option de biodétection viable en raison de son caractère non invasif, abordable et de sa relation inhérente avec la physiologie cardiovasculaire.

La littérature actuelle explore principalement deux approches concernant l'exploitation des signaux PPG pour : classer les individus à risque de MCV, classer des états pathologiques spécifiques. Bien que ces approches aient généré des classifieurs AA performants, des limites subsistent dans le profilage général du risque ou la classification étroite des maladies pour une translation clinique efficace. L'intégration clinique nécessite des prédictions fondées sur des preuves fournissant des informations ciblées pour éclairer la formulation du plan de diagnostic.

Une solution peu explorée réside dans l'analyse des formes d'onde de pression artérielle, car les MCV sont connues pour influencer leur morphologie, entraînant des motifs d'impulsion artérielle anormale (IAA) distincts. Cette thèse vise à exploiter la combinaison des signaux PPG et des classifieurs AA pour identifier les motifs anormaux des formes d'onde de pression artérielle qui sont prédictifs de manifestations spécifiques d'IAA, offrant ainsi aux praticiens de santé des informations diagnostiques plus ciblées.

Les principaux aspects méthodologiques de cette recherche impliquent l'optimisation des paramètres des classifieurs par des techniques d'optimisation interne et externe. L'optimisation interne se concentre sur l'ajustement fin des hyperparamètres des classifieurs à l'aide de l’approche d'optimisation bayésienne. En parallèle, les techniques d'optimisation externe visent à améliorer les prédicteurs d'entrée en extrayant des paramètres physiologiquement significatifs des signaux PPG. Cela comprend l'application de méthodes de réduction de dimensionnalité, telles que les techniques basées sur la transformation et les algorithmes d'optimisation méta-heuristiques.

Cette approche à double volet d'optimisation interne et externe vise à améliorer les performances des classifieurs dans la prédiction des motifs IAA et des niveaux de pression artérielle (PA), abordant ainsi les problèmes répandus des MCV et de l'hypertension. Divers classifieurs AA sont évalués de manière empirique pour classer ces variables, certains atteignant des performances impressionnantes de 100% de précision.

Dans l'ensemble, cette thèse présente un cadre complet pour développer des classifieurs efficaces basés sur la PPG. Les résultats suggèrent un potentiel pour une surveillance pratique de la pression artérielle de niveau clinique au-delà des paramètres de soins de santé. De plus, le système montre un potentiel clinique en tant que solution non invasive et rentable pour diverses applications médicales.

Mots clés : *Apprentissage automatique, Intelligence artificielle, Motif d'impulsion artérielle anormale, Optimisation, Photopléthysmographie, Pression artérielle, Classification*

الخلاصة

أدى العبء العالمي المتزايد لأمراض القلب والأوعية الدموية إلى تحفيز البحوث التي تستكشف أساليب الذكاء الاصطناعي والتعلم الآلي لتطوير أنظمة المراقبة باستخدام إشارات طبية حيوية. برز مقياس موجة الضوء الكهربائية كخيار قابل للحياة للاستشعار الحيوي بسبب طبيعته غير الجراحية وميسورة التكلفة وعلاقته الضمنية بالفسيولوجيا القلبية الوعائية.

تستكشف الأدبيات الحالية بشكل أساسي اتجاهين - استغلال إشارات موجة الضوء الكهربائية لتصنيف الأفراد المعرضين لخطر أمراض القلب والأوعية الدموية أو لتصنيف حالات مرضية محددة. على الرغم من أنها ولّدت مصنفات التعلم الآلي ذات أداء عالٍ، لا تزال هناك قيود في التنميط العام للخطر أو التصنيف الضيق للأمراض من أجل الترجمة السريرية الفعالة. تتطلب التكامل السريري توقعات مستندة إلى أدلة توفر رؤى موجهة لإعلام صياغة خطة التشخيص.

تكمن إحدى الحلول التي لم يتم استكشافها في تحليل أشكال موجة ضغط الشرايين، حيث من المعروف أن أمراض القلب والأوعية الدموية تؤثر على تشكيلها، مما يؤدي إلى أنماط نبضات شرايين شاذة متميزة. تهدف هذه الأطروحة إلى الاستفادة من الجمع بين إشارات موجة الضوء الكهربائية ومصنفات التعلم الآلي لتحديد أنماط شكل موجة ضغط الشرايين الشاذة التي يمكن التنبؤ بها لتجليات أنماط نبضات شرايين المحددة، وبالتالي توفير ممارسي الرعاية الصحية بمعلومات تشخيصية موجهة بشكل أكبر.

تنطوي الجوانب المنهجية الرئيسية لهذا البحث على تحسين معلمات المصنفات من خلال تقنيات التحسين الداخلية والخارجية. يركز التحسين الداخلي على الضبط الدقيق لمعلمات المصنف باستخدام نهج تحسين بايزي. في الوقت نفسه، تهدف تقنيات التحسين الخارجية إلى تحسين المتنبئات الداخلية من خلال استخراج معلمات ذات معنى فسيولوجي من إشارات موجة الضوء الكهربائية.

هذا النهج ثنائي الأوجه للتحسين الداخلي والخارجي يهدف إلى تعزيز أداء المصنفات في التنبؤ بأنماط نبضات الشرايين الشاذة ومستويات ضغط الدم، مما يعالج المشاكل السائدة لأمراض القلب والأوعية الدموية وارتفاع ضغط الدم. يتم تقييم تجريبي لمجموعة متنوعة من مصنفات التعلم الآلي لتصنيف هذه المتغيرات، مع بعض الأداء المبهر الذي يصل إلى دقة 100٪.

بشكل عام، تقدم هذه الأطروحة إطاراً شاملاً لتطوير مصنفات فعالة قائمة على موجة الضوء الكهربائية .تشير النتائج إلى إمكانات للرصد العملي لضغط الدم بمستوى سريري خارج إعدادات الرعاية الصحية. علاوة على ذلك، يُظهر النظام إمكانات سريرية كحل غير جراحي وفعال من حيث التكلفة لتطبيقات مثل التشخيص المساعد من قبل الطبيب والمراقبة عن بُعد بعد الجراحة والتنبيهات التمريضية وإدارة الصحة الشخصية من خلال إشعارات في الوقت المناسب، مما يعالج الاحتياجات مع تقليل المخاطر الناجمة عن الممارسات الجراحية الحالية.

كلمات مفتاحية : نمط نبضات الشريان غير الطبيعي، الذكاء الاصطناعي، ضغط الدم، التصنيف، التعلم الآلي، التحسين، مقياس موجة الضوء الكهربائية، ضغط الشريان.

Table of Contents

List of Figures

List of Tables

List of Abbreviations

AAP: *Abnormal Arterial Pulse*

ABP: *Arterial Blood Pressure*

ACC: *Accuracy*

ABI: *Ankle Brachial Index*

ANN: *Artificial Neural Network*

APG: *Acceleration Photoplethysmography*

AR: *Aortic Regurgitation*

ARMAX: *AutoRegressive Moving Average model with eXogenous inputs*

AS: *Aortic Stenosis*

AV: *Atrioventricular*

BDP: *Bounding Pulse*

BHS: *British Hypertension Society*

BLSTM: *Bidirectional Long Short-Term Memory*

BP: *Blood Pressure*

BT: *Bagged Decision Trees*

CAD: *Coronary Artery Disease*

CHD: *Coronary Heart Disease*

CNN: *Convolutional Neural Network*

CO: *Cardiac Output*

CPU: *Central Processing Unit*

CWT: *Continuous Wavelet Transform*

CVD: *Cardiovascular Disease*

DBP: *Diastolic Blood Pressure*

DNL: *Dicrotic Notch Level*

DNN: *Deep Neural Network*

DWA: *Dicrotic Wave Level*

DL: *Deep Learning*

DT: *Decision Tree*

EHR: *Electronic Health Record*

ELM: *Extreme Learning Machine*

FN: *False Negative*

FP: *False Positive*

FFT: *Fast Fourier Transform*

FSST: *Fourier Synchrosqueezed Transform*

FRV: *Feature Redundancy Vote*

GMM: *Gaussian Mixture Model*

GP: *Gaussian Process*

GPU: *Graphics Processing Unit*

HF: *Heart Failure*

HOCM: *Hypertrophic Obstructive Cardiomyopathy*

HR: *Heart Rate*

HS: *Harmonic Search*

HT: *Hypertension*

ICU: *Intensive Care Unit*

JNC7: *Seventh Report of the Joint National Committee on Prevention, Detection, Evaluation, and Treatment of High Blood Pressure*

JNP: *Jugular Venous Pulse*

KNN: *k-Nearest Neighbors*

LDA: *Linear Discriminant Analysis*

LR: *Linear Regression*

LSTM: *Long Short-Term Memory*

LMTD: *Local Minimum of the Third Derivative*

MAE: *Mean Absolute Error*

MAP: *Mean Arterial Pressure*

MATLAB: *Matrix Laboratory*

MI: *Medical Imaging*

MIMIC: *Medical Information Mart for Intensive Care*

ML: *Machine Learning*

MLP: *Multi-Layer Perceptron*

MRMR: *Minimum Redundancy Maximum Relevance*

MSE: *Mean Squared Error*

NT: *Normotension*

OPT: *Onset to Peak Time*

PAD: *Peripheral Arterial Disease*

PAP: *Pulse Arterial Pressure*

PAT: *Pulse Arrival Time*

PP: *Pulse Pressure*

PPG: *Photopletysmograghy*

PPT: *Peak to Peak Time*

PHT: *Prehypertension*

PR: *Precision*

PR: *Pulse Rate*

PTT: *Pulse Transit Time*

PVR: *Pulse Rate Variability*

RAM: *Random-Access Memory*

RR: *Respiratory Rate*

RF: *Random Forrest*

RGB: *Red Green Blue*

SA: *Sinoatrial*

SD: *Standard Deviation*

SDC: *Streaming Data Collection*

SE: *Sensitivity*

SBP: *Systolic Blood Pressure*

SOM: *Self-organizing map*

SP: *Specificity*

SQ: *Signal Quality*

SQI: *Signal Quality Index*

SSQI: *Skewness Signal Quality Index*

ST: *Systolic Time*

STFT: *Short-time Fourier Transform*

STT: *Slope Transit Time*

STD: *Standard Deviation*

SV: *Stroke Volume*

SVM: *Support Vector Machines*

SVR: *Systemic Vascular Resistance*

TCPD: *Traditional Chinese Pulse Diagnosis*

TCM: *Traditional Chinese Medicine*

TF: *Time-frequency*

TFR: *Time-Frequency Reassignment*

TN: *True Negative*

TP: *True Positive*

UCB: *Upper Confidence Bound*

UT: *Upstroke Time*

VHD: *Valvular Hear Disease*

WHO: *World Health Organization*

WHP: *Water Hammer Pulse*

XAI: *Explainable Artificial Intelligence*

Research Introduction

Cardiovascular disease (CVD) poses a major global health challenge, accounting for over 17.9 million annual deaths worldwide according to the WHO [1]. The scale of this burden is projected to increase substantially if left unaddressed, as CVD often presents with mild, gradually worsening symptoms that can sometimes remain hidden until sudden cardiac arrest [2,3]. Early and precise detection is critically important to motivate lifestyle modifications and clinical intervention when required [4]. However, clinically diagnosing CVD presents difficulties due to heterogeneous and non-specific symptoms, leading to diagnostic delays and consequently poorer prognoses [5,6]. Furthermore, the standard methods for diagnosing CVDs are limited in terms of specificity and sensitivity, potentially leading to erroneous positive identifications [5]. Outside of clinical settings, the asymptomatic nature of CVD [7] poses additional challenges for management as affected individuals have no impetus to pursue medical care. Hence, to adequately address CVD management concerns both within and outside of clinical environments, healthcare must leverage advanced digital technologies, such as automated systems powered by AI. With such innovative solutions, we could help shorten time to accurate diagnosis and treatment, as well as uncover undiagnosed "occult" cases of CVD among asymptomatic populations.

Advances in ML have opened up new avenues for more proactive, predictive approaches to CVD screening, detection, and clinical management [8]. ML algorithms possess the capacity to integrate diverse biomedical data streams, including EHRs [9], MI [10] and test results [11], treatment plans [12], biosensor outputs [13], and genetic profiles [14]. The ability of ML to process and extract insights from such multifaceted data holds immense potential for early CVD prediction. Notably, bio-signal data such as ECGs and PPGs have demonstrated promise for non-invasive CVD prediction when combined with ML models [15]. Studies have validated ML's effectiveness in classifying CVD status using these physiological signals, with high-performing systems developed for conditions like myocardial infarction, arrhythmias, CHD, CAD, cardiopathies, and aneurysms [16-21]. Additionally, other ML-based approaches have been designed to identify at-risk individuals [22-24], by leveraging PPG signals and associated respiratory events, such as rebreathing, heart rate variability, and sleep apnea [25].

Noninvasive cardiovascular profiling utilizing physiological signals fosters opportunities for earlier clinical intervention when treatment efficacy is optimal. However, prioritizing predictive performance exclusively may undermine the clinical utility of such systems, as enhancing healthcare delivery requires considerations beyond classification accuracy alone

[26]. For such systems to meaningfully augment medical services, the following questions warrant examination:

(1) *By what mechanisms could these systems potentially aid physicians in screening and risk appraisal procedures? What technical and applied barriers remain to be addressed in order to realize their full clinical potential?*

(2) *To what extent can clinical judgement be made independently of model transparency? Which approaches may engender confidence in such systems among healthcare practitioners?*

(3) *Under prevailing methodologies, what typical elements inform AI model structure for CVD classification? Do conventional optimization strategies sufficiently facilitate the explainability and transparency intrinsic to healthcare decision contexts?*

The former inquiries address the predictive capacity of these systems. Models focused on singular disease classification in [18-21] may serve to corroborate diagnoses or refine risk profiles, yet their utility for comprehensive initial screening is limited. A classifier capable of discerning multiple potential conditions would offer a holistic perspective and guiding insights regarding the spectrum of possible CVDs. Conversely, models addressing general CVD risk in [22-24] offer constrained etiological insights to inform clinical decision-making processes. These approaches typically rely on datasets designed using observable respiratory events like rebreathing, heart variability, and apnea [25]. The inherent diversity and lack of disease-specificity of such signs can complicate the prognostic process and delay accurate diagnosis [6]. Overall, an overemphasis on single-disease output or generalized risk profiling may restrict the clinical utility and real-world applicability of these emerging technologies.

From a clinical perspective, the optimal system would possess the capacity for both broad screening and nuanced risk profiling, through evidence-based inputs and outputs. An unexplored solution lies in targeting ABP waveforms. Cardiovascular pathophysiology is known to influence ABP morphology, altering the normal pulse wave pattern. Different AAPs have been shown to correlate with specific cardiovascular conditions [27-29], presenting an opportunity to empower clinicians with a multimodal diagnostic system. Additionally, hypertension's prevalence and associated mortality risk [30,31], coupled with its effects on pulse wave morphology, further underscore the clinical utility of developing robust AAP classification capabilities. However, realizing this potential requires the non-invasive classification of AAPs through high-fidelity input signals. PPG offers a convenient, non-

invasive biosensing solution due to the close correlation between ABP and PPG signals [32]. PPG data can provide insights into cardiovascular mechanisms [33], enabling ML algorithms to characterize patterns indicative of specific AAP manifestations. Nevertheless, the lack of pre-identified AAP datasets poses challenges [26], likely due to the inherent risks of ABP measurement [34]. This constraint has limited current literature to estimating BP trends [35] and classifying hypertension [36] via these signals.

The subsequent inquiries address the imperative of clinical decision-making transparency. Evidence-based medical practice depends on a comprehensive understanding of underlying pathophysiology, rather than the sole consideration of model outputs [37]. Irrespective of whether a system is designed to predict specific diseases or general risk levels, a lack of explicability regarding its input predictors constrains its real-world applicability within clinical settings. Garnering acceptance and trust within the medical community necessitates the provision of more targeted, interpretable insights into the probable etiological factors driving the model's predictions. However, extant studies may inadvertently overemphasize system performance at the expense of transparency. For instance, employing complex optimization techniques on PPG signals to extract input features, as in [22, 23], is clinically irrelevant. What is truly needed are features that are physiologically meaningful and aligned with the clinician's understanding of cardiovascular pathologies, rather than perfect dimensionally reduced representations.

Other key aspects for clinical transparency include algorithm architecture and parameter optimization, as emphasized by the latter inquiries. Within healthcare applications, explainability is of paramount importance [37]. Algorithms exhibiting more transparent architectures are preferable for XAI researchers exploring the logic and reasoning of clinical AI models. Selecting ML methods that maintain a certain level of interpretability allows better evaluation of functionality. However, current researches lack well-defined criteria for selecting less complex AI algorithms, often trading off interpretability for higher performance metrics. Furthermore, common optimization approaches focus solely on maximizing accuracy [22], regardless of model complexity. Thus, exploring alternative optimization strategies to manage this interpretability-performance equilibrium represents a critical frontier in advancing the clinical utility of AI-powered systems.

This tension between predictive performance and model simplicity poses a significant challenge in the development of clinically viable ML classification systems. Failure to address

the disconnect between technical optimization and clinical relevance may relegate these innovative technologies to the periphery of clinical decision-making. However, it is reasonable to assume that the use of these systems outside the clinic could undermine the need to address this clinical transparency/system performance trade off. For example, by deploying high-performing models on personal health tracking devices like smart watches and wristbands, could enable asymptomatic individuals to self-screen for CVDs and hypertension anytime, anywhere. This would help drive earlier detection and improved public health outcomes on a global scale, without requiring the same level of clinical transparency expected in a medical context.

To address barriers limiting widespread cardiovascular management, this research aims to develop and validate a non-invasive classification system capable of integrating into affordable devices. Suitable ML classifiers will be explored to create a system able to predict key cardiovascular biomarkers, including systolic/diastolic blood pressure, hypertension status as well as identification of distinct AAP morphologies, all through non-invasive PPG signal analysis. This work seeks to address common limitations of existing approaches that have constrained the clinical translation and successful device implementation of such technologies, including:

- *Complex preprocessing requirements for features extraction.*
- *Clinically irrelevant features extraction.*
- *Lack of generalizability due to limited datasets.*
- *Suboptimal handling of training data.*
- *Improperly optimized parameters or model architectures.*
- *Significant time and computational resources required for model training.*

Specific objectives to overcome these barriers are summarized as follows:

Expanded and Diverse Dataset: Prior research in this field has often relied on relatively small and narrow datasets, limiting the generalizability and predictive performance of resulting AI models. To address this, the present study plans to collect and employ a substantially larger and more diverse dataset during model development and evaluation compared to earlier work, ensuring inclusion of varied systolic, diastolic pressures and types of AAP waveforms. Exposing the AI models to such a breadth of examples during training is expected to reduce potential biases and overfitting while strengthening classification reliability for novel cases compared to alternatives developed from narrow, less inclusive datasets. This enhanced

representation of real-world variability aims to produce more robust and translatable AI solutions.

Addressing motion artefacts: While PPG-based monitoring shows promise, signal quality can degrade due to motion-induced noise [38], confounding cardiovascular parameter extraction. To minimize this motion interference, an automatic rejection system will be created to eliminate corrupted signals.

Feature engineering for Clinical and Consumer Applications: Extracting features for clinical versus consumer-oriented applications requires distinct design considerations. From a clinical standpoint, deriving meaningful physiological features is paramount. However, PPG waveform morphologies exhibit inherent instability, necessitating precise signal processing. Therefore, custom detectors will be created and optimized to locate clinically important waveform characteristics, generating more stable inputs for the proposed classifier [26]. Conversely, these complex analytical methods may be less critical for personal health monitoring applications, as the user's primary concern is identifying potential health risks early, rather than dissecting the algorithmic logic. As such, this work will investigate time-frequency signal processing techniques to characterize dynamic PPG changes obscured from view with conventional methods. Engineering features capturing information in time-varying spectral content is expected to provide novel insights beyond basic waveform analyses [36].

Computational Efficiency: Dealing with large datasets usually prompts a preference for DL algorithms over ML due to their ability to handle complex and high-dimensional data [39]. However, this flexibility demands major computational resources for training and inference. Deep neural networks have substantial storage needs [40], due to the large number of weight parameters and requires expensive high-RAM GPUs to process their computationally intensive activation layers during prediction. This level of specialized hardware makes deploying DL models on resource-constrained wearable devices infeasible for most users. In contrast, ML training involves less complex optimization of fewer learned variables, allowing for use of basic processors. Trained ML models essentially comprise hyperparameters needing nominal storage. This research therefore aims to investigate computationally efficient ML techniques as an enabler of developing an affordable, clinically meaningful BP monitoring solution deployable directly through consumer-grade wearables.

AAPs Modelling: The identification of AAPs poses a challenge due to the absence of clear guidelines and need for comprehensive understanding of their waveform characteristics [26].

This research aims to present novel approaches and benchmarks to assist in modeling AAPs. Developing techniques specifically targeted towards AAP patterns has potential to advance understanding of underlying cardiovascular conditions.

Multi-objective Hyperparameter Optimization: The efficacy of ML models is heavily contingent on the appropriate hyperparameter selection. This research endeavors to apply Bayesian optimization [41] to systematically tune the classifier's internal hyperparameters. Studies reported the effectiveness of Bayesian optimization algorithm in outperforming other algorithms like random search or grid search [42]. Thus, it is anticipated that automated optimization through Bayesian theorem will develop models with enhanced predictive performance relative to arbitrary hyperparameter configurations. However, developing clinically viable ML classifiers necessitates formulating a multi-objective optimization problem considering model performance and interpretability. Potential solutions include:

- *Prioritizing inherently transparent model architectures that provide intelligible insight into the logic underlying cardiovascular assessments.*
- *Incorporating XAI methods, such as feature importance analysis to identify impactful input variables.*
- *Analyzing dynamic cardiac cycles within PPG signals to boost classification without compromising model simplicity.*

The growing global burden of CVD necessitates innovative solutions to enable earlier detection, both within clinical environments and on a population scale. ML has demonstrated promising advancements in cardiology through non-invasive techniques, such as PPG signal analysis. However, existing approaches remain limited by technical barriers that impede widespread clinical adoption and real-world application through consumer devices. This research aims to develop an optimized cardiovascular risk assessment and management system that targets these limitations. The key objective is to enable the non-invasive identification of various pressure-related abnormalities from PPG signals alone, going beyond the predominant focus on estimating ABP waveforms. This approach introduces a novel means of characterizing pathological hemodynamic phenotypes for improved CVD assessment.

By leveraging the ubiquity of PPG signals, this research endeavors to create an affordable and accessible solution that can be seamlessly integrated into consumer-grade wearable devices. Additionally, the research's emphasis on addressing the tension between model performance and interpretability is crucial for the successful clinical adoption of AI-powered cardiovascular

decision support tools. The proposed multi-objective optimization strategies and the incorporation of domain-specific knowledge to derive clinically relevant features and model AAP patterns are key steps towards bridging the gap between technical advancements and practical clinical utility. Moreover, the research's focus on expanding and diversifying the dataset, as well as developing robust signal processing techniques, aims to enhance the generalizability and reliability of the proposed ML models.

Overall, this research represents a significant stride towards realizing the full potential of ML-based technologies in revolutionizing CVD management. By addressing the technical, clinical, and translational barriers that have hindered the widespread adoption of such solutions, the proposed work promises to have a transformative impact on the early detection, risk assessment, and personalized care of cardiovascular conditions.

Thesis Structure

The present thesis is structured as follows to provide a systematic exploration of the research endeavor, guiding the reader through a logical progression from the foundational understanding of cardiovascular mechanisms to the development, evaluation, and practical implications of the proposed arterial pressure classification system:

Chapter I: *Understanding Blood Pressure Behavior in Health and Cardiovascular Pathology*

This opening chapter offers a comprehensive overview of the human cardiovascular system and its influence on blood pressure. It delves into the conventional blood pressure measurement techniques and their inherent limitations, setting the stage for the subsequent investigation of alternative approaches. Additionally, the chapter examines the emerging role of AI in enhancing the accuracy and accessibility of blood pressure assessment, underscoring the motivations behind the current research.

Chapter II: *Optimizing Arterial Blood Pressure-Based Risk Profiling*

Building upon the foundational knowledge established in the previous chapter, ***Chapter II*** *focuses on analyzing existing classification schemes for cardiovascular conditions. It then proceeds to formulate the experimental plan for the proposed classification system, outlining the research objectives, hypotheses, and the overall experimental design.*

Chapter III: *Operationalizing an Upgraded Classification Framework*

Guided by the experimental plan, this chapter introduces the proposed methodology, detailing the processes of data acquisition, pulse wave feature detection, AAP modeling, feature engineering, dataset creation, and the ML experiments conducted. This chapter elucidates the technical approaches employed to address the research objectives, laying the groundwork for the subsequent analysis and discussions.

Chapter IV: *Classification Approach Assessment and its Implications for Applied Health Management.*

The penultimate chapter presents the experimental results, provides in-depth analysis of the ML modeling process, and discusses the key findings. Importantly, comparisons are drawn between the current approach and prior related methods, allowing for a comprehensive evaluation of the research contributions. Furthermore, this chapter explores the clinical implications of the study, including potential medical applications, system integration opportunities, and the challenges associated with translating the research outcomes into practical solutions.

Conclusions: *Summarizing Contributions, Limitations, and Future Directions*

Finally, the thesis concludes with a summary of the main contributions, an acknowledgment of the limitations, and an outline of potential directions for future work. This final section serves to consolidate the research findings, reflect on the progress made, and inspire further investigations in the pursuit of innovative cardiovascular monitoring solutions.

Chapter I

Understanding Blood Pressure Behavior in Health and Cardiovascular Pathology

Conventional Monitoring Strategies and the Prospect of AI-Driven Care

1. Overview of the Human Cardiovascular System

1.1. Cardiovascular Anatomy and Architecture

The cardiovascular system, or circulatory system, acts as the body's transport network, circulating blood and its contents throughout the entire human body [43]. Principally, it is responsible for distributing oxygenated blood, nutrients, hormones, carbon dioxide and metabolic waste products between the tissues and organs [44]. Blood comprises various cellular components including red blood cells which carry oxygen, white blood cells integral to immune function, platelets aiding hemostasis, as well as plasma consisting of water, proteins, and electrolytes [45]. Of note, red blood cells facilitate oxygen transport from the lungs to peripheral tissues whilst simultaneously removing carbon dioxide created during cellular respiration for exhalation [44]

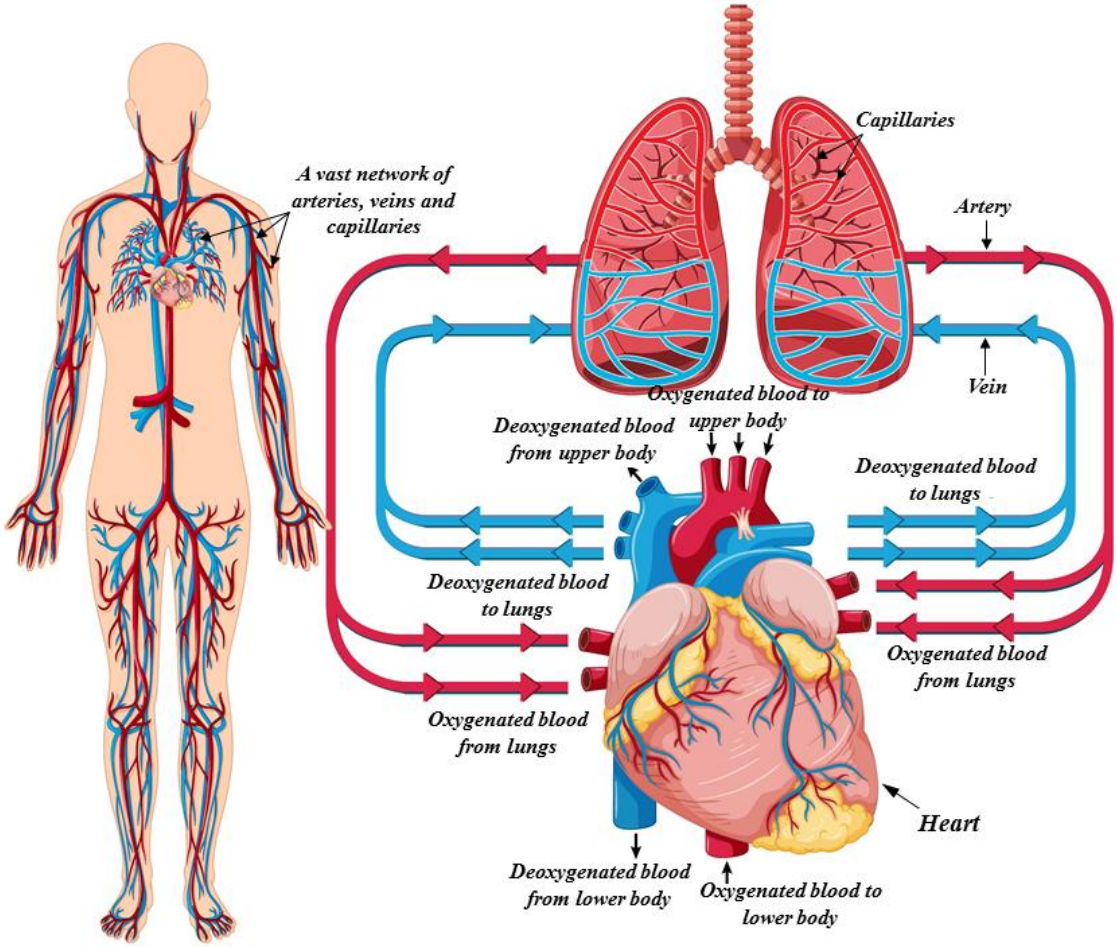

Figure I.1. Blood circulation

Major anatomical structures of this system include the heart which pumps blood, and a network of arteries, veins and capillaries that carry blood (**Figure I.1**). The heart pumps oxygen-rich blood to all parts of the body through arteries, and oxygen-depleted blood is

returned to the heart via veins [46]. Tissues are supplied with blood through a vast network of microscopic capillaries that branch out from arteries into every organ and cell (**Figure I.2**). Through coordinated interactions between its structural and cellular components, the cardiovascular system ensures adequate delivery of oxygen and substrates to sustain cellular metabolism throughout the body's tissues and organs. This supports homoeostatic functions necessary for health, growth, and repair. Derangements to any components within this integrated circulatory infrastructure can impair cardiovascular function and compromise systemic homeostasis if left unaddressed. A deeper understanding of normal cardiovascular physiology as well as pathological disease mechanisms remains integral to improving clinical outcomes.

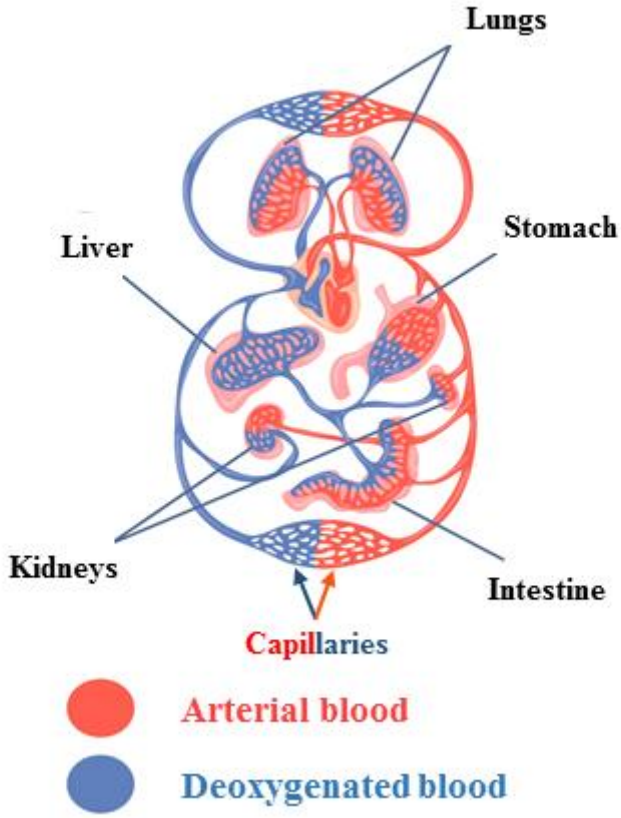

Figure I.2. Organs blood supply

1.2. Heart function

As illustrated in **Figure I.1**, the human heart functions as a dual-pump system, directing blood flow throughout the cardiovascular system. It is divided into right and left sides, with the right side receiving deoxygenated blood and pumping it to the lungs, while the left side receives oxygenated blood from the lungs and pumps it to the body. The heart's primary role is to continuously pump blood via precisely coordinated contractions, occurring about 70 times per

minute across four chambers [47]. The cardiac cycle consists of systole, when the heart contracts to eject blood, and diastole, when the heart relaxes and fills with returning blood (**Figure I.3**).

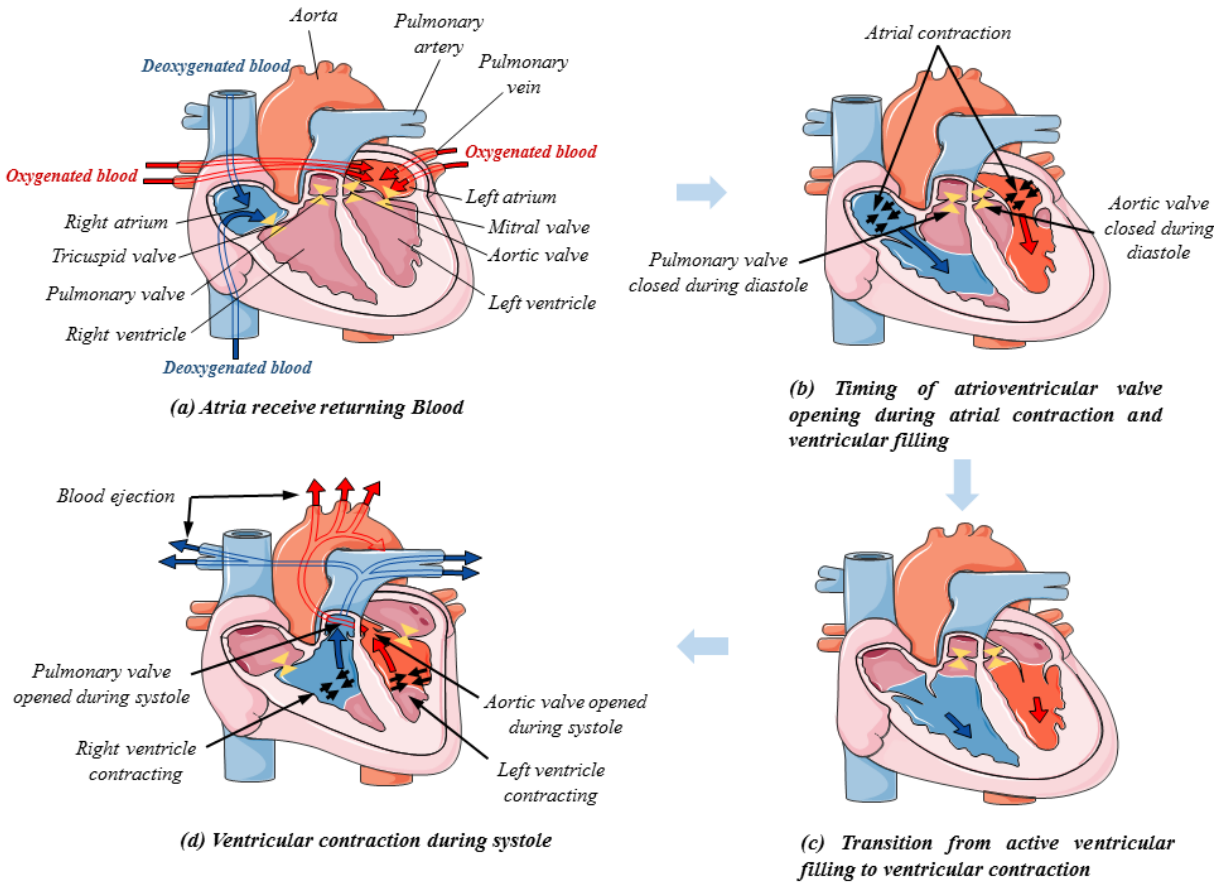

Figure I.3. Cardiac cycle of the heart

Specifically, during systole, atrial contraction propels blood into the relaxed ventricles. Ventricular contraction then rapidly increases intraventricular pressure [48], forcefully ejecting blood into the pulmonary and systemic arteries. As ventricular relaxation commences diastole, the atrioventricular valves reopen, and atrial contraction further fills the ventricles. Through this precisely timed sequence of contractions and relaxations, the heart maintains a consistent CO of around 5-6 liters per minute [49], ensuring adequate blood flow and tissue perfusion throughout the body.

1.2.1. The function and significance of heart valves

The four heart valves - the tricuspid, mitral, pulmonary, and aortic valves - are essential for regulating unidirectional blood flow through the cardiovascular system by opening and closing in coordination with the cardiac cycle [44]. The atrioventricular valves (tricuspid and mitral) separate the atria and ventricles, opening passively during ventricular diastole to allow

blood flow, and closing during systole to prevent backflow. The semilunar valves (pulmonary and aortic) are situated at the exits of the ventricles, opening when ventricular pressure exceeds arterial pressure to allow outflow.

Proper valve function, driven by the dynamic pressure gradients across the heart, is critical for optimizing the heart's pumping efficiency and matching blood flow to metabolic needs. Valve dysfunctions like stenosis or regurgitation can disrupt hemodynamics, leading to volume overload, compensatory cardiac remodeling, and eventual heart failure if left untreated [50,51]. Understanding the mechanics and pathologies of the cardiac valves is essential for managing various cardiovascular disorders and optimizing the heart's performance as the central circulatory pump.

1.2.2. Conduction System of Heart

The heart has a specialized electrical conduction system that coordinates the contractions of the four cardiac chambers (**Figure I.4**). The SA node, located in the right atrium, acts as the heart's natural pacemaker, generating electrical impulses around 70 beats per minute [52]. These impulses spread rapidly through the atrial walls, causing the atria to contract. The AV node then intentionally delays the propagation of the signals, allowing time for the ventricles to fill with blood before contracting. The impulses then travel down the bundle of His, into the right and left bundle branches, and ultimately through the extensive Purkinje fiber network within the ventricular myocardium. This organized conduction system facilitates the synchronized contraction of the ventricles.

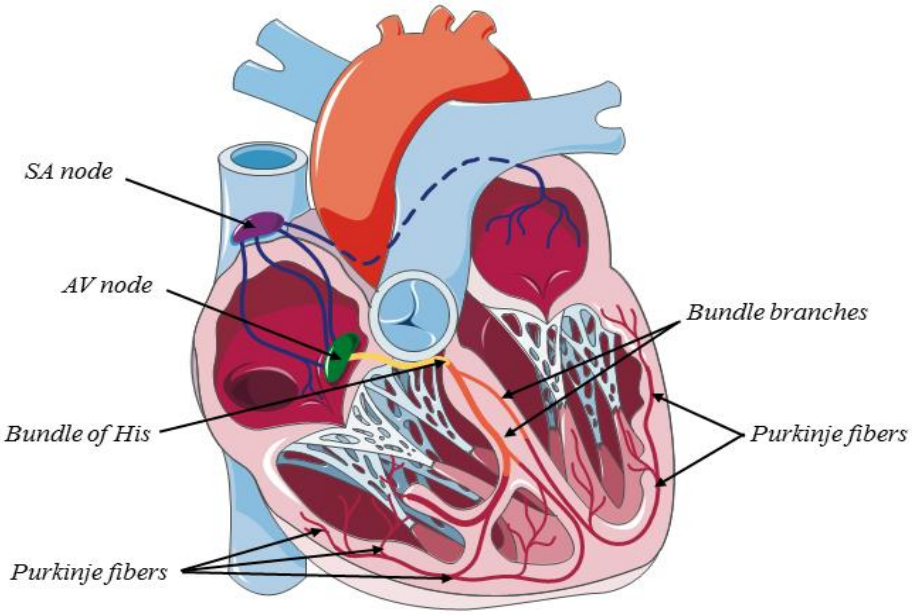

Figure I.4. Heart conduction system

The coordinated electrical activity of the heart's pacemaking and conduction tissues can be noninvasively monitored using an ECG, which provides insights into the sequential depolarization and repolarization of the cardiac chambers [44]. Disturbances in the timing or morphology of the ECG waveforms can indicate underlying conduction abnormalities [53]. Proper function of the heart's electrical conduction system is essential for maintaining the heart's efficient pumping rhythm. Disruptions can lead to cardiac arrhythmias. **Figure I.5** illustrates the normal waveform characteristics of an ECG signal during a single cardiac cycle.

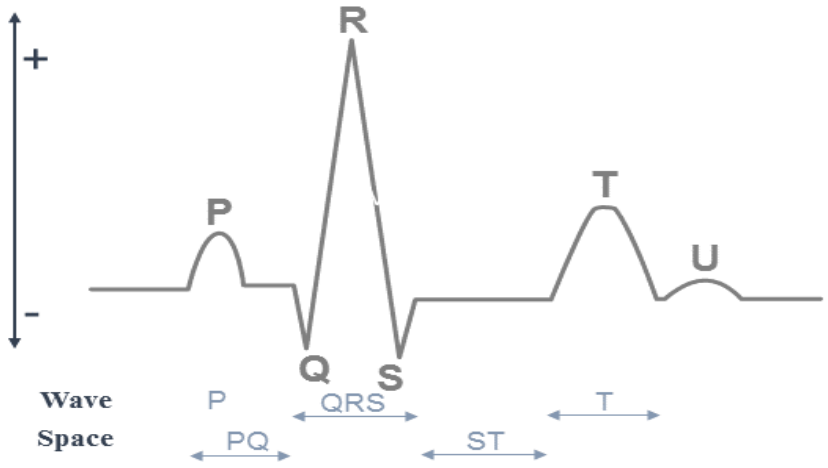

Figure I.5. Normal ECG waveform

1.3. Arterial network

1.3.1. Structure

The human body's arterial network (**Figure I.6)** is an intricate system that originates from the heart and branched vessels that deliver oxygenated blood to the various tissues and organs throughout the body. At the center of this network lies the aorta, the largest and most proximal artery in the body, which emerges from the left ventricle of the heart and serves as the primary conduit for distributing blood. Branching off from the aortic arch are the major, or central, arteries responsible for supplying blood to specific regions of the body. For instance, the carotid arteries branch off the aortic arch and travel up the neck to deliver blood to the head and brain, while the subclavian arteries also branch off the aortic arch and eventually give rise to the brachial and radial arteries that supply the upper limbs.

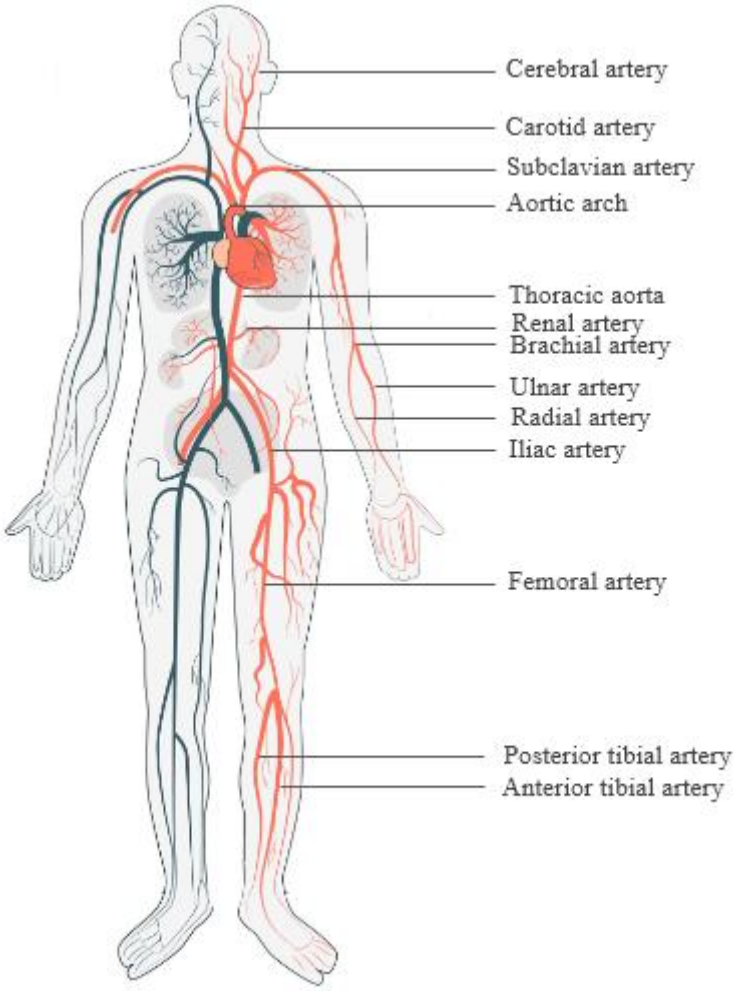

Figure I.6. Arterial network

As the arteries travel deeper into the body, they become smaller and more muscular, taking on the role of regulating blood flow and pressure. These muscular, or peripheral, arteries, such as the coronary arteries that nourish the heart muscle, the cerebral arteries that supply the brain, and the mesenteric arteries that feed the digestive system, are crucial for maintaining the delicate balance of oxygen and nutrient delivery. The radial artery, which originates from the brachial artery in the upper arm, is also considered a peripheral artery as it travels down the forearm.

In the lower part of the body, the abdominal aorta gives rise to the iliac arteries, which then continue as the femoral arteries in the thighs. The femoral arteries are a vital part of the peripheral arterial network, supplying blood to the lower limbs. Ultimately, the arterial network becomes increasingly intricate, with the peripheral muscular arteries giving rise to smaller vessels called arterioles. These arterioles play a vital role in controlling the flow of blood into

the capillary beds, where the exchange of oxygen, nutrients, and waste products takes place between the blood and the surrounding tissues.

1.3.2. Importance of the Arterial Network in Cardiovascular Health

The arterial network is the primary focus of clinical attention, as it is responsible for the delivery of oxygenated blood from the heart to the body's tissues and organs. Monitoring ABP, which reflects the force exerted by blood against the arterial walls [54], is a fundamental metric for evaluating cardiovascular health. Disruptions or abnormalities in ABP can be indicative of various cardiovascular diseases [27-31], as the arterial network is more susceptible to pathological changes like atherosclerosis, aneurysms, and vascular spasms [55, 56]. These arterial disorders can directly impact BP and tissue perfusion, leading to serious complications.

In contrast, the venous network primarily functions to return deoxygenated blood back to the heart. Venous pressure is generally much lower than arterial pressure, and venous pressure measurements are typically less clinically significant than arterial pressure measurements. While the venous system is essential for maintaining circulatory integrity, its functional importance is relatively lower compared to the arterial network. The arterial network and its regulation of BP are the primary focus of cardiovascular risk assessment and management, as disruptions can have significant consequences for overall health and well-being.

1.4. The systemic Circulatory System and Arterial Pressure Regulation

The systemic circulation is responsible for the transport of oxygenated blood from the heart to the body's organs and tissues. This process is facilitated by the coordinated activity of two interacting pumps [57]:

- *The left ventricle, which acts as the systolic pump, forcefully contracting to eject blood into the aorta.*
- *The aorta and other major elastic arteries, which serve as the diastolic pump, maintaining blood flow during ventricular relaxation.*

This dual-pump model, comprising the synchronized activity of the left ventricle and the compliant arterial system, provides deeper insights into the hemodynamic regulation of arterial pressure.

Arterial pressure refers to the force exerted by the circulating blood against the walls of the arteries [54]. It is typically measured in millimeters of mercury (mmHg), where 1 mmHg is equivalent to 133 Pascals [58]. The pressure generated during ventricular contraction is termed

systolic pressure, while the pressure during ventricular relaxation is known as diastolic pressure. However, arterial pressure incorporates both steady and pulsatile components that fluctuate throughout the cardiac cycle [57], as depicted in **Figure I.7**:

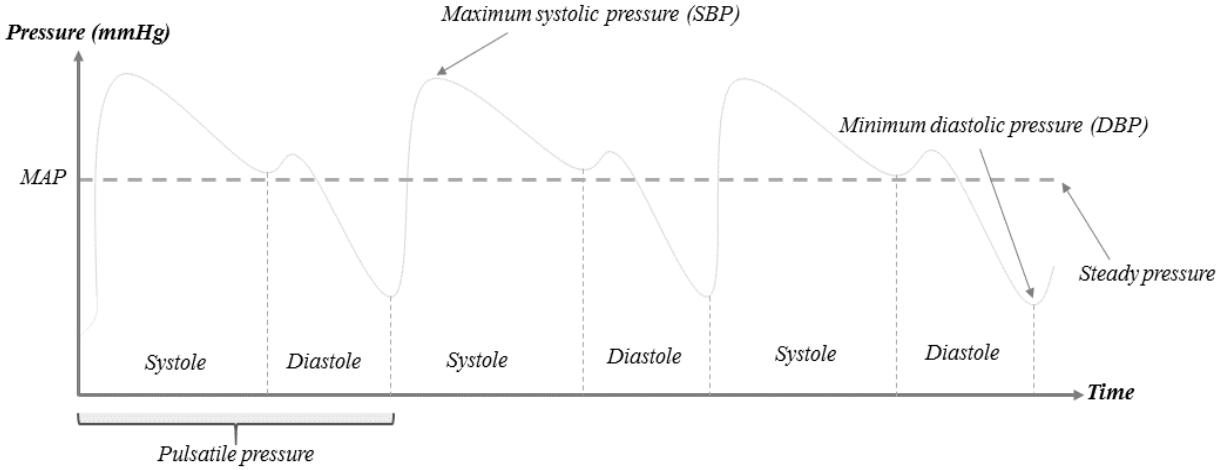

Figure I.7. Arterial pressure components

- ***Pulse arterial pressure (PAP):*** *Reflects the fluctuations between systolic and diastolic pressures around the MAP value.*
- ***Mean arterial pressure (MAP):*** *Represents the steady pressure component averaged over the cardiac cycle. MAP is typically calculated from brachial systolic and diastolic blood pressures using the formula: MAP = DBP + 1/3(SBP - DBP). For a more precise calculation, the integral of the arterial pressure curve can be used to determine the true mean value.*

The cardiovascular system can be conceptualized as a hydraulic circuit, with the heart acting as a rhythmic pump that propels blood through the arterial network, which repeatedly divides into smaller vessels to reach the body's tissues. This analogy to an electrical circuit is useful, as Ohm's law can be applied to describe the relationship between blood pressure, cardiac output, and systemic vascular resistance [57], as shown in **Figure I.8**. According to Ohm's law, the difference in pressure between two points in a circuit (ΔP) is equal to the product of flow (CO) and resistance (SVR): $\Delta P = CO \times SVR$. This relationship can be further expanded, as cardiac output is the product of stroke volume (SV) and HR: $\Delta P = SV \times HR \times SVR$. This formula describes MAP, which tends to remain relatively stable throughout the arterial tree.

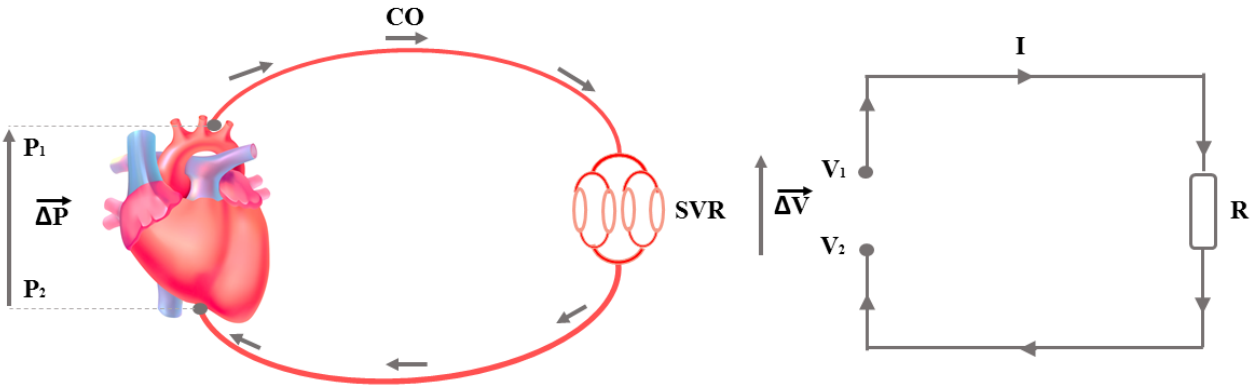

Figure I.8. Circulatory system as an electric circuit

However, this three-parameter model (SV, HR, SVR) is not sufficient to fully explain BP values [57], as demonstrated by the example of two individuals (**Figure I.9 (a)** and **(b)**) with the same MAP but different systolic and diastolic pressures. Comprehensive cardiovascular hemodynamic analysis must account for both the steady component of MAP and the pulsatile component of PAP. While MAP depends on HR, SV, and SVR, PAP is influenced by the interaction between the forward pressure wave originating from left ventricular ejection and the reflected pressure waves in the arterial system [59]. Hence, both MAP and PAP must be considered for a thorough understanding of arterial pressure regulation.

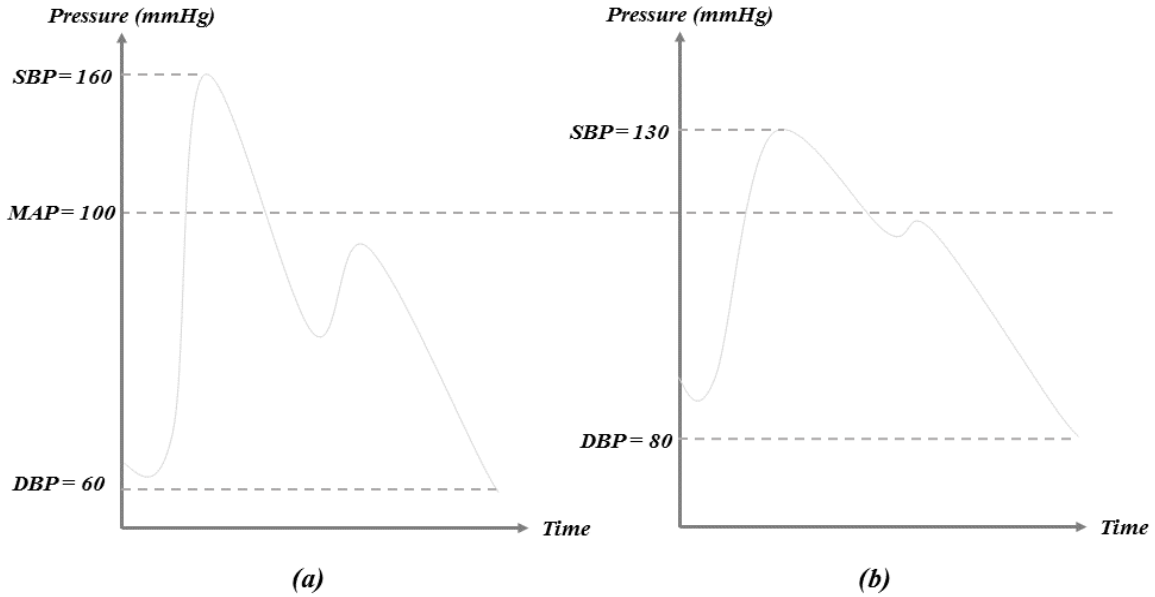

Figure I.9. Two PAPs sharing similar MAPs but different pressure values

2. The Role of Blood Pressure in Cardiovascular Health and Disease

The human cardiovascular system undergoes inherent dynamic changes over the cardiac cycle, manifested as pulsatile arterial pressure (PAP) waveforms. With each heartbeat, the

coordinated contractions of the heart chambers pump oxygenated blood into the arteries. The resulting pressure pulse then propagates away from the heart throughout the arterial system. Under normal physiologic conditions, these waves have a characteristic morphology or shape that varies predictably throughout the cardiac cycle. However, CVDs can disrupt the normal function and structure of the heart and blood vessels, altering the usual pulse wave morphology and resulting in AAPs clinically recognized to be disease indicators [27-29].

2.1. Blood Pressure and Cardiovascular Function

Analysis of the ABP waveform's shape, amplitude, and duration provide a wealth of information that aids in the diagnosis and management of different conditions [60]. However, the correct interpretation of these waveforms requires a clear understanding of their normal characteristics, their connection to the cardiac cycle, and the distinctions in waveforms captured from different arterial locations [61].

During systole, the left ventricle ejects blood into the aorta, resulting in the aortic pressure reaching its peak value, known as SBP, followed by a decline to its foot value referred to as DBP [59]. A slight notch is often observed on the ascending limb of the aortic pressure pulse, also known as an anacrotic notch [62]. This notch gives rise to two distinct waves, namely the anacrotic and tidal waves. Furthermore, the descending limb is interrupted by an incisura, a sharp dip produced by the aortic valve closure, followed by a smaller wave before a more gradual decrease in pressure until the next systole [27].

As the arterial pulse propagates towards the peripheral arteries, several changes occur, including a steeper initial upstroke, a less pronounced anacrotic notch, a higher SBP and a lower DBP [27,59,62]. Additionally, the tidal wave becomes smaller compared to the initial wave, which is known as the percussion wave [62]. Moreover, the central aortic pulse's incisura progressively disappears and is replaced by a lower dip referred to as the dicrotic notch, which is then succeeded by the appearance of a positive wave known as the dicrotic wave [27]. **Figure I.10** compares the central aortic pulse and the peripheral radial pulse waveforms, illustrating their distinct features that align with the aforementioned characteristics.

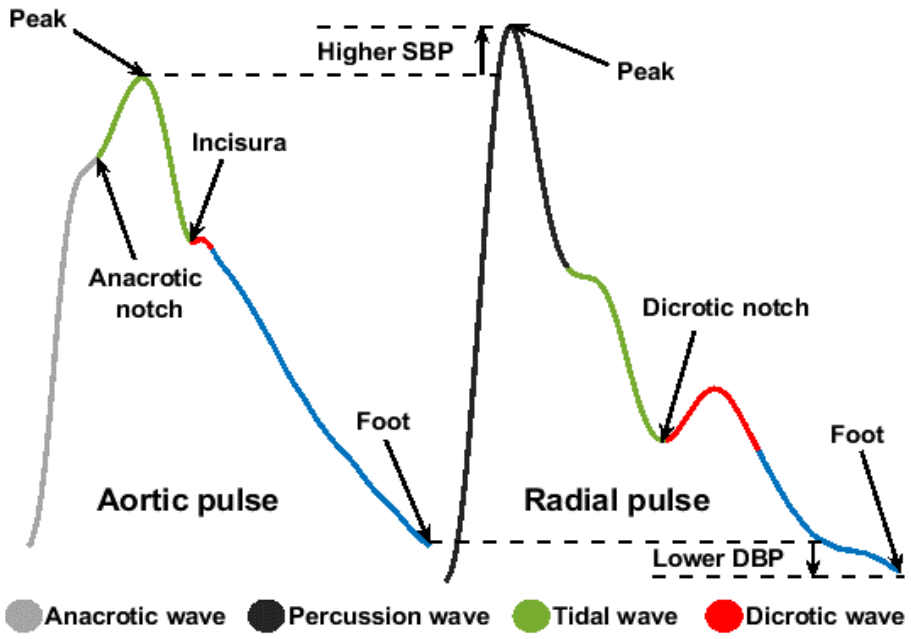

Figure I.10. Central and peripheral arterial pulse characteristics

2.2. Blood Pressure Profiles in Cardiovascular Pathologies

2.2.1. Arterial Pulse Waveforms in Cardiovascular Diseases

The pathophysiological mechanisms underlying CVD impact the morphological patterns of the ABP waveform through changes to its characteristic shape, amplitude and duration. Careful analysis of these biometric changes provides valuable insights for diagnosing and managing various conditions such as diabetes, obstructive sleep apnea, diastolic dysfunction, hypertension, and coronary artery disease [60].

Distinct AAP waveform morphologies have been linked to specific cardiovascular pathologies. For instance, the bisferiens pulse, characterized by two prominent systolic waves, has been observed in patients with pure AR, hypertrophic cardiomyopathy, or the coexistence of AS and severe AR [28]. Conversely, severe AS may cause a weak (parvus) pulse with a delayed systolic peak (tardus) [61], as well as an anacrotic pulse, which is typically characterized by a small premature systolic peak prior to reaching the main peak.

Another notable AAP waveform pattern is the dicrotic pulse, which features a dicrotic notch nearly reaching the baseline, followed by a large dicrotic wave. This pulse morphology has been associated with various cardiac conditions characterized by reduced cardiac output, such as pulmonary embolism, constrictive pericarditis, pericardial tamponade, and cardiomyopathies [63-65]. Similarly, a deep dicrotic notch with a steep downstroke may indicate low systemic vascular resistance [59], as well as sepsis [66].

Furthermore, the bounding pulse, characterized by a rapid upstroke and widened PP [67], can be present in hyperkinetic states (e.g., thyrotoxicosis, fever, anemia) or pathological conditions like arteriovenous fistula and AR [28]. A specific type of bounding pulse, known as the water hammer pulse, is commonly observed in cases of severe AR, marked by a quick rise followed by a sharp descent in pressure [68].

The following figure further illustrate the aforementioned abnormalities:

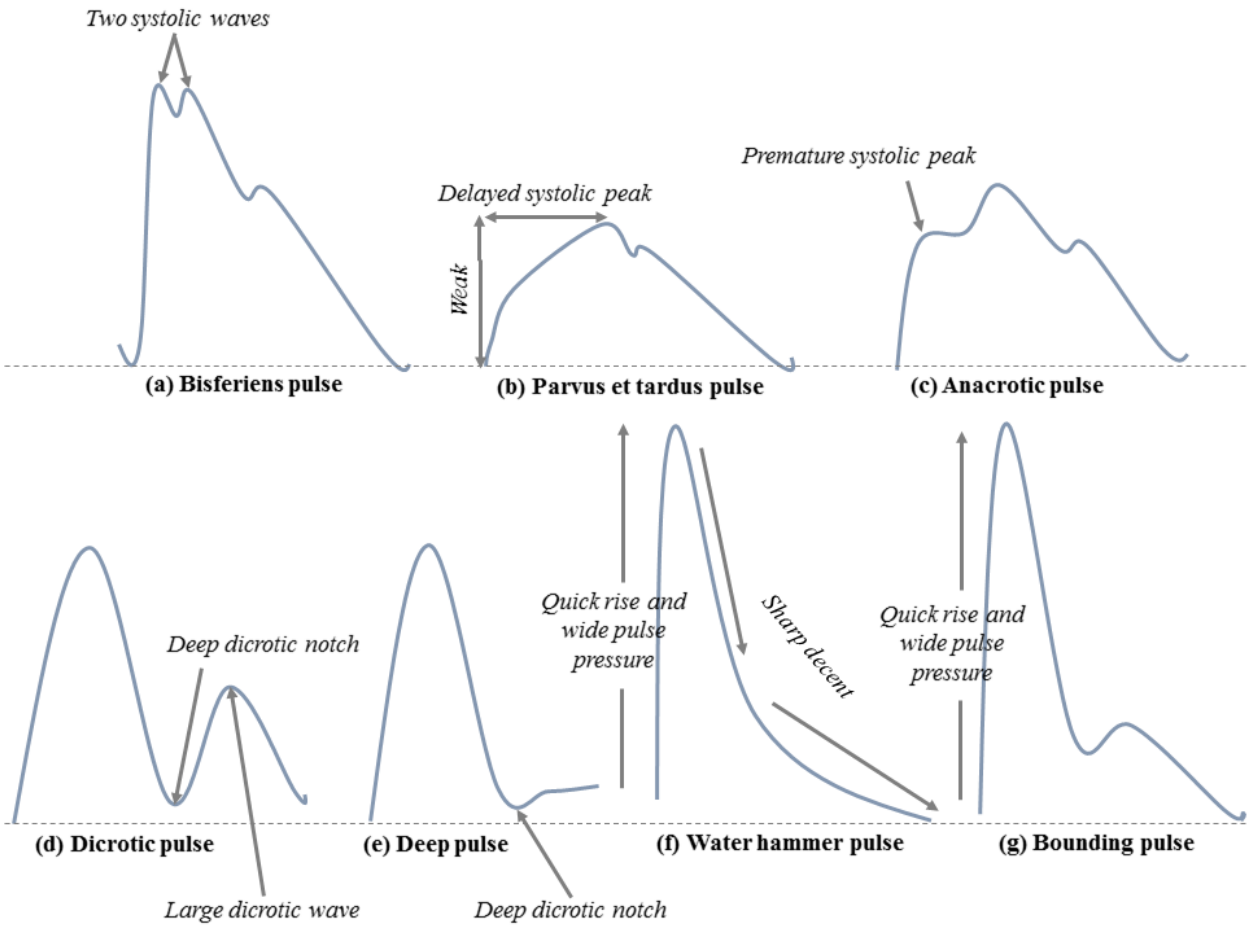

Figure I.11. Abnormal arterial pulse patterns in cardiovascular diseases

2.2.2. Hypertension

Hypertension, or elevated blood pressure, is a highly prevalent medical condition and significant risk factor for premature mortality worldwide. It not only elevates systolic and diastolic blood pressure values but also alters pulse wave morphology through its various cardiovascular effects that can develop over a person's lifetime, including coronary disease, left ventricular hypertrophy, valvular heart diseases, atrial fibrillation, cerebral stroke, and renal failure - each potentially manifested as unique AAP forms. Unfortunately, hypertensive

individuals often remain unaware of their condition until they experience serious health complications. Beyond its direct effects on cardiovascular health, hypertension has far-reaching consequences, causing decreased productivity, economic losses, and even contributing to traffic accidents [3,4].

3. Conventional Blood Pressure Measurement Techniques

Considering the widespread burden of CVD and the often-asymptomatic nature of hypertension, careful preventative attention and regular ABP monitoring are essential to mitigate adverse public health consequences. Healthcare professionals routinely measure ABP, either directly through invasive methods or indirectly through non-invasive techniques.

The invasive approach involves the direct measurement of continuous ABP curves to identify any fluctuations or abnormalities within the waveforms. This method typically requires the insertion of a catheter into the radial artery (**Figure I.12**), as it presents a relatively low-risk and highly palpable access point [69]. By continuously monitoring the ABP waveform, clinicians can obtain valuable insights into the underlying pathophysiological mechanisms and patterns associated with various cardiovascular conditions, as emphasized in the previous sections.

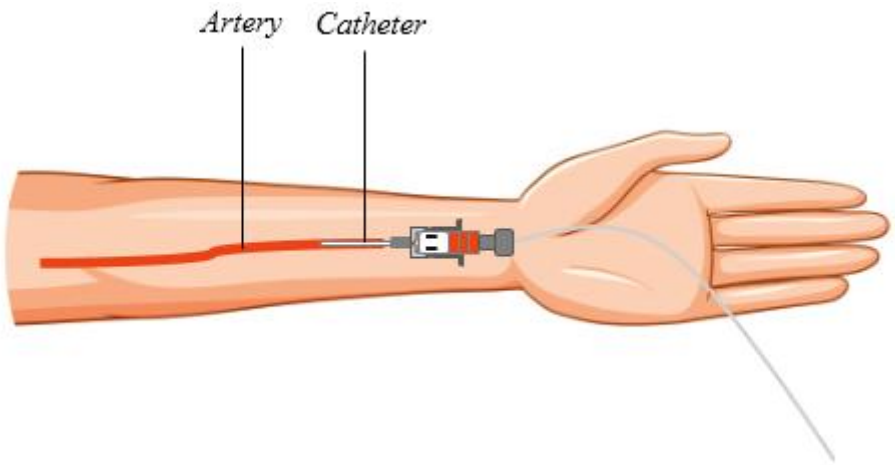

Figure I.12. Invasive blood pressure measurement

On the other hand, non-invasive methods using cuff-based devices (**Figure I.13**) offer safer and more cost-effective alternatives for ABP measurement. These techniques are commonly employed to determine systolic and diastolic pressure values, which are then used to assess the presence of high BP (hypertension) or low BP (hypotension). While lacking the level of detail

provided by invasive monitoring, non-invasive BP measurement remains a widely adopted approach in clinical practice due to its accessibility and reduced risk to the patient.

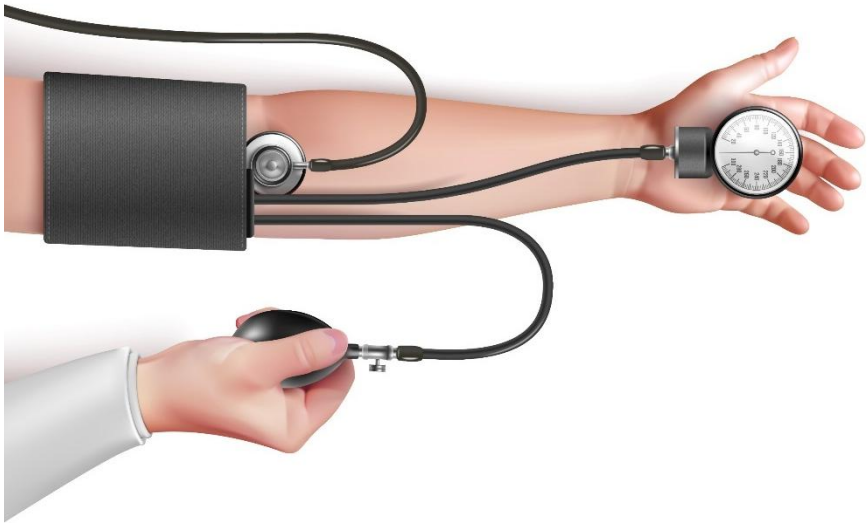

Figure I.13. Cuff-based blood pressure measurement

3.1. Limitations and Challenges

Currently, auscultation (refer to **Figure I.13**) is considered the clinical gold standard for intermittent BP measurement [70]. However, this method requires trained personnel to perform the measurement accurately and relies on the observer's hearing ability, which can sometimes lead to variability in readings. Alternatively, automated devices offer more independent self-monitoring (refer to **Figure I.14**) but have limitations, such as discomfort during cuff use and inaccuracies resulting from improperly fitting cuff sizes or unique arm dimensions [71-75].

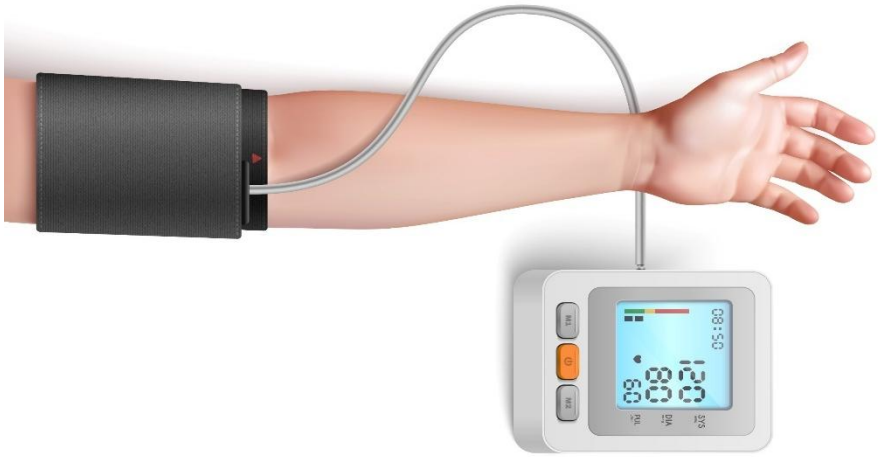

Figure I.14. Automated cuff-based blood pressure measurement

In contrast, invasive arterial catheterization facilitates continuous ABP monitoring and AAP identification through direct arterial access. Although this technique serves as the gold

standard for continuous ABP measurement [76], it is mainly reserved for critical care settings due to the potential complications, including embolism, ischemic damage, bleeding, pseudoaneurysm, and infection [34].

Noninvasive alternatives, such as vascular unloading (**Figure I.15**) and arterial tonometry (**Figure I.16**), provide another avenue for continuous ABP measurement. Vascular unloading involves using a variable finger-cuff and a PPG sensor to estimate the intra-arterial pressure by analyzing changes in blood volume over time [77]. However, prolonged cuff use induces discomfort, numbness and arterial congestion [78]. Arterial tonometry employs a pressure transducer for cuff-less measurement but may exhibit reduced accuracy in obese individuals due to slowed pulse wave propagation to the skin [78].

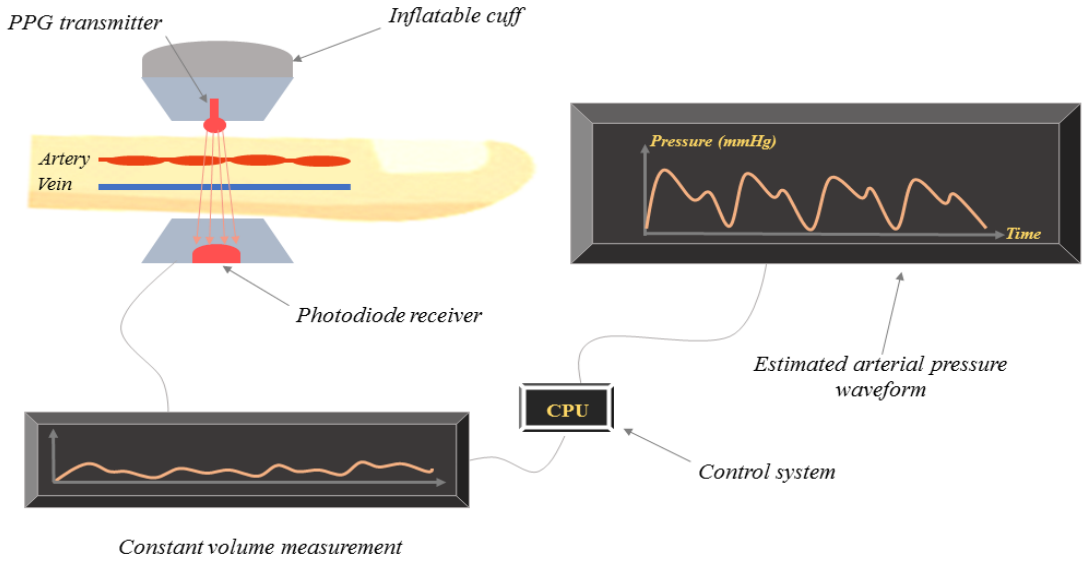

Figure I.15. Principle of vascular unloading measurement

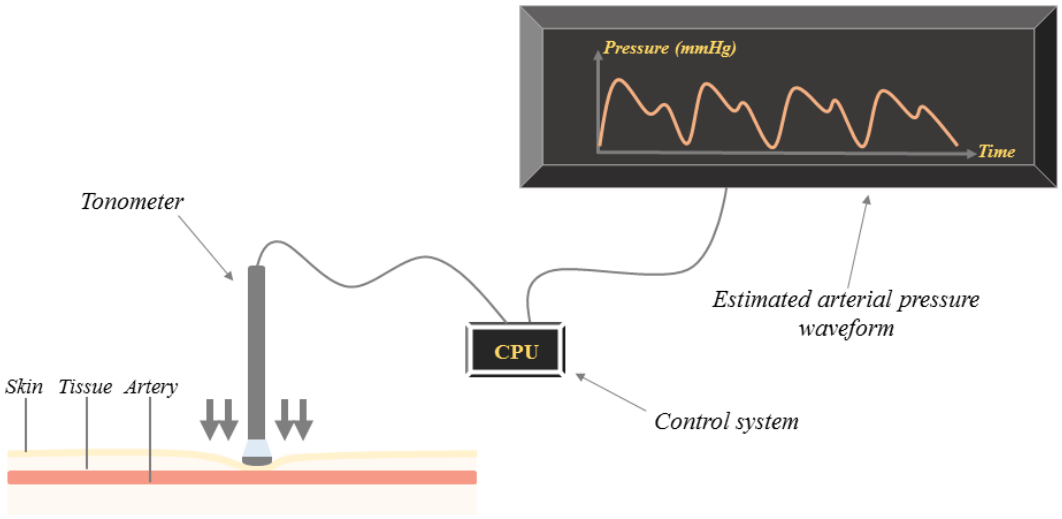

Figure I.16. Principle of tonometry measurement

Ultimately, whatever the continuous measurement approach employed, it still requires medical expertise to interpret waveforms for AAP waveforms identification. Thus, advances are warranted to non-invasively identify these abnormalities through high-fidelity signals and specialized systems, bridging the gap between clinical expertise and patient self-care.

4. The Emergence of AI-Driven Blood Pressure Assessment Approaches

4.1. Introduction to Machine Learning

ML is a field of AI that enables systems to learn and improve from experience without being explicitly programmed [79]. It refers to algorithms that can automatically learn from patterns within data to make future predictions. ML algorithms use statistical techniques to perform specific tasks effectively, such as classification, regression, clustering, and prediction, without relying on rule-based programming. The main types of learning include:

(1) Supervised learning: *Algorithms learn based on labeled examples in a training dataset containing input-output pairs. Models learn the mapping function from input to output to make predictions on new unlabeled data. This approach is well-suited for regression (predicting continuous values) or classification (predicting discrete labels) tasks like blood pressure prediction.*

(2) Unsupervised learning: *Algorithms find hidden patterns within unlabeled data. Models cluster or group similar inputs to discover relationships without labeled responses. This technique is useful for exploratory analysis but not prediction.*

(3) Reinforcement learning: *Algorithms learn optimal actions through trial-and-error interactions with an environment to maximize a reward function. Agents are not told which actions to take but learn via feedback to solve problems over time. This method is applied in game environments but less suitable for clinical prediction tasks.*

Supervised algorithms are well-suited for blood pressure prediction given availability of labeled physiological signals and outcomes. Through mapping input features to target outputs like systolic, diastolic or arterial pressure patterns, ML shows potential for non-invasive hemodynamic assessment. Rigorous model development following best practices can help validate this application both within and outside the clinical.

4.2. Supervised Learning Model Development

Developing a supervised learning model involves several steps:

(1) Data collection and curation: *Gathering high-quality, representative, and relevant data is crucial for model performance.*

(2) Data preprocessing and feature engineering: *Preparing the data by handling missing values, encoding categorical variables, and extracting relevant features.*

(3) Algorithm selection: *Choosing the appropriate ML algorithm based on the problem type (classification or regression.) and the characteristics of the data.*

(4) Training & Validation: *The model is fitted to training data and evaluated on validation data to optimize hyperparameters and prevent overfitting.*

(5) Testing: *Final model performance is assessed on an unlabeled test set to predict new examples.*

4.3. Evaluating a Supervised Learning model

Evaluating the performance of a supervised learning model is a crucial step in the model development process. This involves assessing the model's ability to make accurate predictions on unseen data, as well as identifying potential issues like overfitting and underfitting.

Overfitting occurs when the model performs exceptionally well on the training data but fails to generalize to new, unseen data [80]. This results in high-performance metrics on the training data but significantly worse performance on the test data. Conversely, underfitting is characterized by low performance on both the training and test data [81], indicating that the model is too simple to capture the underlying patterns in the data.

4.2.1. Classification Metrics for Categorical Outcomes

Common performance metrics used to evaluate classification models include accuracy, precision, recall (sensitivity), and F1 score. For example, in hypertension classification, a machine learning model produces four possible outcomes:

(a) Hypertensive data correctly classified as hypertensives. (b) Hypertensive data incorrectly classified as non-hypertensives. (c) Non-hypertensive data correctly classified as non-hypertensives. (d) Non-hypertensive data incorrectly classified as hypertensives.

Accuracy: *Percentage of correct predictions (a and c) out of total data samples (a, b, c and d).*

Precision: *Percentage of true positive predictions (a) relative to the total number of positive predictions (a and d).*

Recall (sensitivity): *Percentage of true positive predictions (a) relative to the actual number of positive samples (a and b).*

Specificity: *Percentage of negatives (c) correctly identified among all actual negative samples (c and d).*

F1 Score: *Harmonic mean of precision and recall.*

4.2.2. Regression Metrics for Continuous Outcomes

Regression models are often simpler to evaluate, as the targets are continuous rather than categorical. Considering a model trained to estimate BP values like SBP, DBP, or MAP, error-based metrics are frequently employed to quantify the differences between actual and predicted BP values:

Mean Absolute Error (MAE): *Average absolute difference between predictions (BP estimates) and targets (Actual BP values).*

Mean Squared Error (MSE): *Average squared difference between predictions and targets.*

Standard Deviation (STD): *Squared root variance of predictions/targets errors.*

4.2.3. Cross-validating a model

To reliably estimate real-world performance, metrics should be calculated via k-fold cross-validation on the test set rather than a single train-test split [82]. This involves repeatedly training and evaluating the model on different subsets of the data:

Cross-Validation*: Data is split into k equally sized subsets, with k-1 used for training and the remaining subset for validation. The process is repeated k times, each time using a different validation set. Results are averaged to improve accuracy.*

By Comparing the aforementioned performance metrics across supervised algorithms and their hyperparameters can help identify the most suitable model for the ABP prediction tasks.

4.4. Leveraging Machine Learning for Non-Invasive Monitoring

Given the limitations associated with conventional BP measurement techniques, researchers have begun to explore the potential of ML for improving sustained BP monitoring. Technological advancements in wearable PPG sensors, coupled with the emergence of sophisticated ML models, have shown promise for the non-invasive estimation of BP trends and the classification of hypertension status.

Typically, two main approaches have been explored in this domain. The first approach relies exclusively on PPG signals, extracting a variety of informative attributes from the waveforms. These attributes span the time-domain, frequency-domain, time-frequency domain, and morphological features, capturing various aspects of the underlying cardiovascular dynamics. The extracted characteristics are then fed as input parameters into ML models to produce distinct predictions, such as SBP, DBP, MAP, as well as categorical BP class-level for classification purposes (e.g., normotensive, prehypertensive, hypertensive).

The second approach incorporates PPG signals alongside other physiological data, such as ECG recordings. This bio-signal combination is typically used to compute the PAT or PTT parameters - the elapsed time from when the heart produces a pulse until that same pulse wave eventually surfaces at the PPG sensing site. The PAT or PTT measurements are used alongside other PPG features as inputs into ML models for BP estimation and classification tasks.

By leveraging the inherent relationships between the PPG and ECG signals or the exclusive use of PPG signals, these ML-based techniques aim to provide a non-invasive, cost-effective, and continuous alternative to traditional BP measurement methods. Ongoing research in this field continues to explore the optimal feature engineering techniques, ML model architectures, and multimodal data integration strategies to further enhance the performance and reliability of non-invasive BP monitoring systems.

4.3.1. Principles of Photoplethysmography

PPG is a non-invasive optical technique that has been employed for over 80 years to measure changes in blood volume within living tissues [83]. This technology utilizes light-based sensing to quantify signals from convenient sites like the wrist, finger, or earlobe [84]. The sensor design can be either transmissive, where the light source and photodetector are positioned on opposing sides of the tissue, or reflective, where they are positioned on the same (**Figure I.17**). Regardless of configuration, PPG employs skin surface optical signals without direct contact, enabling non-invasive tracking of cardiovascular dynamics. The underlying principle lies in the fact that the amount of light absorbed or reflected from vascularized skin varies dynamically with shifts in blood volume within the sensing area, encompassing arteries, veins and capillaries [83].

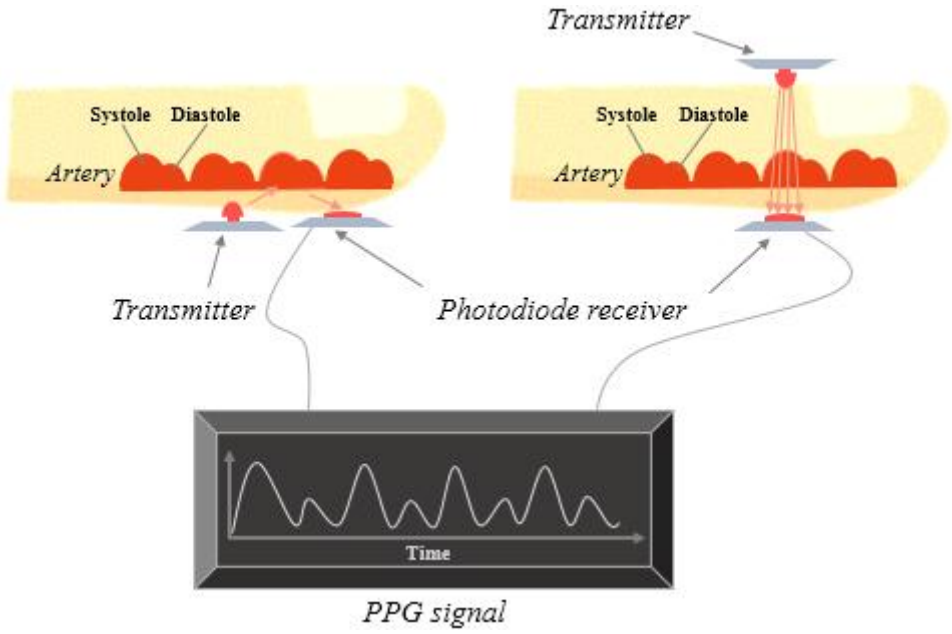

Figure I.17. Photoplethysmography measurement from a finger

PPG signals provide a wealth of physiological data that can aid in identifying abnormal health conditions in both outpatient and clinical settings [85, 86]. These signals consist of pulsatile (AC) and non-pulsatile (DC) elements [87]. The AC element conveys volumetric changes related to the cardiac cycle, enabling HR measurement. In contrast, the DC portion offers insight into vascular volume fluctuations influenced by factors such as respiration, sympathetic activity and thermoregulation [88].

By optically monitoring microvascular blood displacement at easily accessible superficial sites, PPG serves as a convenient non-invasive and cost-effective tool for cardiovascular monitoring without need for intrusive devices [86, 89]. This allows detection of various hemodynamic parameters through a single sensor, including blood oxygen saturation, heart rate, blood pressure, cardiac output, respiration, arterial stiffness, endothelial function, microvascular blood flow, and autonomic nervous system activity [86]. This ability to evaluate microcirculatory impacts through simple optical sensing carries promise for expanding applications in hemodynamic assessment.

4.3.2. Electrocardiography, Photoplethysmography and Arterial Blood Pressure

The ABP, ECG, and PPG signals are closely interrelated as they provide insights into cardiovascular physiology. Similar to the ECG waveform, the AC component of the PPG signal can be used to estimate heart rate [90]. However, the underlying principles by which they capture this physiological parameter differ, as illustrated in **Figure I.18**. The ECG measures

the electrical activity of the heart, whereas the PPG monitors the mechanical effects of these electrical stimulations through changes in blood volume within the pressurized arteries.

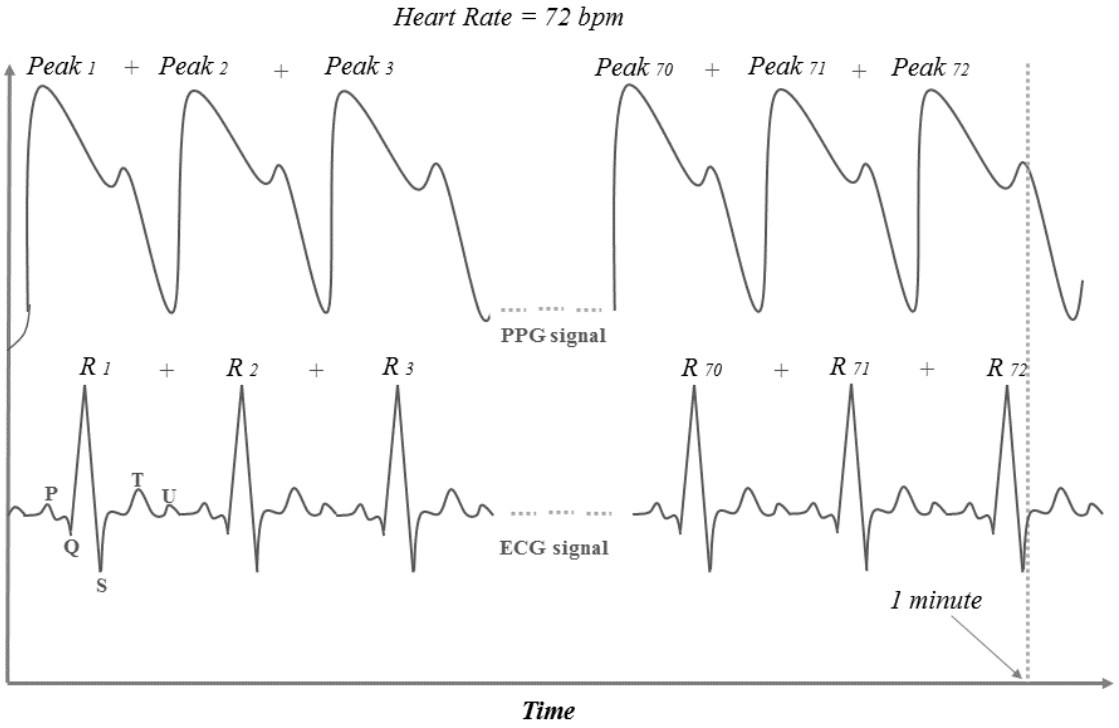

Figure I.18. Heart rate measurement in PPG and ECG signals

Specifically, the ECG's QRS complex represents the electrical depolarization of the myocardium or heart muscle. This electrical activation triggers the mechanical contraction of the heart to forcibly pump blood into the systemic arteries, generating the systolic arterial pressure wave. Meanwhile, the ECG's T wave corresponds to the ventricular relaxation, during which the aortic valve closes, and the aorta and elastic arteries continue to squeeze the blood while the heart refills. This arterial compliance leads to the formation of the diastolic arterial pressure wave, completing the arterial pulse wave.

This electromechanical coupling alters arterial pressures, leading to rapid fluctuations in blood flow volume that attenuate the PPG sensor's light source. This permits detection of blood flow volume changes throughout the cardiac cycle. As **Figure I.19** depicts, the PPG waveform's systolic, dicrotic, and diastolic components closely resemble those of the ABP signal. By identifying the characteristic ECG R-wave peaks and PPG/ABP systolic peaks, heart rate can be extracted from each signal by computing their coinciding peaks over one minute.

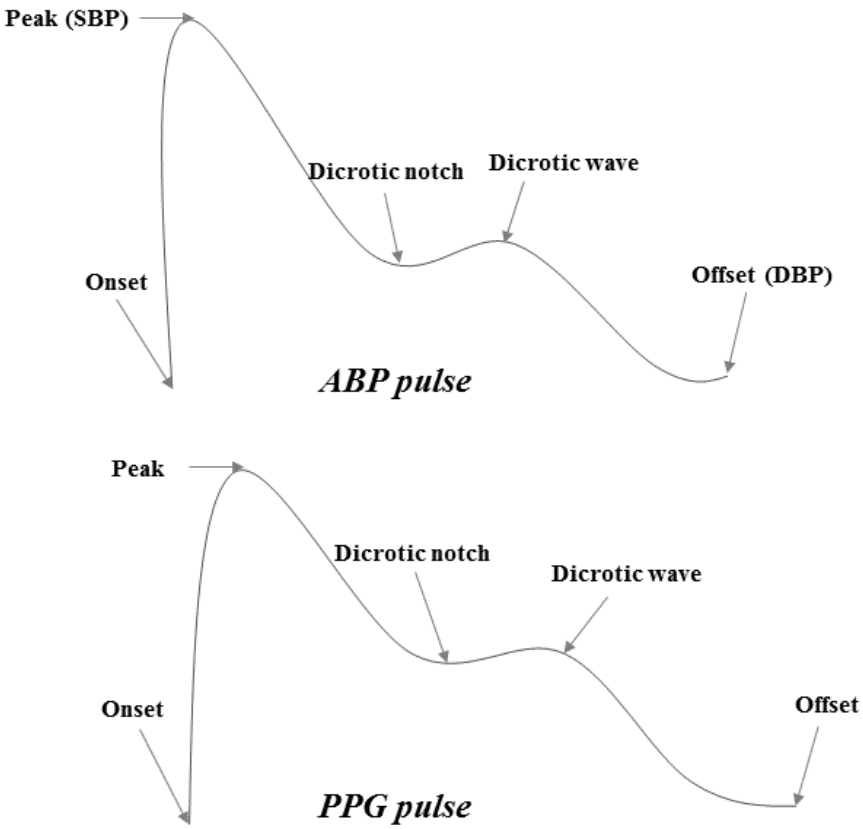

Figure I.19. Waveform similarities between an ABP and PPG signals

The temporal relationship between the ECG R wave and corresponding PPG systolic upstroke is termed the PAT or PTT, depending on measurement points [83]. This time interval provides valuable data about vascular properties as it is influenced by factors such as arterial stiffness and pressure wave propagation through the arterial tree [91]. The complementary nature of ECG and PPG signals has facilitated multimodal ML approaches integrating these waveforms to enhance ABP monitoring accuracy and robustness, especially for wearable health technologies and clinical applications.

4.3.3. Potential and Challenges of Current Machine Learning Approaches

Recent research on BP monitoring has explored various approaches, each with distinct design considerations regarding the sensing device, input features, ML algorithms, and target output. **Table I.1** outlines the different design aspects currently reported in the literature.

Table I.1 Different design aspects currently reported in the literature.

Research	*Sensor*	*Features*	*Algorithm*	*Dataset*	*Output*	*Performance*
[35]	*PPG*	*Spectral and morphological features*	*ANN*	*58,795 ABP/PPG signals*	***BP values:*** *SBP (mmHg)* *DBP (mmHg)*	***MAE ± STD:*** *4.02 ± 2.79* *2.27 ± 1.82*

[92]	*PPG*	*Time-domain and morphological features*	*RF*	*11492 PPG pulse signals*	***BP values:*** *SBP (mmHg)* *DBP (mmHg)*	***MAE ± STD:*** *4.21 ± 7.59* *3.24 ± 5.39*
[93]	*PPG*	*Temporal and frequency features*	*CNN (ResNet)*	*700 hours of ABP&PPG recordings*	***BP values:*** *SBP (mmHg)* *DBP (mmHg)*	***MAE:*** *9.43* *6.88*
[94]	*PPG*	*Raw pulse wave signal*	*CNN*	*50,000 PPG pulse wave*	***BP values:*** *SBP (mmHg)*	***STD:*** *11.40*
[95]	*PPG*	*Time-domain and morphological features*	*LSTM*	*9000 PPG segments*	***BP values:*** *SBP (mmHg)* *DBP (mmHg)*	***MAE ± STD:*** *3.23 ± 4.74* *1.59 ± 1.96*
[96]	*PPG*	*1024 PPG samples*	*CNN*	*127,260 ABP&PPG segments*	***BP values:*** *SBP (mmHg)* *DBP (mmHg)* *MAP (mmHg)*	***MAE ± STD:*** *5.727 ± 9.162* *2.310 ± 4.437* *3.449 ± 6.147*
[97]	*ECG & PPG*	*PTT, heart rate, PPG morphological features*	*SVM*	*4254 ABP&PPG signals*	***BP values:*** *SBP (mmHg)* *DBP (mmHg)* *MAP (mmHg)*	***MAE ± STD:*** *12.38 ± 16.17* *6.34 ± 8.45* *7.52 ± 9.51*
[98]	*ECG & PPG*	*PAT, heart rate, Time-domain and morphological PPG features*	*AdaBoost*	*3663 ABP&PPG signals*	***BP values:*** *SBP (mmHg)* *DBP (mmHg)* *MAP (mmHg)*	***MAE ± STD:*** *11.17 ± 10.09* *5.35 ± 6.14* *5.92± 5.38*
[99]	*PPG*	*256 PPG samples*	*CNN*	*100 ABP&PPG signals*	***BP values:*** *SBP (mmHg)* *DBP (mmHg)* *MAP (mmHg)*	***MAE ± STD:*** *3.68 ± 4.42* *1.97 ± 2.92* *2.17 ± 3.06*
[100]	*PPG*	*625 PPG samples*	*CNN*	*1227 ABP&PPG signals*	***BP values:*** *SBP (mmHg)* *DBP (mmHg)* *MAP (mmHg)*	***MAE ± STD:*** *7.95 ± 10.35* *4.11 ± 5.5* *3.83± 5.13*
[101]	*PPG*	*RGB PPG images*	*CNN*	*12000 ABP&PPG signals*	***BP values:*** *SBP (mmHg)* *DBP (mmHg)*	***MAE ± STD:*** *7.419 ± 6.849* *3.395±3.414*
[102]	*PPG*	*Time-domain and morphological features*	*ANN*	*2000 ABP&PPG signals*	***BP values:*** *SBP (mmHg)* *DBP (mmHg)*	***MAE ± STD:*** *4.23 ± 5.30* *4.46 ± 6.37*
[36]	*PPG*	*TF-features using STFT*	*BLSTM*	*900 PPG segments*	***BP level trials:*** *NT vs. HT* *NT vs. PHT* *(NT+PHT) vs. HT*	***F1 scores:*** *97.29 %* *97.39 %* *93.93 %*

[103]	*PPG*	*2100 PPG features points*	*KNN*	*900 PPG segments*	***BP level trials:*** *NT vs. HT* *NT vs. PHT* *(NT+PHT) vs. HT*	***F1 scores:*** *100 %* *100 %* *90. 80 %*
[104]	*PPG*	*RGB images using CWT (scalogram)*	*CNN*	*2904 PPG images*	***BP level trials:*** *NT vs. HT* *NT vs. PHT* *(NT+PHT) vs. HT*	***F1 scores:*** *80.52 %* *92.55 %* *82.95 %*
[105]	*ECG & PPG*	*PAT and 10 PPG features*	*KNN*	*121 ABP&PPG signals*	***BP level trials:*** *NT vs. HT* *NT vs. PHT* *(NT+PHT) vs. HT*	***F1 scores:*** *84.34 %* *94.84 %* *88.49%*

As the table illustrates, researchers have predominantly focused on addressing the limitations of traditional BP measurement methods. This is typically achieved through either estimating continuous BP values or classifying BP into discrete levels. The underlying motivation behind these studies is to address the prevalence and asymptomatic nature of hypertension [30, 31], leveraging the capabilities of portable and wearable devices. Studies in [95, 100-102] have achieved good results in BP estimation tasks, meeting the standards set by the BHS and the AAMI [106, 107]. Similarly, the proposed classification systems have reported impressive F1 scores up to 100%. While these technical achievements are commendable, to realize desirable public health outcomes, the research objectives must extend beyond system performance. Factors such as accuracy, reliability, accessibility, and seamless integration into clinical workflows should be prioritized to ensure the successful translation of these ML-based solutions into practical, user-friendly, and clinically relevant tools.

Recent investigations [108,109] have compared the performance of ML models that integrate features from both ECG and PPG data, against models relying solely on PPG-derived features. Findings indicate that the use of combined ECG and PPG features can lead to relatively improved BP performance. However, the results were unable to exceed the outstanding performance attained by other approaches focusing solely on PPG-based BP estimation techniques [110-113, 95].

One key challenge with ECG-based approaches is the precise positioning of chest electrodes. This specific electrode arrangement protocol may be unfamiliar and inconvenient for the general public [114, 115], particularly in the context of wearable applications where the

ECG unit may protrude beneath the user's clothing [116]. Accounting for these integration challenges discussed, PPG emerges as the most convenient sensor to be utilized in wearable or portable health technologies [114, 117]. This is particularly relevant as modern smartphones and smartwatches are increasingly equipped with PPG sensing functionality [116].

While the integration of PPG signals holds promise for ML-based BP monitoring, there are notable technical challenges that need to be addressed. Despite the reduced errors reported in BP prediction studies [92, 95, 97, 98, 102, 105], extracting morphological features from PPG signals is impractical. PPG is susceptible to motion artefacts [38], which constrains the flexibility in the feature extraction process due to the complex preprocessing requirements and potential for outlier interference. An optimal BP model would benefit from a simpler yet high-performing design. Time-domain and transform techniques, such as TF analysis, may be more reasonable for applications on affordable devices.

Additionally, the computational complexity of DL approaches can compromise the usability of these systems on low-cost technologies. DNN require powerful GPUs during the training phase, which can be a barrier to enabling accessible BP monitoring on affordable devices. For instance, the BLSTM model proposed by Tjahjadi et al. [36] and the CNN model developed by Liang et al. [104] required over 33 and 350 minutes of training time, respectively, even with smaller datasets. Similarly, the ResNet-GRU model utilized in [93] is computationally expensive and exhibits slow convergence. This confirms the exceptional hardware demands of DL algorithms. While cloud computing could address some of the challenges posed by DNN architectures, it introduces concerns related to latency, costs, and privacy due to the transmission of personal health data.

Furthermore, most studies have inadequately accounted for dataset diversity, which is essential for ensuring the generalizability of the developed models. For example, the figshare database used in [36, 104] lacked diversity in systolic and diastolic BP values. Similarly, some studies have excluded extreme high and low BP readings without clear justification [102], while others have removed records containing AAP patterns, such as the bisferiens pattern, despite its potential association with hypertension [105]. This underestimation of AAP pattern diversity goes beyond just data collection. Previous studies have predominantly focused on estimating ABP waveforms using ML and DL techniques [118, 119], neglecting the importance of identifying abnormalities that may occur in these waveforms. Exploring AAP morphologies has the potential to revolutionize cardiovascular assessment beyond just pressure values or

predicted waveforms. Nonetheless, even without addressing these gaps, ideal datasets for ML-based BP monitoring should, at a minimum, account for both the size and the diversity of AAP patterns, alongside comprehensive representation of BP values.

5. Motivation and Rationale for the Current Research

The field of arterial pressure prediction has seen a proliferation of research, exploring PPG signals in conjunction with various ML and DL approaches. These efforts have resulted in successful estimations of SBP, DBP, MAP, and even ABP waveforms, as well as classifications of normotension, prehypertension, and hypertension. However, despite these advancements in utilizing PPG signals, the non-invasive identification of the morphological state of ABP waveforms remains an area of concern in the existing literature. This is particularly important as specific CVDs have been linked to distinct AAP morphologies.

Some studies have attempted to address this issue by relying on TCPD [120], which involves classifying the radial pulse into different morphological patterns, each corresponding to different diseases and syndromes in TCM [121,122]. However, in western medicine, the classification of arterial pulses and their relation to diseases differs from the approach used in TCM.

Therefore, advancements are needed to non-invasively characterize AAPs through PPG signals and specialized systems, bridging the gap between clinical expertise and patient self-care. This would enable the development of comprehensive cardiovascular assessment tools that go beyond just predicting pressure values or waveform estimates, and instead, identify abnormalities that may be indicative of underlying health conditions. Addressing this gap in the existing literature could revolutionize the field of arterial pressure prediction, allowing for more holistic and clinically relevant non-invasive monitoring solutions. By incorporating the identification of AAP morphologies, these advancements could enhance the potential of PPG-based systems to provide valuable insights into an individual's cardiovascular health status.

5.1. Addressing the Need for Improved Cardiovascular Management

Ongoing arterial pressure research generally aims to either provide more convenient alternative BP measurement solutions or contribute to early CVD diagnosis through hypertension risk classification. While both approaches ultimately relate to cardiovascular management through hypertension profiling, the latter approach is more impactful when considering global health outcomes. This is due to the poor public understanding of acceptable

BP values [123]. For example, over half of volunteers in one study struggled to correctly estimate a normal BP range [124], highlighting the need for simplifying BP monitoring systems beyond just non-invasiveness. An ideal method would promptly notify patients if their BP becomes abnormal, making classification approaches potentially more suitable than regression techniques.

Nevertheless, classifiers could also facilitate targeted CVD identification beyond hypertension alone while still utilizing arterial pressure waveforms. This can be achieved by capitalizing on the inherent association between CVDs and AAP patterns within these waveforms, alongside the correlating nature between PPG and ABP signals. Specifically, PPG signals provide insights into cardiovascular functioning, enabling AI to identify abnormal patterns predictive of specific AAP manifestations linked to underlying CVDs. Unfortunately, while PPG has been used to predict various diseases, its use in predicting arterial pressure abnormalities is limited to hypertension and hypotension [90]. Although AAPs have historically related to CVDs, current literature has not fully exploited arterial pressure predictive capabilities.

Accordingly, this research aims to develop a classification system capable of predicting not only hypertension risk but also the most common abnormalities that manifest within arterial pressure waveforms. Additionally, the classifiers will be optimized to provide more accurate BP value estimates. These objectives are based on an optimization strategy that adopts additional classification parameters beyond ML's internal hyperparameters. Overall, the overarching goals are to enable accessible sustained self-monitoring, facilitate early disease detection, assist clinical decision-making, and ultimately contribute to improved global cardiovascular health outcomes.

5.2. Bridging the Gap between Technical Advancements and Clinical Adoption

The development of effective ML classifiers for arterial pressure prediction necessitates a clear delineation of the intended usage environment and target end-users. The design considerations for clinical applications may differ significantly from those for consumer-oriented technologies.

In clinical settings, where these technologies will be directly integrated into healthcare workflows, transparency and interpretability of the ML models are of paramount importance [37]. Unlike consumer-oriented systems, where performance optimization may be the primary concern, clinically deployed models must be explainable and aligned with evidence-based

medical practices. An ML model that is exclusively optimized for performance, regardless of the underlying parameters or algorithmic details, lacks clinical validity. For example, relying on TF analysis-based predictors to boost the model's performance yields a black-box system that is unintelligible not only to healthcare practitioners but also to the engineers who developed the system. Rather than obscure feature sets, evidence-based inputs, such as time-domain or morphological features, would be more appropriate.

Algorithm selection is also problematic for the clinical translation of these technologies. As discussed previously, wearable technologies demand computationally efficient algorithms, avoiding the use of resource-intensive DNN architectures. However, the algorithmic constraints are even tighter in clinical contexts, requiring the use of simpler architectures. Parametric models offer a simple and transparent design structure, as the connection between variables is explicitly denoted by a set of parameters [57]. However, this simplicity may limit their ability to capture the nonlinear relationships within PPG inputs. Non-parametric models, on the other hand, provide more flexibility in handling such nonlinearity. Nevertheless, training such models on large datasets may compromise their transparency.

By reviewing these challenges, emphasis should be placed on constraining the classifiers' optimization by minimizing their internal parametric structure while maintaining acceptable performance potential. This balanced approach can help ensure the clinical relevance and adoption of the developed solutions. By addressing these critical challenges, this research aims to advance the state-of-the-art in ML-powered, non-invasive cardiovascular assessment. This would empower clinicians to proactively manage heart health and mitigate the global burden of CVDs through comprehensive arterial pressure waveform analysis.

Chapter II

Optimizing Arterial Blood Pressure-Based Risk Profiling

Analysis of Existing Classification Schemes and Experimental Plan Formulation of a Refined Classification system

1. Analysis of Existing Cardiovascular Disease Classification Approaches

1.1. Current State of the Art

The healthcare industry has witnessed a growing interest in leveraging ML techniques for CVD management. Numerous studies have explored the potential of PPG-based systems in predicting and classifying various cardiovascular conditions, as illustrated in **Table II.1**.

Table II.1 Current CVD classification systems.

Authors	*Features*	*Research subjects*	*Output*	*Classifier*	*Performance*
Liu et al. [125]	*Time-domain features*	*228*	*Arrhythmias*	*CNN*	***Accuracy:*** *85%*
Al Fahoum et al. [126]	*Time-domain and morphological features*	*360*	*CVDs group vs. healthy*	*NB* *ANN* *KNN*	***Accuracy:*** *94.44%* *89.56%* *82.08%*
Putra et al. [19]	*Time and frequency-domain features*	*58*	*CHD*	*KNN*	***Accuracy:*** *90.9%*
Hackstein et al. [18]	*Frequency-domain features*	*55*	*Aortic aneurysms*	*KNN* *NB*	***Average accuracy:*** *60%*
Hosseini et al. [20]	*Time-domain features*	*48*	*CAD*	*KNN*	***Accuracy:*** *81.5%*
De Moraes et al. [21]	*Time-domain features*	*32*	*Cardiopathies*	*KNN* *MLP*	***Accuracy range:*** *88.57%-100%*
Chiang et al. [127]	*PPG perfusion index (AC/DC)*	*74*	*Blood flow & stenosis degree*	*SVM*	***Accuracies:*** *88.61% & 87.84%*
Kang et al. [128]	*Morphological features*	*64*	*Cerebral artery stenosis*	*LDA*	***Accuracy:*** *92.2%*
Väliaho et al. [129]	*Time-domain and morphological features*	*359*	*Atrial fibrillation*	*LR*	***Sensitivity, specificity:*** *96.4%, 96.3%*

One such study by Liu et al. [125] utilized 10-second PPG segments annotated by cardiologists against their corresponding ECGs exhibiting various arrhythmias, including sinus rhythm, premature ventricular contraction, premature atrial contraction, ventricular tachycardia, supraventricular tachycardia, and atrial fibrillation. A CNN model evaluated the segments, achieving 85% overall classification accuracy. In a separate study, Al Fahoum et al.

[126] employed seven distinct machine learning classifiers to sort PPG-derived features into two classes. The first class consisted of healthy subjects, while the second encompassed five different cardiovascular disorders: deep vein thrombosis, atrial fibrillation, acute coronary syndrome, heart failure, and cerebrovascular accident. The NB classifier demonstrated the best performance, attaining 94.44% classification accuracy.

Another study by Putra et al. [19] focused on the detection of CHD. They explored different feature selection methods to optimize the KNN model's performance, achieving an impressive accuracy of 90.9% using the Pearson Correlation selection method. Hackstein et al. [18] used NB and KNN classifiers with feature selection to predict aortic aneurysms, reaching 60% overall accuracy. Hosseini et al. [20] employed a set of time-domain PPG features in a KNN model to identify the risk of CAD, achieving an accuracy of 81.5%. De Moraes et al. [21] used time-domain input features to classify cardiopathies reaching an accuracy of up to 100% with MLP and KNN models.

Researchers have also explored the use of PPG signals for specific cardiovascular assessments. For example, Chiang et al. [127] utilized SVM to evaluate blood flow volume and the degree of stenosis at arteriovenous fistulas in individuals undergoing hemodialysis, achieving accuracies of 88.61% and 87.84%, respectively. Kang et al. [128] employed LDA on PPG features to identify cerebral artery stenosis subjects, achieving high classification rates of 93.8% sensitivity, 90.6% specificity and 92.2% accuracy. Additionally, Väliaho et al. [129] investigated the utility of ten PPG features for atrial fibrillation detection using LR, resulting in 96.4% sensitivity and 96.3% specificity.

Beyond disease-specific predictions, researchers have also explored the potential of PPG signals for broader cardiovascular risk classification (**Table II.2**). For instance, Soltane et al. [130] utilized dimensionally reduced PPG features to differentiate between healthy individuals and those at vascular risk. The study reported classification accuracies of 94.7% and 91.17% using MLP and GMM approaches, respectively. Shobitha et al. [131] investigated the classification of PPG data into healthy or at-risk of CVD categories. The researchers established 466 feature combinations and employed ELM and SVM classifiers to perform the task. The study achieved sensitivities of 90.33% and 91.33%, and specificities of 89.33% and 89.67%, for the ELM and SVM models, respectively. Ramachandran et al. [24] extracted PPG features through singular value decomposition, statistical analysis, and discrete wavelet transform, which were evaluated using a SDC and GMM, achieving an accuracy of 97.88% and 96.64%,

respectively. Prabhakar et al. [23] explored metaheuristic optimization methods to reduce PPG dimensionality before various classifier models, achieving 99.48% accuracy using ANN and LR classifiers. Palanisamy et al. [22] tested 12 classifiers on dimensionally reduced PPG waveforms, with harmonic search classifiers demonstrating 98.31% accuracy.

Table II.2. Cardiovascular risk classification systems.

Authors	***Features***	***Research subjects***	***Classifier***	***Performance***
Soltane et al. [130]	*Dimensionally reduced time-domain features*	*48*	*MLP* *GMM*	***Accuracy:*** *94.7%* *91.17%*
Shobitha et al. [131]	*Time-domain and morphological features*	*60*	*ELM* *SVM*	***Sensitivity, specificity:*** *89.33%, 90.33%* *89.67%, 91.33%*
Prabhakar et al. [132]	*Fuzzy-inspired and Dimensionally reduced features*	*42*	*KNN* *SVM* *MLP* *LR*	***Accuracy:*** *85.03%* *95.06%* *92.19%* *88.81%*
Ramachandran et al. [24]	*Statistical and wavelet features*	*42*	*SDC* *GMM*	***Accuracy:*** *97.88%* *96.64%*
Prabhakar et al. [23]	*Dimensionally reduced features*	*42*	*ANN* *LR*	***Accuracy:*** *99.48%* *99.48%*
Palanisamy et al. [22]	*Frequency-domain features*	*42*	*Harmonic search*	***Accuracy:*** *98.31%*

Beyond ML techniques, studies further emphasize PPG's potential for improving CVD management by providing diagnostic parameters including PR, PRV, RR, SI, JVP, and ABI among others [133].

PR and PRV measured via PPG are important vital signs for patient health assessment. PR provides a convenient, continuous heart rate monitor, a key indicator of cardiovascular status. Abnormal heart rates like bradycardia or tachycardia may indicate underlying conditions [134]. PRV correlates with HRV [135], linked to development and progression of various CVDs [136-138]. RR is another parameter that can be derived from PPG in a non-invasive manner [139-142]. RR is an important indicator of overall cardiovascular health, as it is closely coupled with the cardiovascular system. For example, heart failure is known to have a significant influence on the respiratory system [143], and studies have found that patients with poor left ventricular function often exhibit breathing disorders [144].

PPG has also shown promise in the assessment of arterial stiffness [145], a key marker of cardiovascular health. Studies have reported the effectiveness of PPG-derived SI in identifying patients at higher risk of future cardiovascular events [146, 147]. The JVP is also a useful parameter in diagnosing potential cardiovascular abnormalities [133], and different PPG designs have been explored to enable the non-invasive measurement of JVP with impressive results [148-151]. Additionally, the ability to estimate the ABI - the ratio of ankle to arm blood pressures - from PPG has been investigated [152, 153], as ABI is commonly used in assessing PAD and CAD [154].

Furthermore, the diagnostic potential of PPG and its derivatives has been investigated for a range of cardiovascular conditions [133]. The link between PPG derivatives and cardiovascular mortality has been reported in the literature [155]. Researchers have developed prototype PPG devices for the detection of HF [156], while others used PPG to monitor obstructive sleep apnea [157], and assessment of JVP [158] in HF patients. The identification of cardiac abnormalities, such as venous occlusion and HOCM, using PPG signals has also been explored [159, 160].

1.2. Potential Benefits and Technical Limitations of Existing Approaches

1.2.1. Shortcomings of Input Predictor and predictive capability

Current CVD research primarily focuses on leveraging the diagnostic value of PPG signals to enable early disease detection. This is achieved either through ML classifiers directly predicting disease (**Table II.1**), assessing CVD risk (**Table II.2**), or through ML-independent derivation of diagnostic parameters, as exemplified previously. While all these methods may contribute to CVD management, challenges remain regarding clinical decision support.

Specifically, ML classifiers addressing the prediction of particular diseases, such as those presented in [18-21, 125-129], may be useful in confirming already established diagnoses. However, these models do not offer a holistic perspective or guiding insights regarding the spectrum of possible cardiovascular conditions during initial screening. A more desirable approach would be the development of classifiers capable of differentiating between multiple potential CVDs, providing a comprehensive assessment and guidance on the probable etiologies.

Similarly, the CVD-risk assessment classifiers presented in [22-24, 130-132] provide limited information into the underlying causes driving these predictions, as their outputs do not suggest clear diagnostic plans due to the lack of etiological insights. In fact, the PPG inputs

involved in these studies are labeled based on observable respiratory signs like rebreathing, heart variability, and apnea [25]. Such a variety of symptoms can often result in a poor prognosis and delayed diagnosis [6]. Besides, risk-based systems overlook asymptomatic individuals as they rely on symptom-defined classes. Furthermore, despite established links between PPG-derived biomarkers—including PR, PRV, RR, JVP, ABI—and CVDs [133], their utilities remain limited, similar to the symptom-based and specific-disease classifiers.

Moreover, while predictive capacity is important, direct outputs irrespective of underlying logic limit explainability in clinical settings. For instance, the complexity of the optimization techniques used in [23, 130, 132] for feature extraction may be clinically irrelevant. Clinicians often prefer evidence-based, physiologically interpretable parameters over perfectly dimensionally reduced features that lack explanatory connections to the underlying cardiovascular mechanisms. Overall, maximizing the clinical translatability of ML demands intelligible, multi-condition predictions that guide comprehensive evaluation and management of cardiovascular diseases.

1.2.2. Challenges in Algorithm Selection

Selecting optimally capable, transparent and computationally efficient algorithms aligned to clinical needs and data characteristics remains an ongoing challenge in developing trusted medical classification systems. Techniques such as SVM, BLSTM, CNN, and GMM, have demonstrated impressive performance, as highlighted in [24, 125, 127, 130-132]. However, the intricacy of their internal structure and mechanisms poses difficulties in terms of interpretation and explanation.

For instance, BLSTM and CNN models operate as black-box models, making it exceedingly challenging to elucidate the rationale behind their predictions [161]. These DL models also exhibit high sensitivity to hyperparameter tuning, require extensive training datasets, and may inadvertently learn spurious correlations present in the data. Similarly, MLPs and other ANNs exhibit a high degree of complexity due to multiple hidden layers and numerous neurons, further complicating their interpretability. These architectures are also susceptible to potential convergence issues stemming from vanishing or exploding gradients during the training process [162].

SVMs introduce additional complexity, particularly when non-linear kernel functions are employed [163]. Challenges associated with SVMs include the selection of suitable kernel functions, handling imbalanced datasets, and the computational burden of solving the quadratic

optimization problem, especially for large-scale datasets. Furthermore, the complexity of GMMs increases as the number of components and the dimensionality of the data increase [164]. GMMs also face issues such as sensitivity to initialization, the necessity to specify the number of components, and a propensity for overfitting, particularly in high-dimensional spaces with limited data.

On the other hand, ML techniques such as LR, NB, KNN, and DTs, as created in [18-21, 126, 129, 132], may be more appropriate for such medical classification tasks. These algorithms offer several benefits that make them appealing choices in the context of healthcare applications.

LR is particularly valued for its straightforwardness and ease of interpretation, providing clear insights into the relationship between the dependent variable and one or more independent variables by estimating the probabilities of outcomes. This interpretability is crucial in medical applications where understanding the contribution of each variable is essential for clinical decision-making. However, the linear assumption of LR may not hold when the features are non-linearly linked to the targets, as evidenced in [132].

NB models, which are based on Bayes' theorem, are efficient and perform well with small to medium-sized datasets. NB models assume feature independence [165], which simplifies the computation and often leads to robust performance in high-dimensional spaces. NB models are especially effective in medical diagnosis applications where the conditional independence assumption may reasonably hold, making them both simple and powerful. However, the performance of NB models can be hindered if the independence assumption is violated, as evidenced by the low performance results in [18] when exploring different input features.

KNN is an instance-based learning algorithm that is intuitive and easy to implement [166]. Unlike LR and NB, KNN makes no assumptions about the underlying data distribution, making it a versatile choice for various types of data. It makes predictions based on the closest training examples in the feature space [167], which can be particularly intuitive in clinical settings where similar cases are expected to have similar outcomes. This explains the prevalent use of this algorithm in current research [18-21, 126, 132]. The ability of KNN to adapt to the complexity of the data through the selection of the parameter 'k' allows for flexibility in achieving a balance between bias and variance. KNN does not require a training phase, which can be an advantage in terms of computational efficiency, although it can be slower during prediction as it requires calculating the distance to all training examples.

DT models are highly interpretable, as they provide a clear, visual representation of decision rules based on the features [168, 169]. DTs can handle both numerical and categorical data, making them versatile for different types of medical data. They are also capable of capturing non-linear relationships between features and the target variable, making them suitable for various types of classification tasks. However, DTs can be prone to overfitting, especially with deep trees, which can be mitigated through techniques like pruning.

Ultimately, the choice of the most appropriate model depends on the specific requirements of the clinical task, the nature of the data, and the need for model interpretability in medical decision-making.

1.2.3. Dataset Constraints and Lack of Diversity

To ensure effective CVD classification, datasets should encompass comprehensive representation of varied pathologies. However, the previously discussed studies [18-20, 125-129] appear to be biased towards specific disease categories, with the most diverse datasets covering only three [21] or five [126] CVD categories. Notably, the latter dataset was improperly evaluated, with all pathologies sorted into a single class versus healthy. Additionally, at-risk CVD studies using heterogeneous respiratory symptom annotations [25] provide insufficient insight for risk prediction. Such inadequate data representation can lead to suboptimal model performance and limited generalizability.

Moreover, sufficient sample size is also crucial for training and evaluating robust ML models. While size requirements may vary depending on the task complexity and the chosen ML algorithm, larger datasets tend to yield more generalizable models resistant to overfitting. However, prior studies were limited by small sample sizes (see **Tables II.1-2**), potentially leading to overfitting and poor performance when deployed in real-world clinical settings. Addressing these data representation and sizing issues will be important to develop models capable of reliably distinguishing the full spectrum of CVDs with high accuracy.

1.2.4. Ineffective Optimization Strategies

Achieving optimal model performance and generalizability crucially relies on determining parameter configurations yielding highest predictive capability. This is conventionally realized via internal or external optimization approaches. Internal optimization involves fine-tuning the model's hyperparameters using techniques such as grid search, random search, Bayesian optimization [170]. On the other hand, external optimization focuses on enhancing the model's predictive ability by identifying the most contributory feature subsets. This can be

accomplished through dimensionality reduction using metaheuristic optimization, transformation, or feature selection methods.

For instance, Hosseini et al. [20] applied sequential floating selection to dimensionally compress PPG data before empirically determining k=8 yielded maximal KNN accuracy. Similarly, De Moraes et al. [21] experimentally evaluated diverse MLP hyperparameter configurations and modified KNN's k value from 3 to 7 for different classification tasks. Prabhakar et al. [23] dimensionally reduced PPG data via probabilistic, search-based and model-based metaheuristics. Ramachandran et al. [24] applied dimensionality reduction techniques to preprocess PPG data. Singular value decomposition compressed 144,000 PPG samples to 7,200. Discrete wavelet transforms using db4, Haar and sym8 wavelets reduced 200-sample PPG segments to 13, 7 and 20 samples respectively. Additionally, expectation-maximization optimized the GMM model, estimating parameters from the probabilistic modeling of PPG data as a combination of Gaussian distributions.

Furthermore, Väliaho et al. [129] implemented a backward feature selection process to determine independent and statistically significant features. Prabhakar et al [132] dimensionally reduced fuzzy-inspired PPG representations via nature-inspired heuristics, including differential search, shuffled frog leaping, wolf search and animal migration optimization. Al Fahoum et al [126] leveraged data-mining to extract classifiers' most predictive attributes. Palanisamy et al [22] optimized PPG via Hilbert transform, nonlinear regression and metaheuristics including artificial bee colony, particle swarm, cuckoo search and dragonfly optimization.

However, while the reviewed studies have significantly advanced CVD classification using PPG data through feature optimization, several limitations and shortcomings merit further consideration. A primary focus has been dimensionality reduction via metaheuristic, transformational and feature selection techniques. However, internal model parameter optimization has generally relied on arbitrary or empirical approaches like trial-and-error, sweeping, and predefined values. For example, some determined KNN k-values and MLP parameters through experimentation without systematic optimization [18, 20, 21]. Similarly, GMM parameters were set via expectation-maximization without rigorous tuning methodology [24]. This reliance on trial-and-error or heuristic-based parameter tuning, rather than a more systematic and principled approach, raises concerns about the robustness and generalizability of the developed models. Incorporating validation techniques or Bayesian optimization can

better ensure configurations align with underlying data characteristics rather than result from arbitrary adjustment.

Nevertheless, the exclusive focus on performance maximization through extensive feature engineering and parameter optimization can lead to increasingly complex 'black-box' models. While this may be acceptable for consumer-oriented systems where the primary concern is profiling health status, in the healthcare domain, where trust and transparency are paramount, model interpretability and reliability are equally important. Simpler models with carefully calibrated internal structures may prove more clinically appropriate. Incorporating XAI methods like feature importance analysis, better fulfills clinical needs relative to maximizing prediction alone. By addressing these limitations and shifting the focus towards developing interpretable, simplified yet optimized models can significantly advance clinical decision-making and ultimately improving patient outcomes.

2. The Proposed Classification System

Considering the limitations of current CVD classification systems in fully meeting clinical needs and enabling personalized screening applications, we propose a new arterial pressure classification system. This system utilizes exclusively PPG signals for noninvasive multi-purpose prediction.

Current systems are either focused solely on specific CVD prediction or broad CVD risk profiling. To address this, our proposed system predicts AAP patterns which have established clinical associations with various CVDs. This includes anacrotic, bisferiens, dicrotic, deep, tardus, parvus et tardus, bounding and water hammer patterns. By providing this multidimensional output, the aim is to guide healthcare professionals towards more targeted clinical insights beyond singular profiling.

However, achieving this multi-purpose predictive capability requires high performing classifiers. This generally leads preferences for complex nonlinear models, which can lack clinical relevance. Rather than solely optimizing internal model complexity, we first aim to enhance the input predictors by precisely extracting features tied to underlying cardiovascular physiology. Subsequently, we will apply feature selection techniques based on importance analysis to refine the feature set, as will be discussed further in upcoming sections.

For consumer-oriented personalized health monitoring systems, interpretability of internal logic may be less crucial compared to identifying potential health issues prompting users to

seek medical advice. In this context, features will be extracted using advanced transformation methods and compressed via statistical and metaheuristic optimization techniques. The goal is to boost predictive performance for self-screening applications.

We also propose leveraging the classification capabilities of ML models to improve BP estimation. Current approaches broadly assign target BP values across wide ranges, requiring extensive analysis to reduce model variance errors. Narrowing target ranges may improve stability but raises concerns for values outside those ranges. Our classifier aims to provide additional granularity by classifying BP into narrow discrete ranges. This focuses regressor training within more targeted BP values, forcibly reducing error variances. This approach will not only yield accurate BP estimates but also precisely classify AAPs and hypertension status. However, achieving this still requires development of highly accurate classification models. Therefore, a novel external optimization approach explored in later sections aims to address this challenge.

The following subsections will further discuss the proposed classifier concept, highlighting the input/output system considerations and the overall classification architecture.

2.1. System inputs

2.1.1. Clinical Considerations

PPG sensors provide an affordable and convenient input option that makes them highly suitable for the proposed arterial pressure classification system. Like arterial pressure waveforms, PPG waveforms contain systolic and diastolic phases as well as distinguishable characteristic points including the systolic peak, dicrotic notch, dicrotic wave, and diastolic foot. Due to the close correlational and morphological similarities between PPG and arterial pressure waveforms [32], features extracted from PPG signals could significantly benefit this multi-task focused classification system. Physiologically meaningful and clinically relevant features may be derived from PPG waveforms through either temporal or waveform-based analytical approaches.

For instance, previous research has demonstrated connections between BP and features that can be captured from the second derivative of the PPG signal (APG) [171,172]. Specifically, a study reported ratios of b/a and d/a from APG waveforms as potential indicators of arterial stiffness and arteriosclerosis associated with elevated intravascular pressure (see **Figure II.1**) [173]. Additionally, Addison declared the STT, the ratio between systolic upstroke duration and amplitude, correlates with blood pressure [174]. Other researchers have analyzed

temporal characteristics between different PPG characteristic points, as illustrated in **Figure II.2**, to extract features [175]. Whether focused on morphological or temporal aspects, this type of analytical approach is founded upon solid physiological evidence and could facilitate clinical translation.

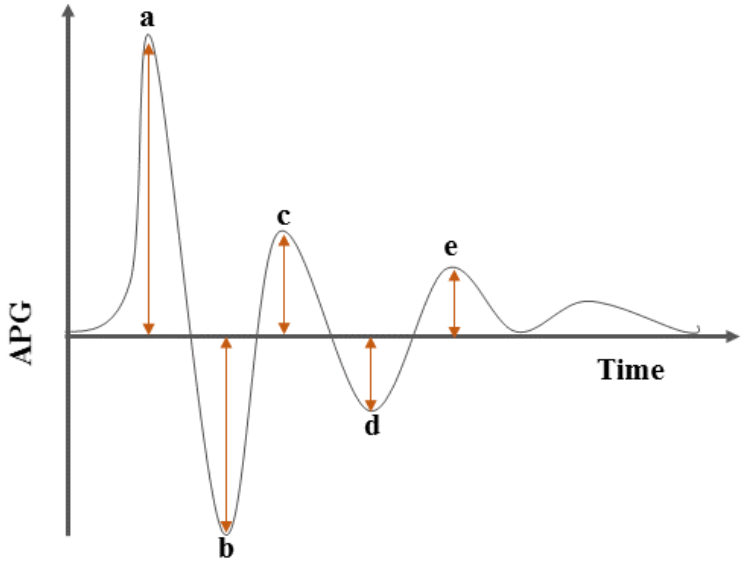

Figure II.1. APG waveform features

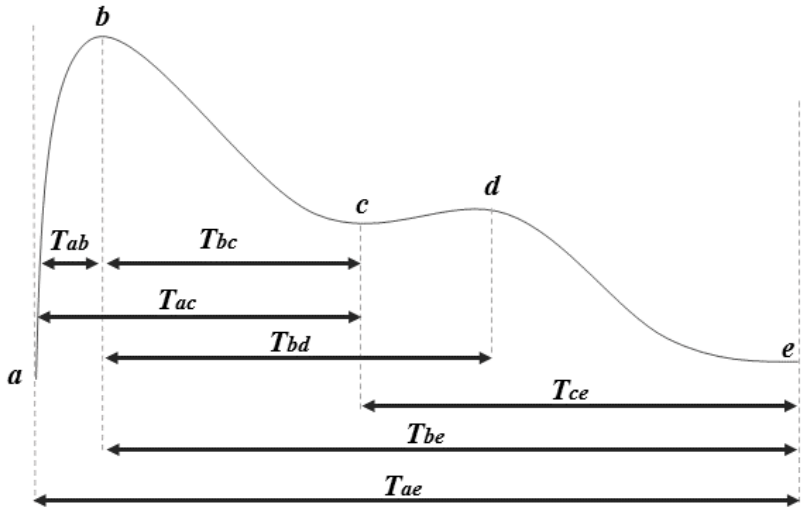

Figure II.2. Time-domain features

The features incorporated into the proposed classification framework will encompass evaluations of both waveform and temporal attributes to optimize predictive performance. However, the informativeness of PPG waveforms can sometimes be hindered by factors such as the influence of age on dicrotic notch prominence [176]. An additional challenge stems from potential signal quality degradation due to PPG's susceptibility to motion artifacts [38]. These issues will be addressed in subsequent chapter through customized detection algorithms and an

artifact screening method based on signal quality assessment during data collection, respectively.

2.1.2. Personalized Monitoring

Systems designed for personal use may differ from clinical models in their design priorities and goals. For asymptomatic individuals without overt signs or symptoms of CVD/hypertension, highly accurate ML systems that are somewhat less interpretable could still effectively serve as self-screening tools. By leveraging the ubiquitous presence of PPG sensors in wearable devices like smartwatches [177], individuals could conveniently monitor their cardiovascular health metrics anywhere and anytime. This has the potential to enhance early disease detection and drive improved long-term health outcomes, even in the absence of medical expertise that could critically evaluate the internal logic and workings of the underlying models. In this context, for the average user, the primary concern is identifying potential health risks early, rather than attempting to dissect the detailed algorithmic mechanisms. A system optimized purely for classification accuracy, rather than interpretability, may therefore prove quite valuable for this type of widespread consumer-driven health screening application.

Given this context and purpose, utilizing dimensionality reduction techniques like metaheuristic optimization or signal transformation methods to extract features could prove feasible and worthy of exploration. Considering past research demonstrating the high-performance benefits of such approaches [22, 23, 130], our objectives are to experimentally evaluate the potential of metaheuristic optimization techniques to further boost the learning and predictive abilities of our classification models. Additionally, to help address potential degradation issues with PPG signal quality, TF transforms will be applied as the feature extraction method rather than more complex morphological analyses.

PPG signals exhibit non-stationary properties due to the time-varying physiological processes that generate them [36]. Traditional Fourier analysis faces challenges dealing with these signals since their frequency content changes over time [178]. In contrast, TF analysis techniques are well-suited for capturing the time-varying spectral information obscured by conventional methods. Among these, the STFT is widely used for addressing this challenge using fixed-size windows [179], as demonstrated in past studies applying it successfully to BP classification from PPG [36]. The STFT calculates local frequency content via the given equation:

$$V_S^D(t,\gamma) = \int_{-\infty}^{+\infty} S(\alpha) D(\alpha - t) e^{-2i\pi\gamma(\alpha - t)}\, d\alpha \quad (1)$$

where, *S(α)* is the input signal, *D(t)* represents the window function, *t* denotes the time index, γ corresponds to frequency, and α serves as a time-variable of integration.

However, it introduces a trade-off between time and frequency resolution due to the fixed window sizes [180], limiting its ability to effectively represent rapid changes that often appear in non-stationary signals like PPG. Therefore, we will investigate alternative time-domain reassignment approaches, such as FSST [178], to help address this disconnect between time and frequency information.

Transforming PPG signals using TF analysis generally results in sizable datasets, which could be computationally inefficient if used directly as features. Additionally, outliers may be incorporated. Therefore, the proposed optimization techniques aim to reduce the dimensionality of these transformed PPG datasets into potentially more compact yet still information-rich feature sets. Statistical measures like kurtosis, skewness, mean and STD will also be explored for feature engineering purposes.

2.2. System Outputs

2.2.1. Abnormal Pulse Pattern Identification

An underexplored area that may address current limitations in CVD classification output involves the use of arterial pressure waveform morphologies [28]. A range of AAP patterns have demonstrated strong correlations with potential CVDs [27-29]. However, the lack of comprehensive guidelines for analyzing such abnormalities makes identification challenging, requiring clinical expertise [26]. The only approach to understanding these abnormalities involves examining pathologies commonly manifesting with such patterns. Clinical literature has presented various theories and criteria for AAP analysis through diverse pathological case studies. Accordingly, AAP models will be created following in-depth analysis of past studies revealing these morphologies.

The proposed AAP modeling approach will employ a variety of preprocessing techniques for comprehensive waveform characterization:

***Temporal analysis**, assessing the time domain, will detect abnormalities in the duration to pressure peaks. Specifically, shortened peak times may indicate a water hammer pattern, while delayed times suggest tardus, parvus et tardus, or slow-bounding morphologies.*

***Amplitude analysis**, evaluating the pressure domain, will identify abnormalities in pulse pressure widths. Narrowed pulse pressures could represent a parvus et tardus pattern, whereas widened pressures may signal a bounding morphology.*

***Contour examination**, analyzing the shape domain, will reveal morphologic deviations. For example, sharp waveforms could characterize a water hammer pulse. Enlarged dicrotic wave components may typify a dicrotic pulse. Additionally, double pressure peaks may denote anacrotic or bisferiens patterns.*

Through multi-dimensional temporal, amplitude, and contour profiling, this modeling scheme aims to capture the full spectrum of potentially pathological AAP variations revealed via extensive case study evidence. Comprehensively phenotyping AAP morphologies in the time, pressure, and shape domains may facilitate more precise cardiovascular correlation and enhanced classification accuracy. Once modeling is finalized, PPG features will be easily labeled according to their synchronous AAP pattern. This novel AAP modeling framework based on extensive clinical evidence has the potential to advance CVD classification output by capturing hemodynamically-relevant morphologies indicative of disease correlates. Nevertheless, the proposed approach merits thorough investigation to realize this potential.

2.2.2. Blood Pressure Level Classification

To address limitations in BP measurement and poor public understanding of acceptable BP values [123,124], two complementary classification approaches will be explored.

The first approach involves predicting discrete BP ranges for SBP, DBP, and MAP spanning narrow, predefined values. By training ML estimators to operate within confined ranges, the outcome error can be deliberately controlled by the classifiers. Producing outputs in discrete BP ranges in this way allows for constrained BP estimation.

The second method classifies BP into standard categories of hypertension, prehypertension, and normotension defined by JNC7 guidelines [181] (see **Table II.3**). By producing standardized BP classifications, this aims to improve hypertensive patients' comprehension of dangerously high values threatening health status.

Table II.3. JNC 7 blood pressure classification standards [181].

Blood pressure level	*Systolic blood pressure (mmHg)*		*Diastolic blood pressure (mmHg)*
Normotension	*< 120*	*and*	*< 80*
Prehypertension	*[120 to 140 [*	*or*	*[80 to 90 [*
Hypertension	*> 140*	*or*	*> 90*

2.3. System Architecture

This research endeavors to explore the utilization of PPG signals for the development of a ML-based classification system capable of producing multiple, clinically-relevant arterial pressure-related outputs.

The proposed system will employ PPG signals as the primary input, as depicted in **Figure II.3**. The data preprocessing stage will involve artefact screening and filtering to ensure signal quality. A multifaceted feature extraction process will be employed, involving temporal, morphological, and TF transformations of the PPG data. To optimize the informativeness of the inputs, dimensionality reduction techniques, including metaheuristic optimization and statistical measures, will be utilized to compact the FSST transform into efficient feature sets. Additionally, feature selection methods will be adopted to identify the most contributory temporal and morphological features.

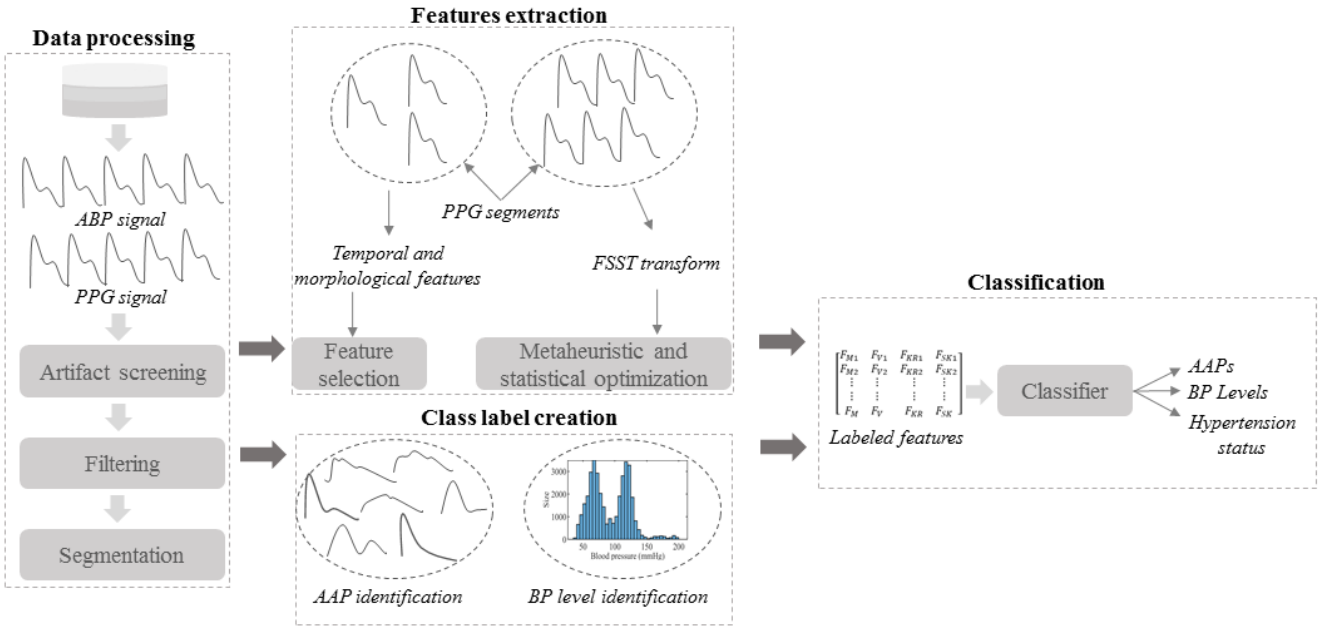

Figure II.3. Block diagram of the proposed system

The optimized PPG inputs will then be used to train multiple ML classifiers, each targeted at distinct classification tasks. Firstly, pre-identified AAP models, developed through extensive waveform profiling methods, will decode the PPG features according to synchronous arterial pressure morphologies. Complementary to the AAP classification, the system will also incorporate BP level prediction models. These models will produce outputs in the form of both predefined ranges for BP estimations and standardized categories defined by clinical guidelines for hypertensive risk classification.

By integrating these diverse cardiovascular assessment capabilities, the proposed system aims to deliver a comprehensive and clinically-relevant solution for early detection, risk stratification, and personalized management of CVDs.

3. Experimental Design and Methodological Considerations

3.1. Dataset Development and Curation

3.1.1. Data Collection

A suitable dataset containing synchronous PPG and intra-arterial pressure recordings will be required to develop and evaluate the proposed multi-output classification models. The following characteristics should be present:

Subject Cohort: *Recordings should be obtained from a reasonably sized (anticipated n > 200) and demographically diverse patient cohort to facilitate generalizability of modeling efforts.*

Signal Acquisition: *PPG signals should be captured at sampling frequencies of 100Hz or higher for extended durations (several minutes) to permit robust preprocessing. Simultaneous high-fidelity (≥100Hz) arterial pressure tracings directly measured from peripheral arteries will supply ground truth waveforms for precise abnormal arterial pulse modeling and blood pressure extraction.*

Synchronization: *Contemporaneous capture of PPG and intra-arterial signals is necessary to characterize relationships between signal types for this research.*

Population Coverage: *Representation of the full spectrum of normotensive and pathological BP levels/categories as well as diverse arterial pulse morphologies is important for comprehensive model formulation.*

Data Integrity: *Recorded data must undergo rigorous quality control protocols including preprocessing techniques to filter noise, motion artifacts, and validate reliable acquisition prior to use.*

Sample Size: *An adequate sample volume (e.g. thousands of recordings) is recommended to facilitate development of generalizable multi-output classification models.*

Publicly accessible datasets meeting these criteria will be explored to obtain suitably sized, diverse synchronized PPG-arterial datasets capable of advancing the objectives of this research initiative. One publicly available dataset that would be well-suited to meet the above criteria is

the MIMIC-III waveform database. MIMIC-III contains de-identified health data including physiological waveforms collected from over 40,000 intensive care unit patients [182]. Within MIMIC-III is a wealth of longitudinal high-fidelity cardiovascular recordings, including synchronized multi-parameter waveforms captured at 125Hz such as ABP, PPG, and ECG. The diversity of patients, ranging from healthy volunteers to severely ill populations, would allow for modeling across a wide spectrum of hemodynamic states.

At over 200GB in size and comprising millions of waveform samples, MIMIC-III far surpasses the anticipated sample size needs. Its standardized format and documentation would facilitate efficient data preprocessing and model training. Most importantly, the inclusion of direct arterial line pressure as ground truth, synchronized with other waveforms on a massive scale, uniquely positions MIMIC-III to address the core needs of this research for paired PPG and intra-arterial datasets. For these reasons, the extensive collection of synchronized cardiovascular waveforms contained within the publicly available MIMIC-III database is proposed as an ideal candidate dataset to supply the necessary training and evaluation data required to develop and validate the proposed multi-output classification models.

3.1.2. Features Extraction Strategies

This research aims to explore and evaluate a comprehensive set of PPG-derived features, encompassing physiological, time-domain, and TF domain analyses, to enhance the predictive capabilities of the proposed classification system.

PPG's physiological information will be extracted by leveraging changes occurring at specific cardiac cycle landmarks. The PPG pulse will first be segmented at key temporal markers including onset, peak, dicrotic notch, and offset (**Figure II.4**). These cutoff points delineate the start and end of discrete cardiac phases. Onset indicates systole initiation while the peak signifies mid-systole. The dicrotic notch denotes the systole-diastole transition and offset concludes the cardiac cycle. By segmenting the PPG pulse at these physiological landmarks, six distinct sub-waves can be obtained, each characterizing a particular cardiac event. The duration between each pair of landmarks will be measured, generating six time-domain features that provide insights into the temporal dynamics of the cardiac cycle.

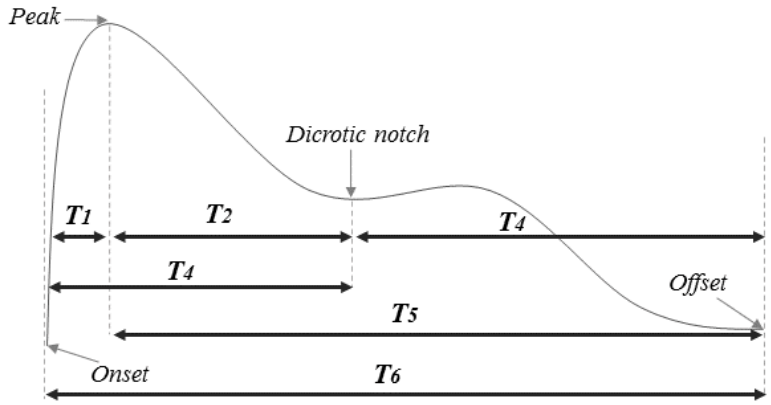

Figure II.4. The proposed time-domain features

Furthermore, the morphological variations within the segmented waveforms can be considered as a result of statistical influences over time [26]. Considering each sub-wave as a normal probability distribution, statistical metrics such as kurtosis and mean will be employed to quantify waveform morphology on a more quantitative basis. For instance, the kurtosis of the waveform can describe the extension of the tail regions compared to a normal distribution (**Figure II.5**) [183], while the mean can be used to measure the central tendency of the waveform's statistical components.

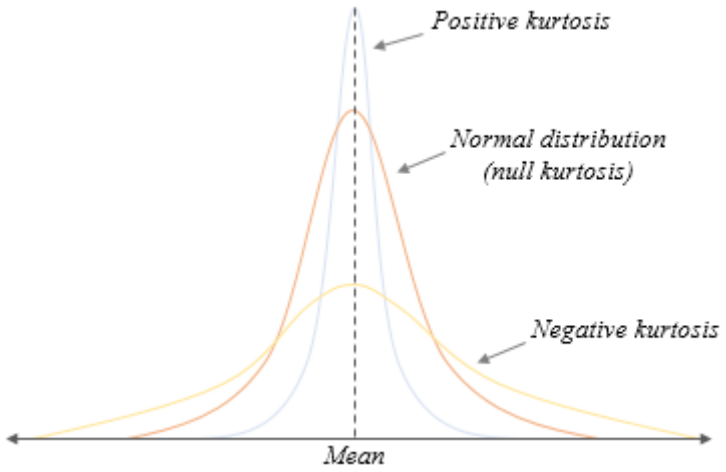

Figure II.5. Kurtosis morphological measurement

PPG signals are inherently non-stationary, exhibiting time-varying properties arising from dynamic physiological processes [36]. Analyzing the obscured temporal modulations in the TF domain can yield more informative insights. To fully leverage these informative temporal changes, the research will employ the FSST to analyze the PPG signals. The FSST offers an innovative solution to the classical tradeoff between time and frequency components in STFT analysis. The FSST can be expressed as:

$$T_S^D(t,\omega) = \int_{-\infty}^{+\infty} V_S^D(t,\gamma)\delta(\omega - I_S(t,\gamma))\, d\gamma \tag{2}$$

where $\delta(\omega)$ is the Dirac distribution, and $I_S(t,\gamma)$ denotes the instantaneous frequency estimation at time t and frequency γ, calculated using the following expression:

$$I_S(t,\gamma) = \frac{\partial \arg V_S^D(t,\gamma)}{\partial t} = \mathbb{R}\left\{\frac{1}{2i\pi}\frac{\partial t\, V_S^D(t,\gamma)}{V_S^D(t,\gamma)}\right\}, \tag{3}$$

$$such\ that\ V_S^D(t,\gamma) \neq 0$$

By applying a non-linear postprocessing mapping to the STFT [184], the FSST facilitates signal interpretation through the redistribution of energy and provides robust visualization and manipulation capabilities [185]. This integration results in an improved representation of the TF components, enabling the extraction of more informative features from the PPG signals. A visual comparison between FSST and STFT resolution for a PPG signal is shown in **Figure II.6**.

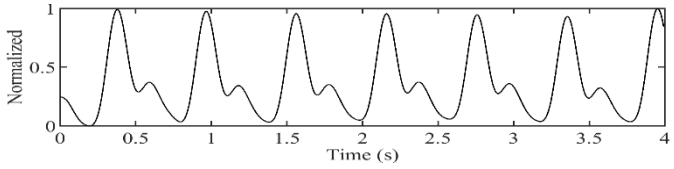

(a) PPG signal

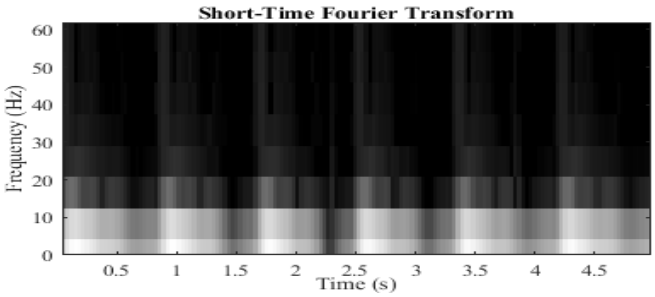

(b) Short-time Fourier Transform

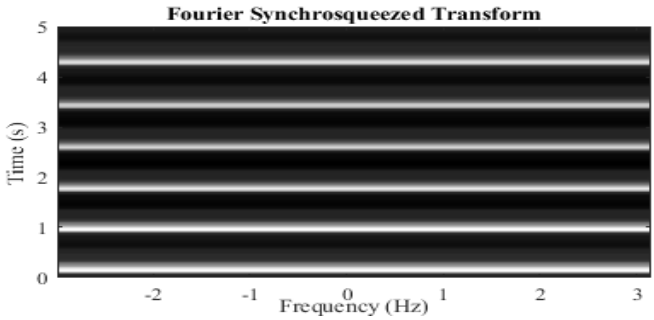

(c) Fourier Synchrosqueezed Transform

Figure II.6. Time-frequency representations of a PPG signal

3.1.3. Metaheuristic Optimizations

The process of dimensionality reduction is employed as a preprocessing step to remove irrelevant and redundant information from PPG datasets, thereby decreasing the computational demands and training time of the ML models. The FSST generates high-dimensional TF components, which makes them unfeasible to utilize as features. Training an ML model on large features dimensions may lead to the model becoming excessively abundant, which can result in mediocre performance outcomes. Given this, it becomes imperative to diminish the number of features, a task that can be carried out via dimensionality reduction. Consequently, this study intends to investigate a metaheuristic-based optimization technique named cuckoo search.

The cuckoo search optimization algorithm can be effectively leveraged to identify the most informative subset of PPG features and reduce the overall dimensionality of the feature space. The algorithm's random walk mechanism via Lévy flights allows it to explore a wide range of feature combinations [186], while the selective pressure towards the best solutions helps converge on the optimal feature subset. By treating each candidate solution as a vector of binary values representing the inclusion or exclusion of specific PPG features, the cuckoo search can iteratively update these vectors to minimize the dimensionality of the feature set while preserving the most relevant information for the targeted arterial pressure assessment tasks. This dimensionality reduction through cuckoo search optimization can help improve the training efficiency and generalization performance of the ML models built upon the PPG data.

3.1.4. Feature Importance Analysis

While the use of waveform and temporal analysis to extract PPG-features can produce clinically meaningful information, it does not necessarily imply that all the extracted features will perform equally well within the classifier. It is therefore imperative to assess the relative importance of the extracted features in order to determine the most impactful ones. As a result, the study will implement the MRMR algorithm [187] as the primary feature selection approach.

MRMR method proved to be efficient in obtaining the nonrepetitive feature subset [188]. The MRMR algorithm identifies an optimal subset of features that are highly distinct from one another while still effectively representing the target variable. The algorithm operates by simultaneously reducing the redundancy within the feature set and increasing the relevance of the features to the dependent variable. Relevance and redundancy are quantified using mutual

information [189, 190], which measures the amount of information one variable provides about another.

Specifically, the relevance D of a feature x_i to the target variable c is given by the mutual information $I(x_i; c)$, defined as:

$$I(x_i; c) = p(x_i, c)\log(\frac{p(x_i, c)}{p(x_i)p(c)}) \quad (4)$$

where $p(x_i, c)$ is the joint probability distribution function of x_i and c , and $p(x_i)$ and $p(c)$ are the marginal probability distribution functions of x_i and c , respectively.

The redundancy R of a feature x_i with respect to a set of already selected features S is given by the average mutual information between x_i and each feature in S [190]:

$$R(x_i) = \left(\frac{1}{|S|}\right)_{x_j \epsilon\, S} I(x_i; x_j) \quad (5)$$

The MRMR score for a feature x_i is defined as the difference between its relevance and redundancy, known as Mutual Information Difference [189]:

$$MRMR(x_i) = I(x_i; c) - \left(\frac{1}{|S|}\right)_{x_j \epsilon\, S} I(x_i; x_j) \quad (6)$$

3.2. Machine Learning Modeling

3.2.1. Clinical-oriented Machine Learning Algorithms

Unlike many other areas, the concept of explainability is of utmost priority when deploying AI systems in the healthcare industry [37]. In the pursuit of XAI for healthcare applications, researchers investigating the communication of clinical AI decision-making and reasoning favor algorithms that possess more transparent and interpretable internal representations [191]. Opting for ML techniques that retain a level of interpretability in their internal operations allows XAI researchers to more effectively explore, evaluate, and clearly articulate the functioning of these models.

Parametric models inherently tend to possess a less complex and more interpretable structure [192]. The connection between variables in parametric models is explicitly specified by a set of parameters. However, the simplistic nature of such models may constrain their ability to effectively represent the intricate and nonlinear relationships present within PPG signals. For

instance, in the case of NB classifier, the underlying assumption is that the features are conditionally independent, given the class variable [165]. Discriminant analysis classifiers also operate under the assumption that the features align with a predetermined probability distribution for each class [193]. These conditional independences may not be valid for tasks involving physiological signals such as PPG, as the features in these signals can display intricate interdependencies.

Conversely, non-parametric models are more adaptable and can model complex relationships in the data without making restrictive assumptions. DTs are non-parametric models that have the ability to manage nonlinear dependencies between the variables. The decision-making process of this algorithm is highly interpretable, as it is based on a hierarchical structure of explicit rules [169]. However, using a single DT to learn from a sizable dataset may result in deeper or more complex tree structures, which could undermine the interpretability of the model and elevate the potential for overfitting. Ensemble approaches like bagging, which incorporate multiple DTs, may offer improved performance while preserving interpretability to a reasonable extent. Bagging entails training multiple DT models, each on a different portion of the training data, and merging their outputs to arrive at the ultimate predictions [194]. A key benefit of bagging is that it lowers the variance of the individual decision trees, which ultimately aids in preventing overfitting [195].

KNN represents another non-parametric modeling technique. It is considered a "instance-based learning" or "lazy learning" approach, as it does not entail explicit training or creating a model in the same manner as many other algorithms [196]. The core idea behind KNN is to store all the training cases and then classify new instances by assigning them to the same classes as their closest neighbors in the training set.

The fundamental concept is that cases which are located near each other typically possess similar feature values [167]. The KNN algorithm requires the specification of just two parameters: the number of neighbors (K) to consider from the training data, and the distance function (distance metric) used to measure the proximity between a new case (query point) and its K closest neighbors. A basic distance metric that could be leveraged for distance measurement in the KNN algorithm is the city block distance, or Manhattan distance. The Manhattan distance between two points $X = \{X_1, X_2, \dots\dots, X_D\}$ and $Y = \{Y_1, Y_2, \dots\dots, Y_D\}$ in a D-dimensional space is calculated as:

$$CityBlock(X,Y) = \sum_{i=1}^{D} |X_i - Y_i| \quad (7)$$

Where the absolute difference between each corresponding coordinate is summed up to obtain the final distance.

To enhance the prediction for the query point, weights can be assigned to the neighboring points, such that the nearest neighbor exerts a greater influence on the output class [167].

The weight assigned to each neighboring point in KNN can be calculated as the inverse of the square root of the distance between the query point and that neighboring point. Mathematically, the weight for a neighbor x can be expressed as:

$$Weights(X,Y) = \frac{1}{\sqrt{CityBlock(X,Y)}} \quad (8)$$

3.2.2. Consumer-oriented Machine Learning Algorithms

When addressing large biomedical datasets, DL algorithms are often preferred to ML due to the former's ability to model high-dimensional, complex phenotypes [39]. However, deep learning's flexibility demands significant computational resources that introduce deployment barriers. DNN require extensive memory storage to house vast numbers of network weights resulting from convolutional and activation layer operations during training [40]. Inference also necessitates powerful GPU to rapidly compute these computationally intensive layers. Such specialized hardware constraints run counter to deploying individualized risk stratification models on resource-constrained wearable devices meant to enhance population health monitoring capacity.

In contrast, ML training involves less computationally complex optimization of a relatively small number of learned variables, allowing for utilization of basic CPUs. Trained ML models primarily comprise lightweight hyperparameters rather than extensive internode connections, thereby reducing storage needs and expediting inference procedures. This renders ML a viable candidate for designing an affordable, clinically impactful continuous BP monitoring solution suitable for integration into consumer-grade mobile health technologies.

3.2.3. Recap of Machine Learning Modeling Approaches

KNN and BT, being non-parametric classifiers, provide more intuitive solutions for nonlinear problems due to their simpler architecture, in comparison to other more sophisticated

classifiers like kernel-based SVMs [163] or DNN [161]. Meanwhile, this nonlinear adaptability may enable them to achieve higher performance than parametric models, while still maintaining a certain level of simplicity. Accordingly, we intend to validate the effectiveness of the BT and KNN classifiers by comparing their performance against other classification models, including both parametric models such as NB, LDA, and SVM, as well as non-parametric models such as DT.

3.3. Multi-Objective Optimization Strategy

3.3.1. Performance Maximization using Bayesian Algorithm

Bayesian optimization is a powerful algorithm used for tuning ML models, particularly when the evaluation of the objective function is expensive [41]. It leverages Bayes' theorem to model the objective function and guide the search for optimal hyperparameters.

(1) Bayesian Optimization Framework

Objective Function: The function $f(x)$ we aim to optimize, where x represents the hyperparameters.

Probabilistic Model: GP is used as a surrogate model to approximate the objective function $f(x)$.

(2) Gaussian Process

A GP is defined as a collection of random variables, any finite number of which have a joint Gaussian distribution [197]. It is fully specified by its mean function $\mu(x)$ and covariance function $k(x, x')$.

- Mean function:

$$\mu(x) = E[f(x)] \tag{9}$$

- Covariance function:

$$k(x, x') = E[(f(x) - \mu(x))\,(f(x') - \mu(x'))] \tag{10}$$

Given a set of observations $D = \{(x_i, y_i)\}_{i=1}^{n}$, where $y_i = f(x_i) + \varepsilon$ and ε is the noise the GP is updated to reflect the posterior distribution over functions.

(3) Bayesian Updating

The posterior distribution is obtained by combining the prior distribution (the GP) with the likelihood of the observed data. The posterior mean U_n and variance σ_n^2 at a new point x are given by:

$$U_n(x) = k(x, X)[K + \sigma^2 I]^{-1} y$$
$$\sigma^2(x) = k(x, x) - k(x, X)[K + \sigma^2 I]^{-1} k(X, x) \quad (11)$$

where $X = [x_1 \dots\dots\dots, x_n]^T, y = [y_1 \dots\dots\dots, y_n]^T$, K is the covariance matrix with $K_{ij} = k(x_i, x_j)$ and σ^2 is the noise variance.

(4) Acquisition Function

The acquisition function $\alpha(x. D)$ is used to determine the next point to evaluate. It balances exploration (sampling points where the model is uncertain) and exploitation (sampling points where the model predicts high values).

Common acquisition functions include:

- ***Expected improvement (EI):***

$$\alpha_{EI}(x) = E[\max(0, f(x) - f(x^+))] \quad (12)$$

where $f(x^+)$ is the best observed value.

- ***Probability of Improvement (PI)****:*

$$\alpha_{PI}(x) = \varphi \frac{\mu(x) - f(x^+) - \xi}{\sigma(x)} \quad (13)$$

where φ is the CDF of the standard normal distribution, $\mu(x)$ and $\sigma(x)$ are the mean and standard deviation of the GP at x, and ξ is a trade-off parameter.

- ***Upper Confidence Bound (UCB)****:*

$$\alpha_{UCB}(x) = \mu(x) - k\sigma(x) \quad (14)$$

where k is a parameter balancing exploration and exploitation.

(5) Algorithm

- **Initialization:** Select an initial set of hyperparameters $\{x_i\}_{i=1}^{n}$ and evaluate the objective function to obtain $\{y_i\}_{i=1}^{n}$.
- **Modeling:** Fit a Gaussian Process to the observed data $D = \{(x_i, y_i)\}_{i}^{n} = 1$.
- **Acquisition:** Use the acquisition function to select the next point $x_n + 1$.
- **Evaluation:** Evaluate the objective function at $x_n + 1$ obtaining $y_n + 1$.
- **Update:** Augment the dataset with the new observation $D = D$ U $\{(x_{n+1}, y_{n+1})\}_{i}^{n} = 1$
- **Iteration:** Repeat steps until convergence or a predefined budget is exhausted.

3.3.2. Minimization Through Features Redundancy Vote

The human cardiovascular system exhibits inherent dynamic changes over the cardiac cycle, resulting in pulsatile waveforms. The repetitive nature of the pulse signal within a specific time period could be leveraged to optimize the classification task outcomes, as illustrated in **Figure II.7**. Typically, the majority of current evaluation approaches follow a similar basic methodology. This includes testing the created model using the same training predictors. However, this approach may generate performance metrics based on a single feature sample, which could introduce prediction errors due to potential outlier interference.

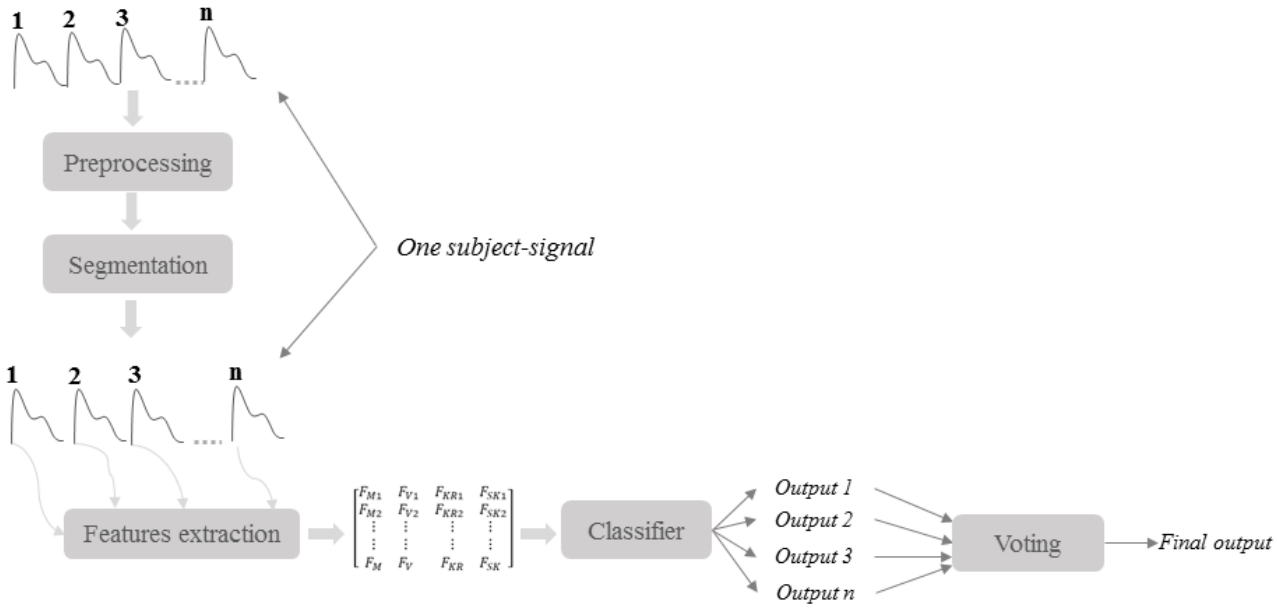

Figure II.7. Features redundancy vote approach

To minimize these errors, we hypothesize that if the testing process is repeated using different feature sets from a particular subject-signal, the overall performance will be enhanced. To achieve this, the testing performance will incorporate the entire subject signal, by combining the feature sets of each segment to produce the final prediction. Specifically, the combination

of outputs will be based on a majority vote of the segment population. This approach aims to leverage the inherent pulsatile dynamics of the cardiovascular system and mitigate the potential impact of outliers by aggregating predictions from multiple feature sets within a subject-signal. The goal is to improve the robustness and reliability of the classification model's performance evaluation.

4. The Overall Classifier Optimizer Workflow

The classification model development will involve a two-pronged optimization approach. The first aspect will focus on optimizing the internal ML hyperparameters, while the second will target the external feature parameters.

Preprocessing and segmentation of the PPG signals will be performed, followed by feature extraction. These features will be derived from morphological, temporal, and TF analysis of the PPG waveforms.

An external optimization step will then be conducted to reduce the dimensionality of the feature space. This will be achieved by applying either the MRMR technique on the temporal and morphological features, or a Cuckoo Search algorithm on the TF-derived parameters.

The optimized feature set will be used as input to the classifier model. The internal hyperparameters of the classifier will be further tuned using a Bayesian optimization algorithm to enhance the model's performance.

Finally, the trained classifier model will undergo an additional external optimization step. The model's performance will be evaluated using the proposed FRV approach.

This multi-layered optimization approach, encompassing both internal hyperparameter tuning and external feature engineering, aims to develop a robust and high-performing classification model for the targeted biomedical application.

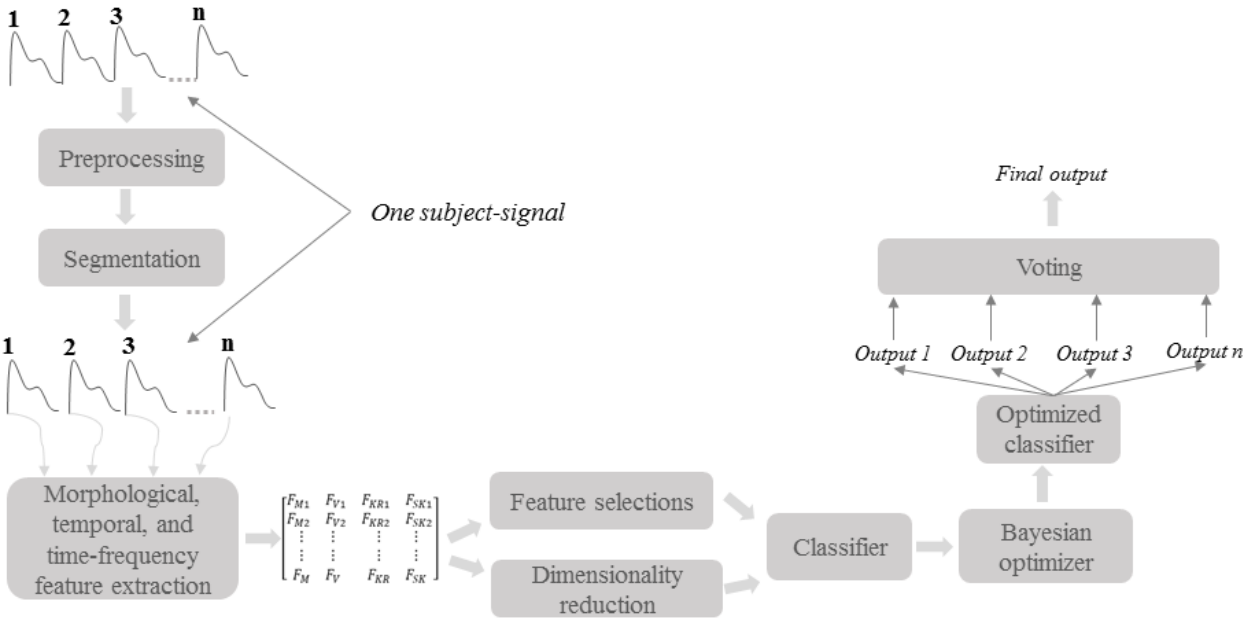

Figure II.8. Multi-objective optimization architecture

Chapter III

Operationalizing an Upgraded Classification Framework

Signal Processing, Feature Engineering, Hyperparameter Optimization, of an Arterial Pressure Risk Prediction

1. Objectives

This Chapter outlines our proposed methodology based on the following steps:

To begin, we carefully select an appropriate dataset that aligns with our approach's requirements, considering factors such as sample size, diversity of AAP and BP values, as well as data quality. Subsequently, we perform a screening on PPG signals for potential artifacts and applying a series of preprocessing techniques on the raw waveform data to eliminate any noise and baseline drifts that may interfere with the classification system.

Next, we segment the ABP and PPG signals into pulses, using a third derivative approach to detect their troughs. We then employ an optimization algorithm to locate the dicrotic notches, which play an essential role in PPG feature extraction and AAPs modeling.

To identify AAPs, we conduct a thorough analysis of their distinguishing characteristics, such as amplitude, shape, and duration, by referring to relevant literature. We subsequently extract a set of features from the preprocessed PPG pulses and assign them to their respective AAP class labels.

Finally, we develop a dataset for BP levels classification. This involves extracting FSST features from 2-secondes PPG segments we than assign them to their respective classes depending on the tasks, such as hypertension or BP ranges.

2. Data Analysis

2.1. Data Base Description

The dataset utilized in the current research originates from the MIMIC-III database, an openly available repository holding anonymized medical information from patients admitted to ICU [182]. MIMIC-III is widely recognized for its substantial size and widespread adoption within the medical research community.

Within the MIMIC-III database, numerous data types are accessible, such as laboratory results, demographic information, clinical registrations, medication details, and biomedical signals. Particularly, the MIMIC-III waveform database encompasses over 3 million hours of signal recordings across 67,830 records [198]. This includes simultaneously captured ABP and PPG signals from thousands of ICU patients, at a sampling frequency of 125 Hz.

2.2. Data Acquisition Methodology

2.2.1. Output Variable Selection

To ensure diversity in BP values, a process was implemented during data collection whereby each acquisition of an ABP record was inspected for SBP and DBP values. This process continued until a wide feasible range of BP values was achieved. Each 1-minute ABP signal was collected with its corresponding 1-minute PPG signal, both containing 7500 data points. To ensure diversity of AAPs and good signal quality, a manual selection process was conducted for ABP and PPG records from the MIMIC-III database. Records were continuously collected meanwhile each ABP was visually inspected for possible AAP patterns, including bisferiens, anacrotic, dicrotic, deep, bounding, and tardus pulses (**Figure III.1**).

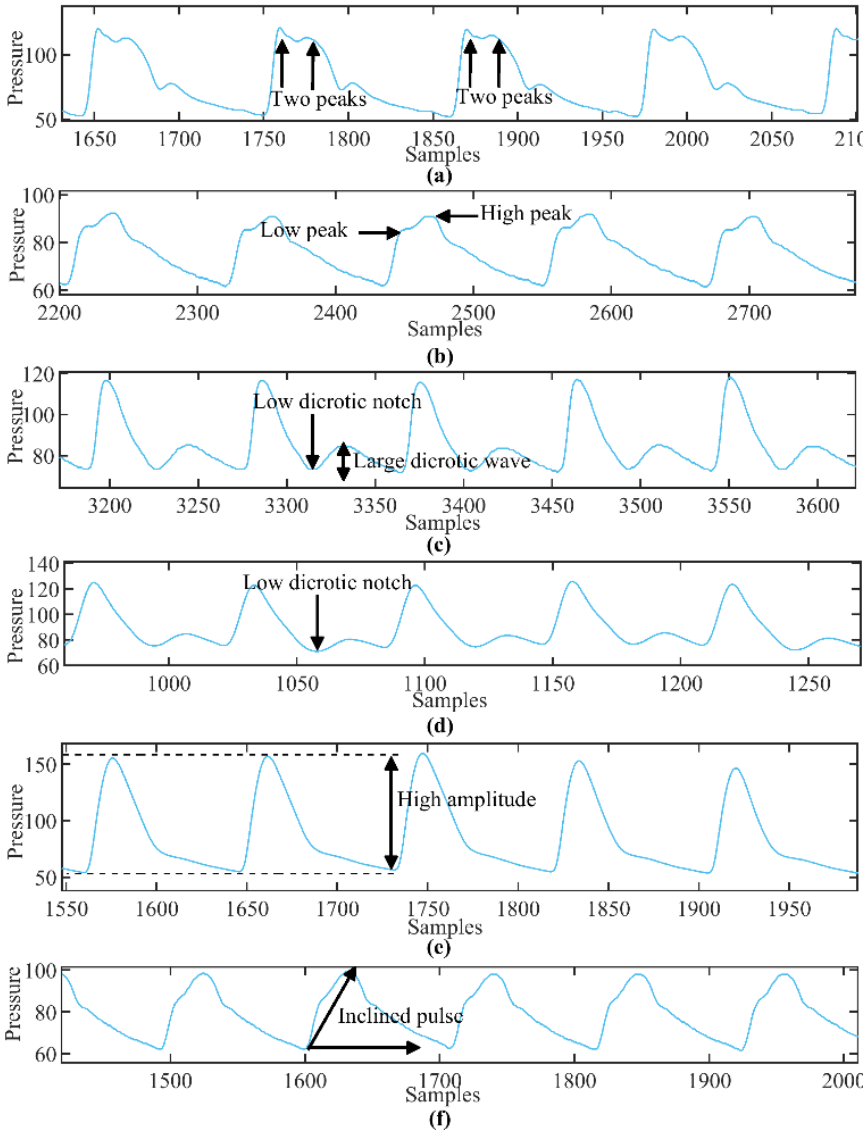

Figure III.1. Abnormal pulse patterns in arterial pressure waveforms

Specifically, bisferiens and anacrotic pulses were identified by two systolic peaks, with anacrotic pulses distinguished by a lower first peak (**Figure III.1 (a)**, **(b)**). Dicrotic and deep pulses showed abnormally low dicrotic notches (**Figure III.1 (c)**, **(d)**), with dicrotic pulses having larger dicrotic waves (**Figure III.1 (d)**). Bounding pulses had abnormally high amplitudes (**Figure III.1 (e)**). Tardus pulses appeared inclined to the right due to delayed peak time (**Figure III.1 (f)**). The process continued until a reasonable number of AAP examples was observed.

2.2.2. SSQI-Based PPG Acquisition

PPG signals underwent a signal quality assessment following an SSQI-based protocol [199]. Some PPG records were excluded due to poor signal quality and motion artifact interference. Orphanidou's research [200] revealed that skewness is linked to distorted PPG signals and has a particular correlation with the quality of PPG signals. Similarly, Liang et al. [201] determined that skewness is the most suitable approach for evaluating the SQI in PPG signals.

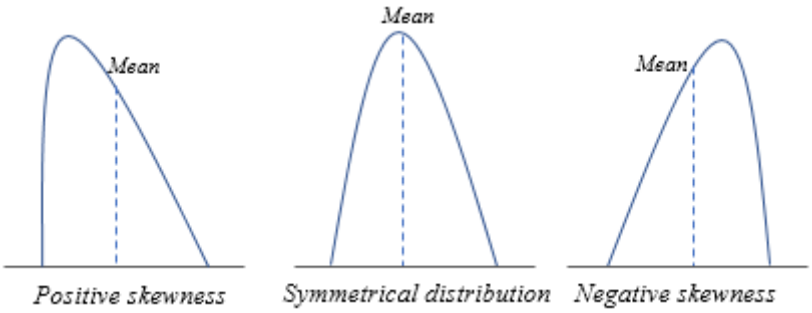

(a) Skewness waveform response

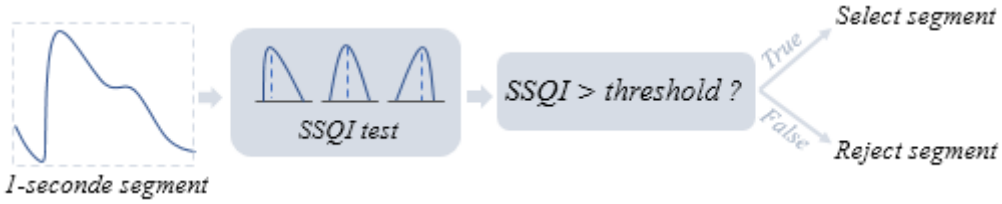

(b) Screening process

Figure III.2. Skewness analysis

Skewness is a measure that reflects the level of asymmetry exhibited by a distribution in relation to its mean value [202], as depicted in **Figure III.2 (a)**. When the skewness is positive, it signifies a distribution with an asymmetric tail biased towards the positive side of the mean. When the skewness is negative, it signifies a distribution with an asymmetric tail biased towards the negative side of the mean [203]. The PPG pulse distribution has an asymmetric tail that extends in the direction of larger, more positive values. Thus, positive skewness suggests good

SQI whereas negative skewness indicates low SQI. The PPG screening process is further illustrated in **Figure III.2 (b)**. In accordance with study in [201], we use 1-second PPG segment to assess its quality. The signal is selected if its SQI exceeds a threshold of 0.90.

2.2.3. Filtering

The signals obtained from the MIMIC III database are often impacted by undesirable effects, such as high-frequency noise and baseline drift in PPG signals, as well as noisy fluctuations in ABP signals. To address these effects, we employ two filtering techniques. Firstly, we apply a fourth-order Butterworth filter with a bandpass of 0.5 Hz to 8 Hz to eliminate baseline drift and high-frequency noise in PPG signals, respectively [118]. Secondly, we used a moving average filter to remove noisy fluctuations from ABP signals.

3. Biomedical signal Preprocessing

3.1. Normalization

The z-score normalization approach is utilized to standardize the signal and maintain a consistent scale. It involves adjusting the signal by first subtracting the mean (μ) to center it, and then scaling it using the standard deviation (δ). Presented herein are the vector forms representing the original signal retrieved from the dataset, as described in **Eq. (1)**, and the normalized signal, as expressed in **Eq. (2)**.

$$X = \{x_1, x_2, x_n, \dots \dots \ x_N\} \tag{1}$$

$$X_{norm} = \{\frac{x_1 - \mu}{\delta}, \frac{x_2 - \mu}{\delta}, \frac{x_n - \mu}{\delta}, \dots \dots \ \frac{x_N - \mu}{\delta}\} \tag{2}$$

where x denotes a sampling point in the signal, n is the sample index and N is the total length.

3.2. Pulse Wave Features Detection Algorithms

3.2.1. Peak Detection

To locate the peaks of the signal, a threshold (*TH*) is initially established to isolate the prominent waves from the rest of the normalized signal, as indicated in **Eq. (3)**. This method, known as clipping, is commonly employed by researchers for peak detection [204].

$$TH = \frac{1}{N}\sum_{n=1}^{N}|X_{norm}| \tag{3}$$

Next, we eliminate any part of the signal that falls below the threshold:

$$S = X_{norm} \quad if \quad X_{norm} > TH$$
$$S = TH \quad otherwise \tag{4}$$

where S represent the isolated signal.

Finally, we compare each sample to the threshold to identify the peak values. To prevent the identification of consecutive peaks within the same pulse, we set a minimum distance of 40 samples between any two identified peaks. By enforcing this condition, we can ensure that each peak corresponds to a distinct pulse within the signal.

3.2.2. Trough Localization approach

To extract pulses from the records we performed a segmentation process based on the signal's third derivative. Our analysis revealed that every trough in the signal is closely associated with a local maximum in the signal's third derivative (**Figure III.3 (a)**), an observation that we term the Local Maximum Third Derivative (LMTD). Interestingly, these LMTDs remain detectable even in records where the troughs are not visible (**Figure III.3 (b)**), indicating their potential use in approximating suppressed troughs.

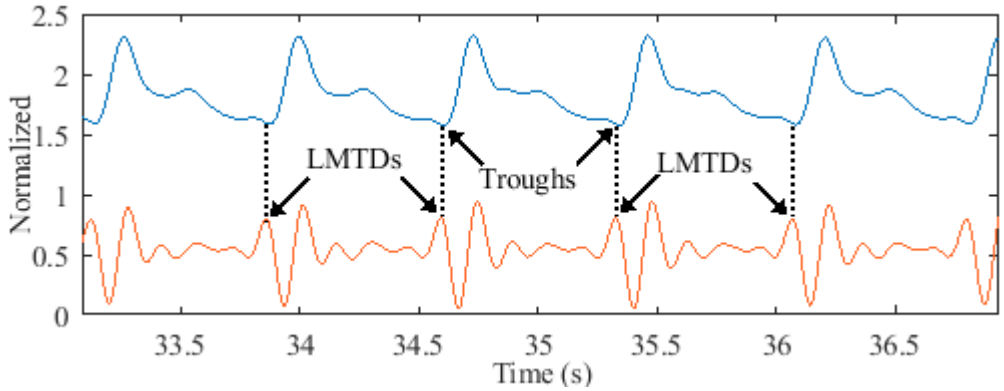

(a) Detectable troughs from an ABP record

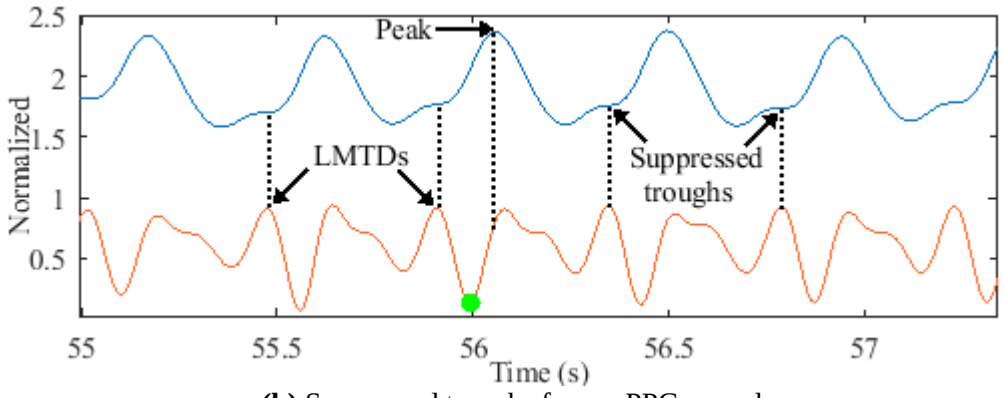

(b) Suppressed troughs from a PPG record

Figure III.3. LMTD locations

As illustrated in **Figure III.3**, to detect an LMTD we must first identify the last local minimum that precedes the signal's peak (in green). As a result, three key features must be extracted in order to detect the trough: the peak, the last minimum preceding it, and the LMTD. The subsequent steps outline the segmentation process in detail.

To detect the LMTDs, we initially divide the third derivative of the signal into discrete windows (**Eq. (5)**). The boundaries of each discrete window are set to correspond with the peak values of the original signal.

$$X'''_{norm} = \{d_1, d_2, d_n, \dots d_l, \dots \dots \ d_L\} \tag{5}$$

where X'''_{norm} represent the normalized signal's third derivative, with each sample value denoted as d, the window's limit as l, and the last limit as L .

Subsequently, we identify the local minima that precede the limits of the windows. We then update these limits by shifting them backward until they align with the local minima values. This process results in a revised set of limits, as denoted in **Eq. (6)**.

$$X'''_{norm} = \{d_1, d_2, d_n, \dots d_{lu}, \dots \dots \ d_{Lu}\} \tag{6}$$

where, the updated limit is designated as lu, and the final updated limit as Lu.

Finally, we identify the LMTDs as the local maxima preceding the updated limits. The process for detecting LMTDs is further illustrated in **Figure III.4**.

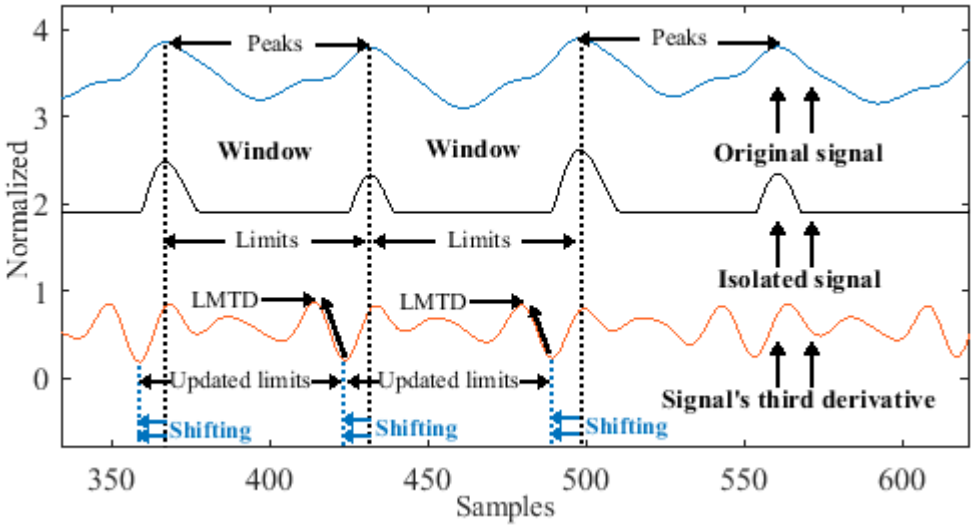

Figure III.4 LMTD detection

To approximate the index values of the suppressed troughs, we examined the marginal distance between LMTDs and detectable troughs. Analysis of the signals revealed mean

distances (MDs) and standard deviation distances (STDs) of 2.6±1.1 and 1.22±0.95 for ABP and PPG signals, respectively. As a result, the formula for approximating the suppressed troughs is defined as:

$$tr_{sup} = LMTD_{idx} + MD \quad (7)$$

where tr_{sup} denotes a suppressed trough, $LMTD_{idx}$ represent the LMTD index and MD represent the mean distances.

3.2.3. Dicrotic Notch Optimization

A dicrotic notch is typically identified by locating the local minimum at the end of the systolic phase. However, in the case of a suppressed dicrotic notch, a slight inflection point replaces the local minimum, making it difficult to detect using conventional methods. Therefore, we present a novel approach for detecting suppressed dicrotic notches using a multi-objective optimization technique.

We introduce a tool that measures the angles of inflection points using two intersected lines, as shown in **Figure III.5**. Conventionally, an angle of two intersected lines is calculated as follows:

$$\theta = tan^{-1}(\frac{a_2 - a_1}{1 + a_1 a_2}) \quad (8)$$

where a_1 and a_2 are the slopes of the first and second line, respectively.

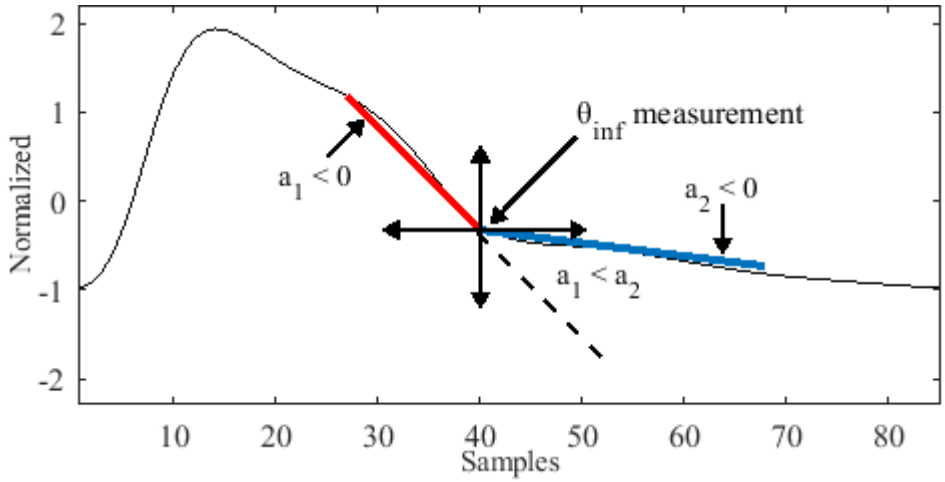

Figure III.5. Measurement technique

However, this method is only valid for equally calibrated signal axes. Instead, we propose estimating the inflection point values utilizing a customized formula. This involves considering the deviation's degree of one line relative to the other, as illustrated in **Figure III.5**.

Additionally, we impose constraints on the slopes of the intersected lines, to ensure the exclusive measurement of the inflection points, as denoted in **Eq. (9)**.

$$\theta_{inf} = \frac{a_2 - a_1}{a_1}, \text{ such that } \begin{cases} a_1, a_2 < 0 \\ a_1 < a_2 \end{cases} \quad (9)$$

where θ_{inf} represent the degree of deviation of the second line compared to the first line, while inf is the inflection point index.

The search process involves obtaining a set of θ_{inf} measurements within a predetermined search space, which is delineated as a segment of the pulse wave extending between the peak and the trough. The pulse wave can be represented as a sequence of values, denoted as:

$$PW = \{x_{tr}, x_{tr+1}, x_{tr+n}, \dots x_{pe}, \dots x_{tr+k}\} \quad (10)$$

where tr and pe respectively represent the pulse's trough and peak indexes, while k indicates the pulse's length.

The search space is then identified as a subset of PW, denoted as:

$$SP = \{x_{\alpha_1}, \dots \dots \ x_{\alpha_2}\} \quad (11)$$

where α_1 and α_2 represent the indexes that mark the boundaries of the search space and are given by $\alpha_1 \approx pe + 0.15k$ and $\alpha_2 \approx pe + 0.55k$.

The θ_{inf} measurements are taken by sliding the intersected lines along all the search space by respecting the established constrained, as illustrated in **Figure III.6**.

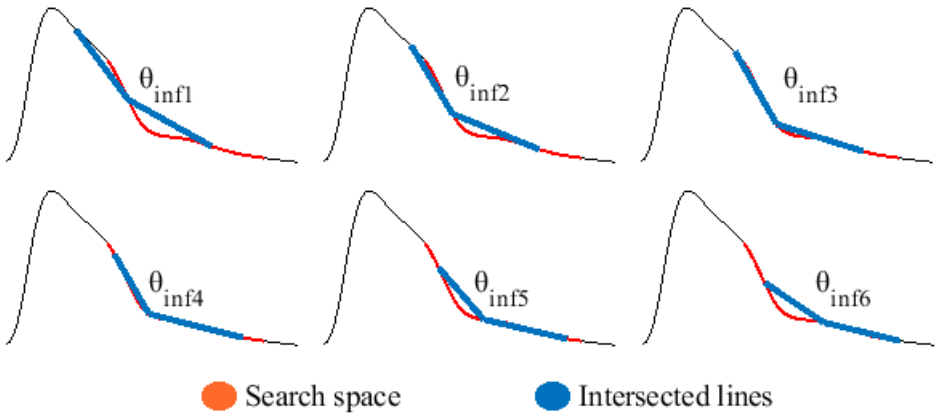

Figure III.6. Random θ_{inf} measurements in the search space

A suppressed dicrotic notch is indicative of an inflection point at the minimum θ_{inf} measurement in the search space, denoted as θ_{min}. However, a single search to obtain θ_{min}

may yield inaccurate measurements, leading to false positive results. As a result, we implement a search process involving multiple iterations (i) to identify the optimal solution (inf_{opt}). Within each iteration, measurements are taken using intersected lines of increasing lengths, resulting in varying slopes. In a given iteration, the slope of each line is defined as:

$$a_{i,j} = \frac{f(c_{end}) - f(c_{in})}{c_{end} - c_{in}} \tag{12}$$

$$with \begin{cases} c_{in} = inf - i, \;\; c_{end} = inf \;\; when \;\; j = 1 \\ c_{in} = inf, c_{end} = inf + i \;\; when \;\; j = 2 \end{cases}$$

where c_{in} and c_{end} represent the initial and the last sample index of a line, respectively, while $f(c_{in})$ and $f(c_{end})$ are their expected values. The length of the lines increases by $i = 1$ during each iteration, until it reaches a maximum iteration of $I \approx 0.15k$.

Each of the resulting $\theta_{min}(i)$ correspond to a specific inf in the search space. Therefore, we determine inf_{opt} by considering all the $\theta_{min}(i)$ measurements and their respective $inf(i)$ obtained during the search process. We present the search process results φ_r for a particular pulse r as:

$$\varphi_r = \left\{ \begin{matrix} \theta_{min}(1) \\ \theta_{min}(2) \\ \theta_{min}(i) \\ \vdots \\ \theta_{min}(I) \end{matrix} \middle| \begin{matrix} \text{inf}(1) \\ \text{inf}(2) \\ \text{inf}(i) \\ \vdots \\ \text{inf}(I) \end{matrix} \right\} \tag{13}$$

The θ_{min} measurements that were taken from similar indexes are counted to identify the most present inf in φ_r. As a result, the most prevalent $inf(i)$ in φ_r is identified as inf_{opt}. The search process is further explained in **Figure III.7**.

To evaluate the efficacy of the optimization algorithm, we employ the standard deviation (SD) as a metric to ensure that the dicrotic notches are accurately located. Typically, the distance between a peak and its corresponding dicrotic notch is nearly constant across all pulses in a signal. Thus, the SD captures the variation between the optimal solutions inf_{opt} and the peaks throughout the entire signal X_{norm}. The SD can be defined using the following equation:

$$SD = \frac{\sum_{r=1}^{R}(inf_{opt}(r) - pe(r) - \sigma)^2}{R} \tag{14}$$

where σ represents the mean distance between the peak and the optimal inflection point, while r denotes the index of each pulse and R represents the total number of pulses in the signal.

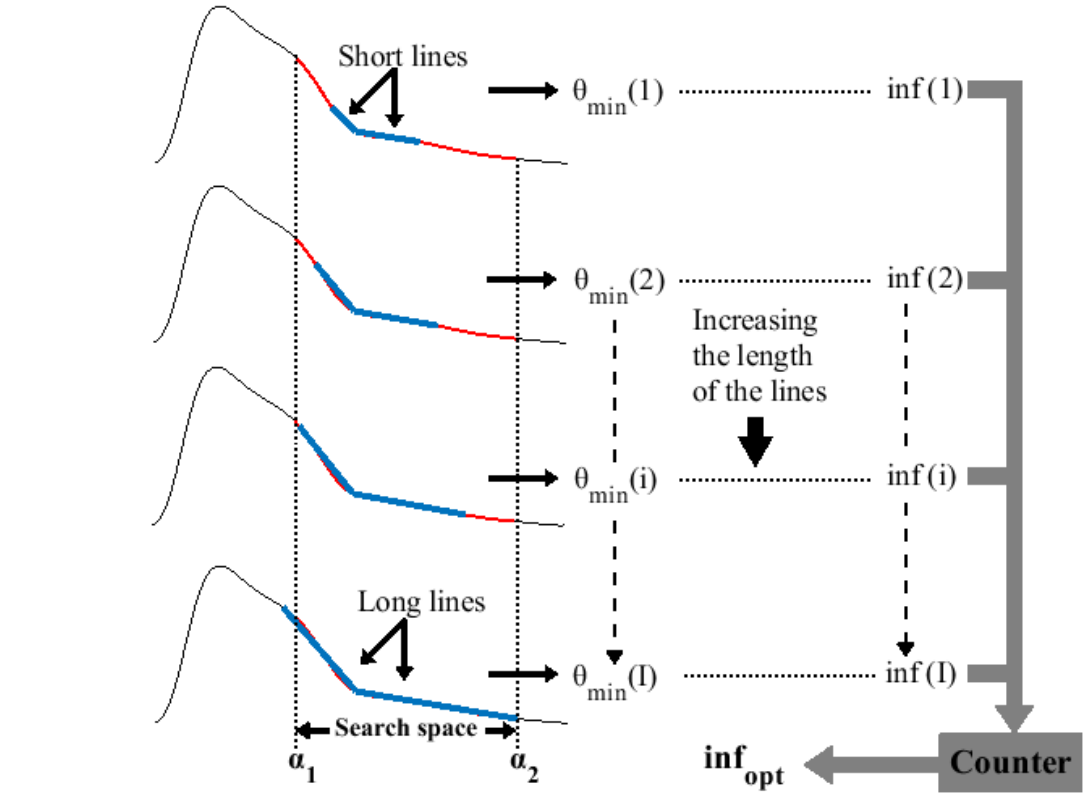

Figure III.7. Search technique

To further minimize the SD index, the search process is regenerated by gradually narrowing the search space (specifically α_2) through three iterations until improved results are obtained, as depicted in **Figure III.8**. If no improvement is observed, we select the search with the lowest SD value as the final result. Nevertheless, our analysis indicates that a marginal improvement of less than 1.38 is considered an instance of over-minimization. To address this, we have set a threshold to control the SD minimization process, requiring the SD index to improve by a value equal to or greater than 1.38.

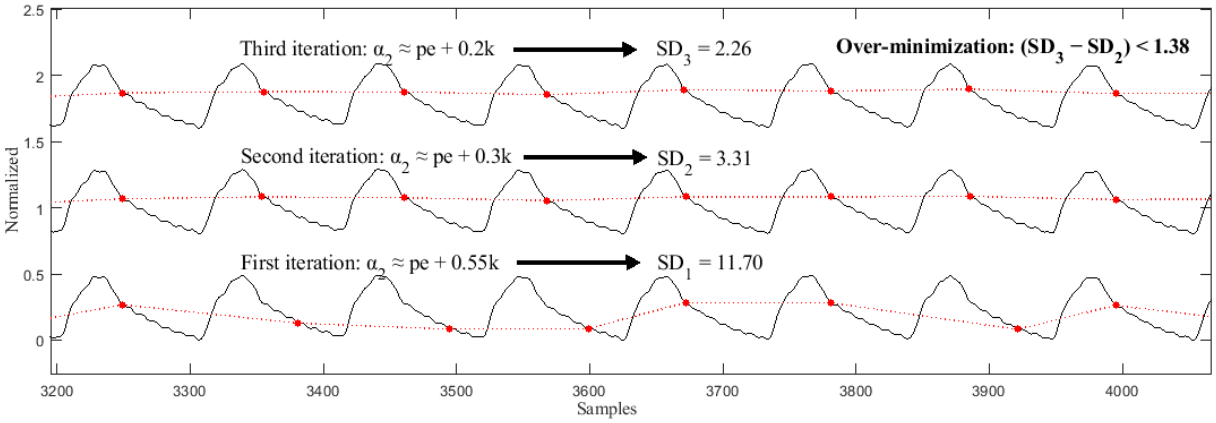

Figure III.8. A segment from an Arterial pressure signal during evaluation process

To evaluate the efficacy of the proposed optimizer, **Figure III.8** presents a segment of a disrupted ABP signal. This particular signal was intentionally selected for its instability and association with various fluctuations, with the aim of testing whether any false positive dicrotic notches are detected.

Overall, our proposed algorithm incorporates three objective functions in an iterative manner. Firstly, we minimized θ_{inf} to obtain the minimum inflection point measurement (θ_{min}). Secondly, we maximized φ_r to identify the optimal inflection point index (inf_{opt}). Finally, we minimized the SD index to improve the overall optimization process.

4. Features Engineering

4.1. Physiologically-Grounded Features

From PPG each pulse, a set of 24 features were extracted for use in AAP classification system. Our analysis starts by selecting six segments from the pulse signal, including the total pulse (**Figure III.9**). Each segment is then processed to derive four distinct features.

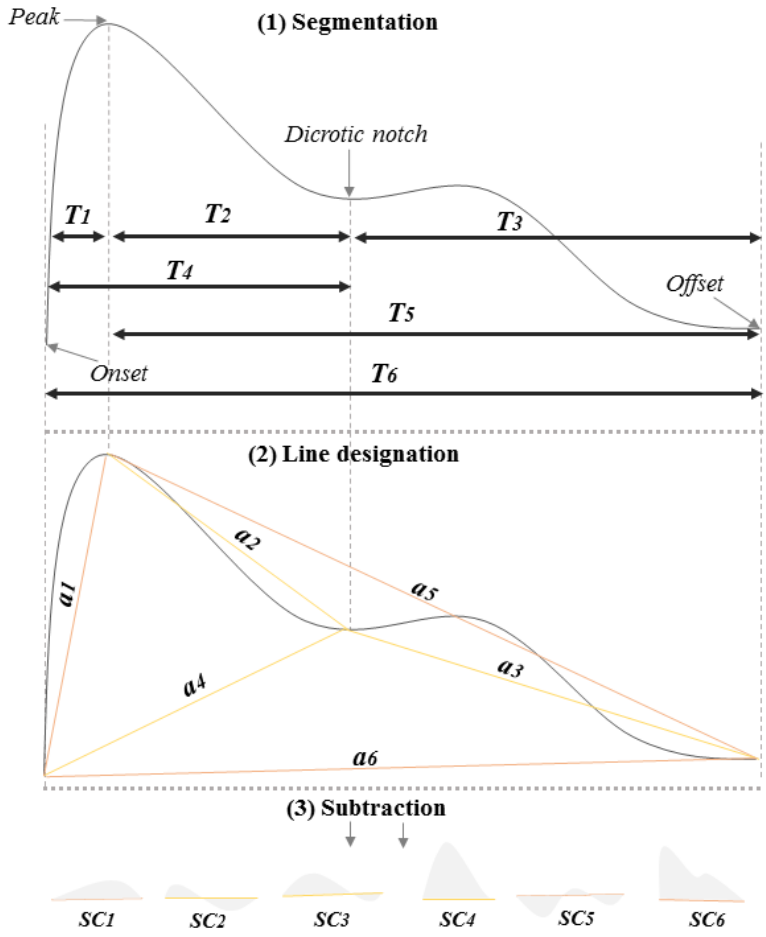

Figure III.9. Morphological feature analysis

The first feature relates to the temporal aspects of the selected phases and is defined as:

$$F_T = \frac{T}{fs} \tag{15}$$

where F_T represents the time feature, T denotes the length of the selected phase, and fs corresponds to the sampling frequency.

Next, we determine the slope (a) features by establishing lines that connect the limits of each curve within the selected segments. The slope is calculated using the following equation:

$$F_a = \frac{Y_{end} - Y_{in}}{T - 1} \tag{16}$$

where F_a represents the slope feature, while Y_{in} and Y_{end} denote the data values marking the beginning and end of a given segment in the PPG signal.

Finally, we explore the SCs obtained by subtracting each curve from its corresponding line. These SCs are represented as a sequence of data points:

$$C_{sub} = \{v_1, v_2, v_m, \dots \dots \ v_M\} \tag{17}$$

where *v* is the expected data value from a given sample index *m*, and *M* is the length of the data points.

We then calculate the mean and kurtosis of the SCs. The mean represents the average value of the SC:

$$F_M = \frac{1}{M} \sum_{m=1}^{M} v_m \tag{18}$$

The kurtosis measures the tailedness of the SC and is defined as:

$$F_{KR} = \frac{\frac{1}{M} \sum_{m=1}^{M} (v_m - F_M)^4}{\left(\frac{1}{M} \sum_{m=1}^{M} (v_m - F_M)^2\right)^2} \tag{19}$$

As a result, we present the input matrix F_{in} as follows:

$$F_{in} = \begin{bmatrix} f_1(1) & f_1(2) & f_1(u) & \dots & f_1(U) \\ f_2(1) & f_2(2) & f_2(u) & \dots & f_2(U) \\ \vdots & \vdots & \vdots & & \vdots \\ f_W(1) & f_W(2) & f_W(u) & \dots & f_W(U) \end{bmatrix} \tag{20}$$

Here, $u \in \{1, 2\dots, 24\}$ and denotes a specific feature in a row matrix, U represent the twenty fourth feature while W is the length of the input dataset.

4.2. Time-Frequency Domain Features

The PPG signals were divided into 2-second windows initiating at the trough of each pulse signal, each comprising 250 samples, as detailed in **Figure III.10**.

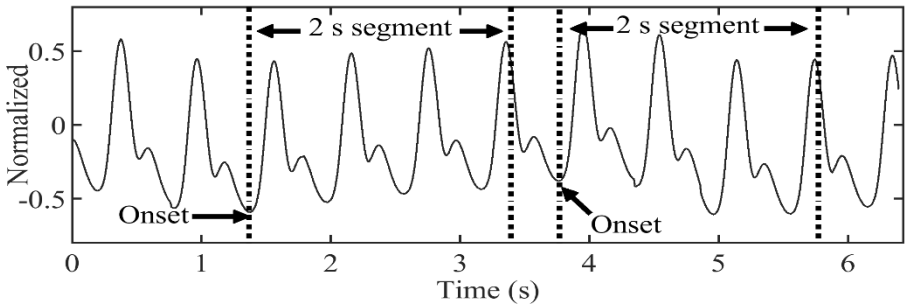

Figure III.10. PPG signal segmentation

The feature extraction process aims to reduce the input dimensions through statistical analysis and metaheuristic optimization. It involves two main steps: representing the PPG signal's time-varying spectrum using the FSST and reducing the dimensionality of the FSST output matrix.

The process begins by computing the STFT of a given 2-second PPG signal. Specifically, the signal is divided into 20 short segments, each windowed using a 20-sample Hamming window. Overlapping windows with 19-sample overlap are used for smooth spectral tracking over time. Within each segment, the fast Fourier transform (FFT) is applied to capture the frequency information. This generates a TF representation, showing how spectral content evolves over time. **Figure III.11** displays the 3D views of TF planes representing signals from each BP level group.

Next, the Fourier coefficients from the STFT are reassigned to new time locations based on instantaneous frequency estimates, creating the FSST (**Figure III.12**). This squeezing process sharpens the PPG signal's time-varying spectrum and provides a more concentrated view in the TF plane compared to the smeared STFT in **Figure III.11**.

The FSST produces a sizable complex-valued matrix, making it infeasible to use as features. Therefore, two different analysis are followed to reduce the features dimensions, including statistical analysis and metaheuristic optimization.

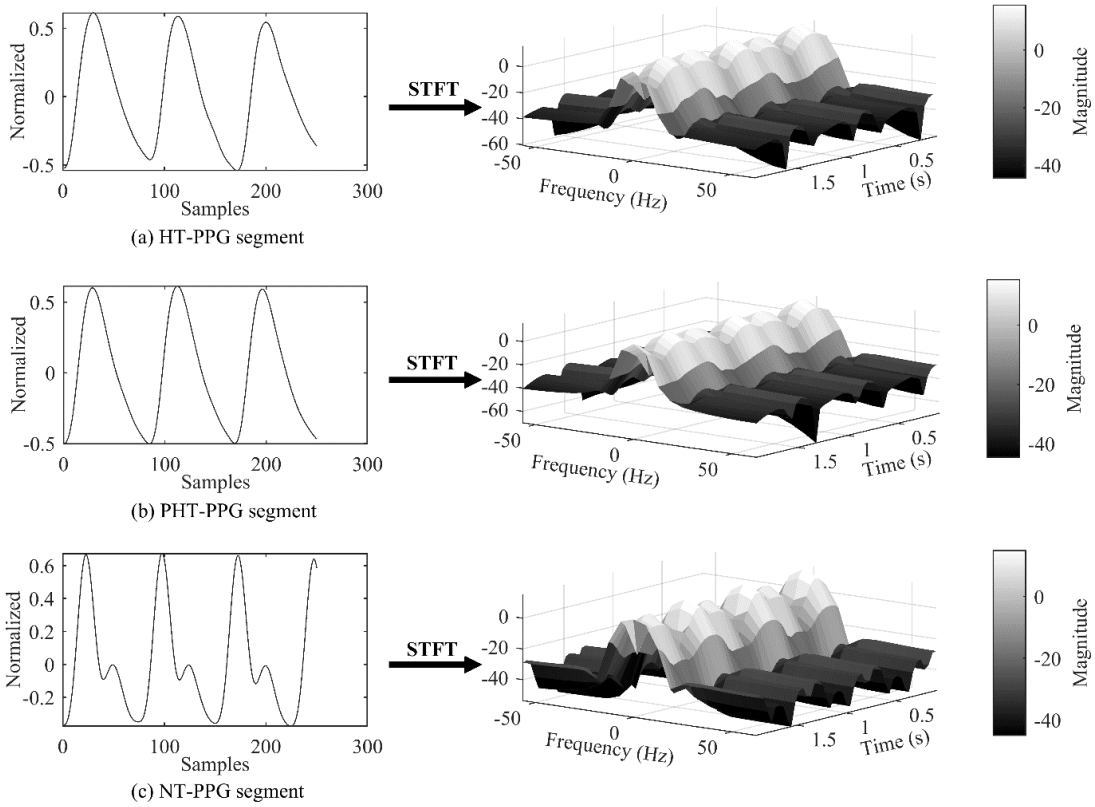

Figure III.11. Short-time Fourier Transform of PPG segments

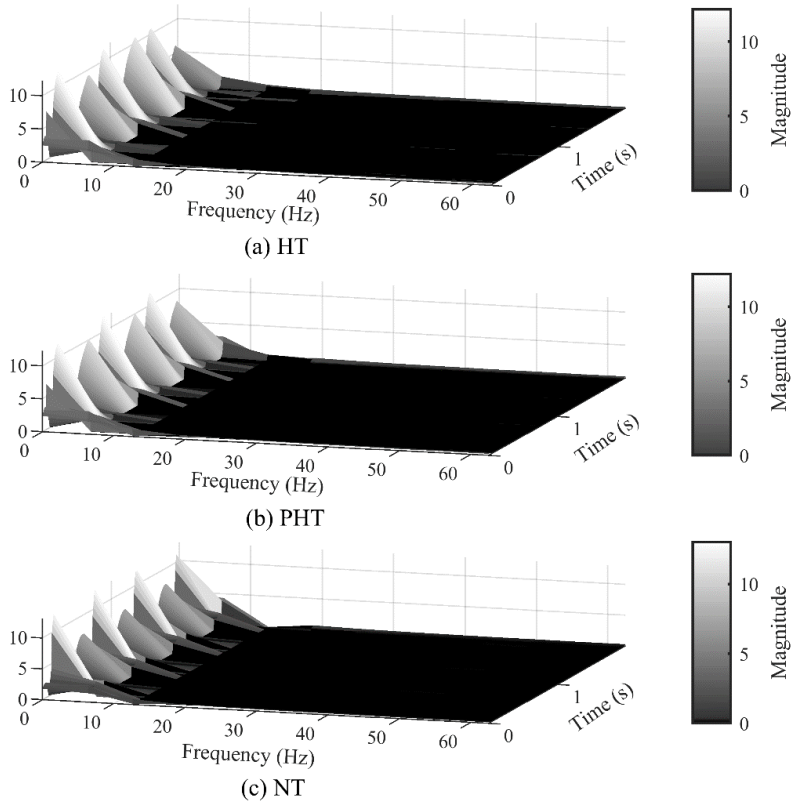

Figure III.12. Fourier Synchrosqueezed Transform of PPG segments

4.2.1. Statistical analysis

To reduce dimensionality of the FSST output matrix, each frequency bin column is processed to derive four statistical features. This compresses the FSST matrix, meanwhile retaining predictive insight regarding the behavior of the reassigned time instances in each frequency bin. Furthermore, three different feature experiments are adopted within this approach, each consisting of a different reference variable to compute the input features, including the magnitude (absolute value), real and imaginary parts of the complex values. Let's consider X_r a sequence of the reassigned coefficients denoted as:

$$X_r = \{x_1, x_2, x_n, \dots \dots \ x_N\} \tag{21}$$

where r is the frequency index, N is the sequence length and x is the expected complex-value from a given sample index *n* and defined as:

$$x_n = a_n + jb_n \tag{22}$$

where a_m is the real part, b_m is the imaginary part and j denotes the imaginary unit. The magnitude of x_m becomes:

$$|x_n| = \sqrt{{a_n}^2 + {b_n}^2} \tag{23}$$

The first feature provides an overall sense of the central tendency of the values in the frequency bin and is defined as the mean, or average:

$$F_M = \frac{1}{N}\sum_{n=1}^{N} C_n^{ex} \tag{24}$$

$$Such\ that \begin{cases} C_n^{ex} = a_n & when\ \ ex = 1 \\ C_n^{ex} = b_n & when\ \ ex = 2 \\ C_n^{ex} = |x_n| & when\ \ ex = 3 \end{cases} \tag{25}$$

The second feature measures how far the values spread out from the mean. It is calculated using the variance equation:

$$F_V = \frac{\sum_{n=1}^{N}(C_n^{ex} - F_M)^2}{N} \tag{26}$$

The third feature examines the asymmetry of the distribution using skewness. Skewness quantifies the extent that values are unevenly distributed to one side versus the other side of the data's mean [202]. The skewness formula can be expressed as:

$$F_{SK} = \sqrt{\frac{\sum_{n=1}^{N}(C_n^{ex} - F_M)^3}{N\sqrt{F_V}}} \tag{27}$$

The fourth feature is derived using the kurtosis, which measures the heaviness of the tails of the values relative to the normal distribution [183] and is defined as:

$$F_{KR} = \frac{\frac{1}{N}\sum_{n=1}^{N}(C_n^{ex} - F_M)^4}{\left(\frac{1}{N}\sum_{n=1}^{N}(C_n^{ex} - F_M)^2\right)^2} \tag{28}$$

4.2.2. Cuckoo search optimization

The implementation steps used to optimize FSST parameters are as follows:

***(1) Objective Function Definition**:* The classification accuracy is defined as the objective function to be maximized:

$$f(\boldsymbol{x}) = Accuracy(\boldsymbol{x}) \tag{29}$$

where $\boldsymbol{x}$ represents a subset of FSST features.

***(2) Initial Population Generation**:* An initial population of n feature subsets are generated, with each subset represented as a binary vector $\boldsymbol{x_i}\epsilon,\{0,1\}^k$ indicating the inclusion (1) or exclusion (0) of features.

***(3) Levy Flight-Based Updates**:* For each feature subset $\boldsymbol{x_i}$, a new subset $\boldsymbol{x_i}'$ is generated using Levy flight:

$$\boldsymbol{x_i} = \boldsymbol{x_i'} + \boldsymbol{\alpha}\,.\,Levy(\lambda) \tag{30}$$

where Levy flights introduce perturbations in the FSST feature subset vector.

***(4) Fitness Evaluation**:* The new feature subsets $\boldsymbol{x_i'}$ are evaluated by training a classifier and computing the classification accuracy:

$$Accuracy(\boldsymbol{x_i'}) = \frac{Number\ of\ correctly\ classified\ samples}{Total\ number\ of\ samples} \tag{31}$$

***(5) Selection and Replacement**:* The fitness of the new subset x_i' is compared with the current subset x_i. The current subset is replaced if the new subset demonstrates better fitness:

$$x_i = \begin{matrix} x_i' \\ x_i \end{matrix} \quad \begin{matrix} if\ f(x_i') > f(x_i) \\ otherwise \end{matrix} \tag{32}$$

***(6) Abandonment of Poor Solutions**:* A fraction p_a of the worst-performing subsets is abandoned, and new subsets are generated to replace them.

$$x_i' = x_i + \gamma.(x_i - x_j) \tag{33}$$

where γ is a random number drawn from a uniform distribution and x_j is a randomly selected nest.

***(7) Iterative Process**:* The above steps are iteratively repeated until the classification accuracy converges.

5. Abnormal Arterial Pulse Pattern Modeling

5.1. Bisferiens Model

The bisferiens pulse, derived from the Latin words "bis" (twice) and "ferire" (to beat), is characterized by both a prominent tidal and percussion waves [205]. These waves can be of equal height or one higher than the other. For example, in cases of AR or combined AR and AS, the tidal wave may be taller or approximately equal to the percussion wave, with a short decline in mid-systole [27]. In HOCM, the bisferiens pulse shows a higher percussion wave compared to the tidal wave and a deeper mid-systolic decline in amplitude [28]. In this study, both bisferiens patterns are categorized under the same class, identified by the presence of two peaks during systole (**Figure III.13**).

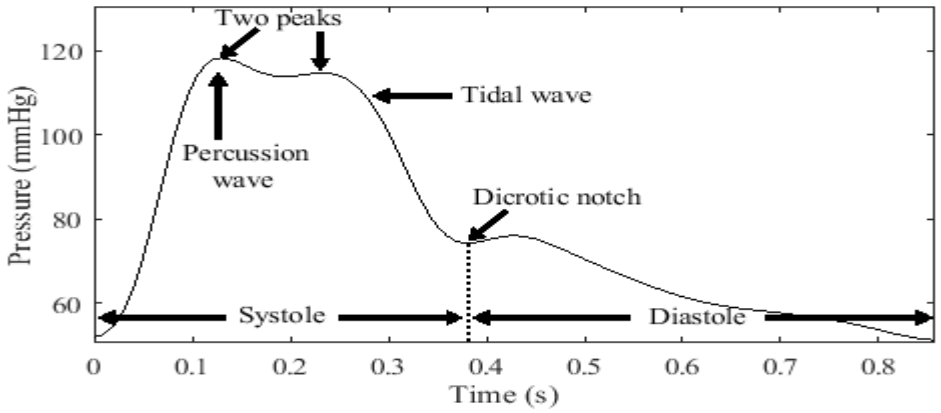

Figure III.13. Bisferiens model

5.2. Anacrotic Model

The typical pulse in AS is referred to as anacrotic, derived from the term "anadicrotic," meaning twice beating on the upstroke [29]. It indicates the presence of two waves during systole. However, this statement creates confusion regarding whether the first wave represents the percussion wave of the bisferiens pulse or the anacrotic wave of the anacrotic pulse [206]. This confusion arises when the first wave has a lower peak compared to the second wave, as illustrated in **Figure III.14**.

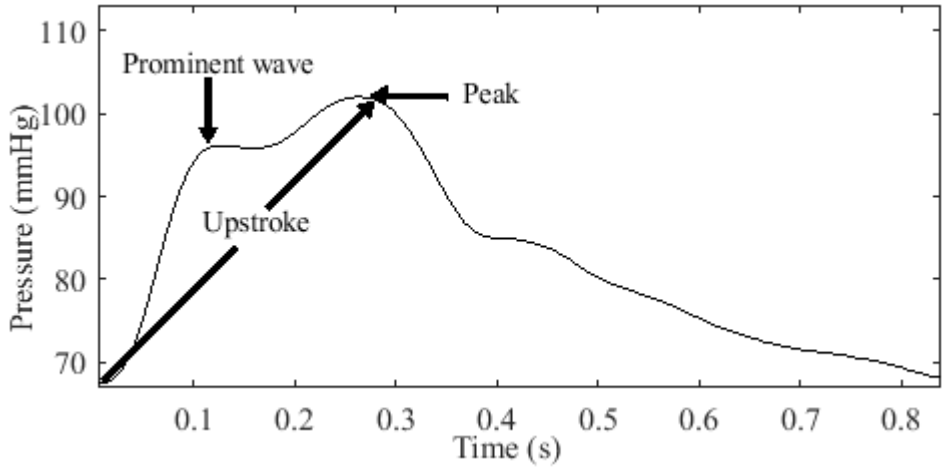

Figure III.14. Anacrotic model

Fleming. [207] described the peaks in the bisferiens pulse as twin peaks. This is visually evident due to their brisk appearance in time [208]. In contrast, anacrotic pulses lack this suddenness. Instead, the upstroke seems interrupted by a notch, resulting in a small first wave, followed by a longer duration to reach the peak of the second wave. This explains Fleming's description of the second wave as being taller and broader than the first wave [207]. Thus, the shape and depth of the dip between the two peaks help differentiate between anacrotic and bisferiens pulses, as they depend on the magnitude of the two waves [209].

Temporal analysis: *Considering the temporal aspect, our analysis demonstrates that the two waves appear briskly when the PPT is shorter than the OPT (**Figure III.15 (a)**). Conversely, the tidal wave appears larger when the PPT is longer than the OPT (**Figure III.15 (b)**). Hence, it is reasonable to assume that the anacrotic pulse has a longer PPT than the OPT.*

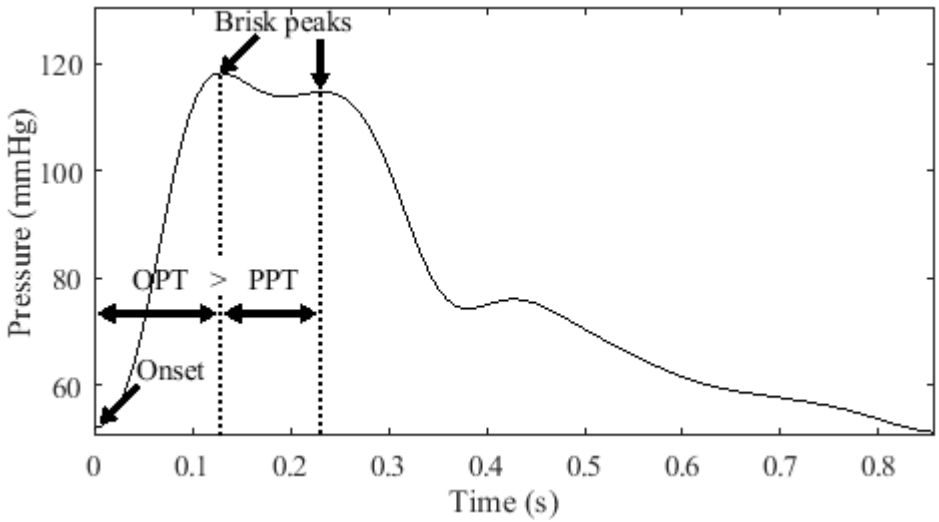

(a) Brisk peaks in a bisferiens pulse

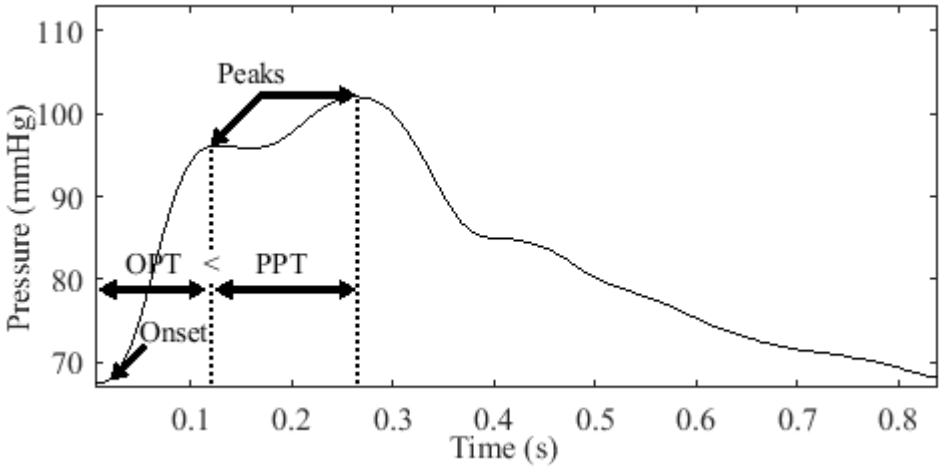

(b) Broad tidal wave in anacrotic pulse

Figure III.15. Bisferiens and anacrotic models' comparison

Contour analysis: *We define anacrotic pulses associated with a non-prominent anacrotic wave based on two conditions:*

Firstly, we set a line connecting the onset and peak of the pulse, and then we subtract the upstroke curve from this line. This subtraction generates a SC comprising positive and negative samples. The positive samples represent the curve above the line, while the negative samples represent the curve below the line. Consequently, for an anacrotic wave to be present, the AUPC must be greater than the AUNC.

Secondly, we locate the peak value of the SC, which represents the positive inflection point of the wave. We then set another line connecting the inflection point and the pulse peak. The trough in the secondary SC represents the notch of the anacrotic pulse. ***Figure III.16*** *provides further illustration of the detection process.*

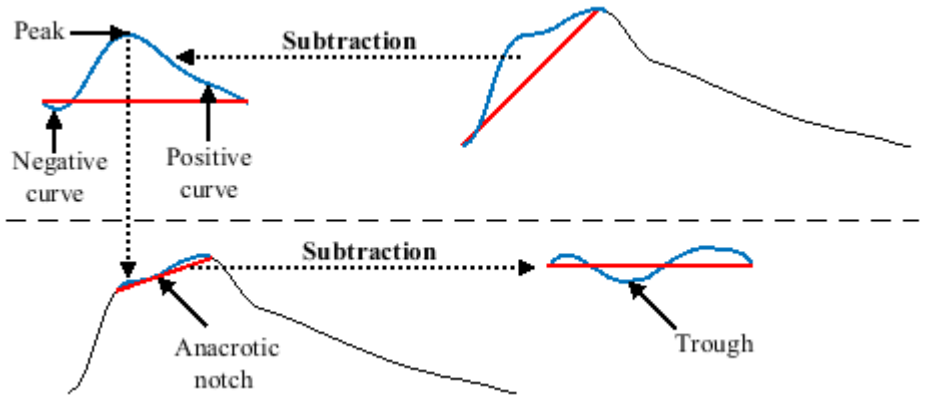

Figure III.16. Anacrotic pulse contour analysis

5.3. Dicrotic Model

In contrast to bisferiens and anacrotic pulses, a dicrotic pulse is characterized by the presence of two waves, with the first wave occurring during systole and the second wave during diastole.

Contour analysis: *Meadows et al. [65] defined a fully dicrotic pulse as having a DWA greater than 30% of the PP and a DNL less than 10% of the PP. They also established borderline criteria, which includes a DWA greater than 20% of the PP and a DNL less than 20% of PP. However, it's important to note that a low level of the dicrotic notch does not necessarily indicate a large dicrotic wave. Therefore, pulses with low DNL and high DWA are labeled as dicrotic pulses, while pulses with only low DNLs are labeled as deep pulses. In this study, we employ the borderline criteria to model dicrotic and deep pulses, as illustrated in* ***Figure III.17.***

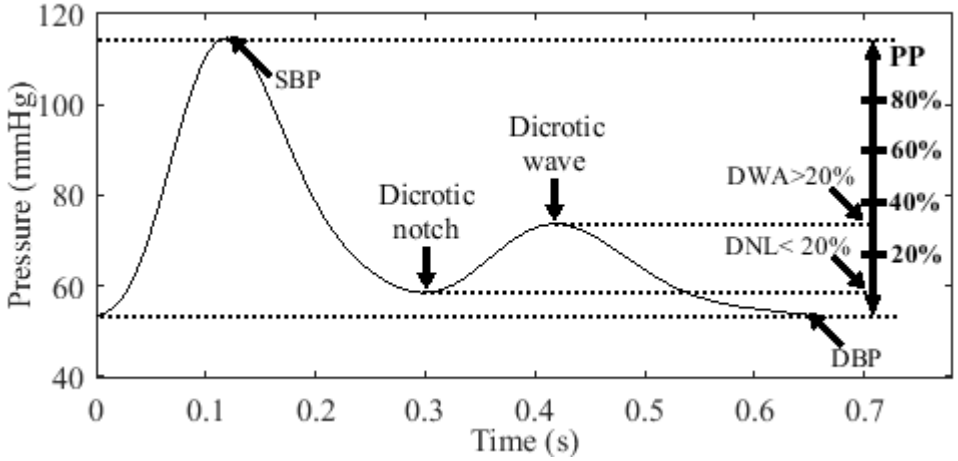

Figure III.17. Borderline dicrotic pulse criteria

5.4. High Amplitude Models

The amplitude of a pulse can be understood in terms of volume, pressure, or peak systolic velocities when analyzing doppler waveforms [210, 211]. The specific interpretation depends on the type of pulse and the nature of the study. In our study, we focus on arterial pressure pulses, and thus we refer to the amplitude as PP. The normal PP range is considered to be between 40 and 60 mmHg [212, 213]. Therefore, a HAP is defined as having a PP greater than 60 mmHg. Our analysis includes three types of HAP models: BDP, shallow HAP, and WHP.

The BDP is characterized by a rapid rise in pressure, resulting in a steep upstroke as illustrated in **Figure III.18**. To our knowledge, there are no defined cutoff values or guidelines to determine the normal range of UT. However, Wood. [29] proposed that an UT of less than 0.16 s can be considered normal. In line with Wood's criterion, Boiteau et al. [214] reported a normal radial UT ranging between 0.11 s and 0.16 s. Thus, we define a BDP as having a PP greater than 60 mmHg and an UT less than or equal to 0.16 s.

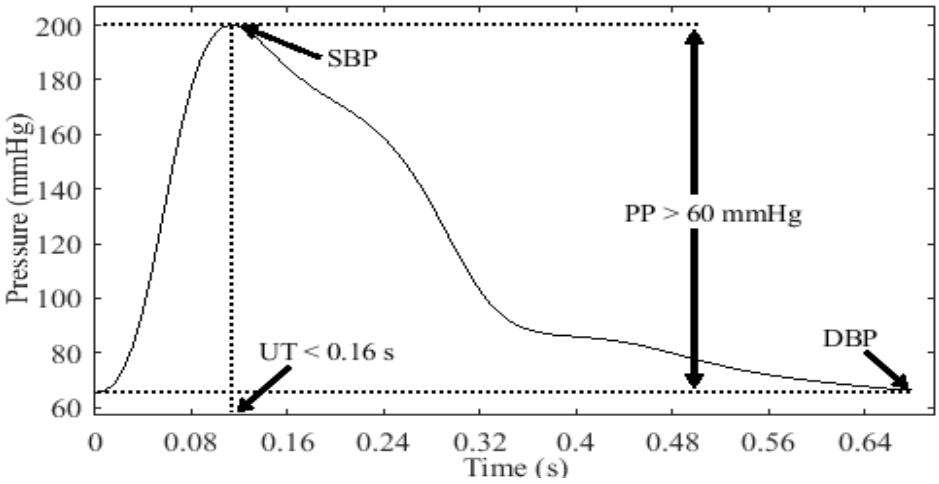

Figure III.18. Bounding model

We refer to the second type of HAP as shallow due to its inclined upstroke, late systolic peak, and occasional early hump. This pulse pattern is commonly observed in conditions associated with arterial stiffness [215]. Similarly, in the case of bradycardia (slow heart rate), the pulse displays a prolonged time in reaching the peak, leading to a broad peak, as illustrated in **Figure III.19**. In contrast to the BDP, a pulse is considered shallow when its UT exceeds 0.16 s.

The BDP can be observed in various physiological and pathological states [28]. Particularly, a unique bounding quality often occurs in moderate to severe AR states known as a WHP, which is mostly marked in peripheral arteries [216]. As revealed long ago, the main

characteristics that distinguish WHP from other HAPs are its sudden upstroke, narrow and wide percussion wave, and preferably flattened tidal and dicrotic waves [217]. In response to these signs, we propose three interpretation criteria to identify a WHP:

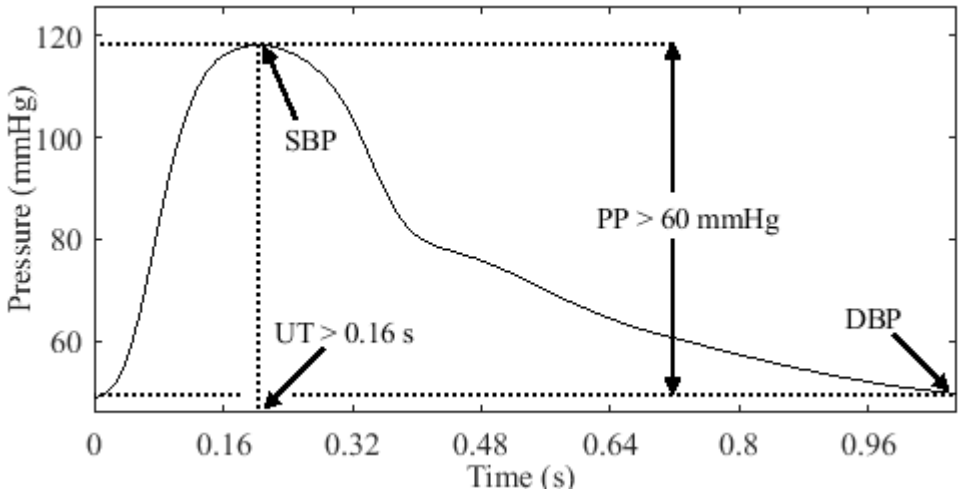

Figure III.19. A high amplitude model with slow upstroke time

Contour analysis: *In accordance with the aforementioned signs, most researchers define a WHP by a steep upstroke, sharp or narrow percussion wave, wide pulse pressure, collapsing, and a sharp downstroke [68,209,216,218]. Therefore, sharpness is an important feature in defining the WHP. Estimating the degree of sharpness in the pulse has been suggested in the literature [219]. However, assessing the sharpness of the WHP requires considering the entire systolic wave, which includes a sharp systolic upstroke and downstroke. To achieve this, we establish two lines: the first line extends from the onset to the peak (upstroke), while the second line extends from the peak to the dicrotic notch (downstroke). The proximity of the wave to these lines indicates its sharpness. Thus, a pulse is considered sharp if the AUNC is greater than the AUPC for both the systolic upstroke and downstroke, as illustrated in* ***Figure III.20****. Similarly, we define a flat diastolic portion if its corresponding AUNC is greater than or equal to its AUPC.*

Amplitude analysis: *McGee. [218] stated in his book that a PP equal to or greater than 80 mmHg and a DBP equal to or less than 50 mmHg increase the probability of moderate to severe AR. These benchmarks were established based on studies investigating the correlation between the severity of AR and PP [220] as well as DBP [221]. Although the WHP is primarily a systolic phenomenon that is not directly defined by low DBP [68], setting this condition enhances the likelihood of its manifestation. This has been confirmed by elevating*

the arm of patients diagnosed with AR, resulting in a decrease in their DBP and a more pronounced water hammer quality [216-218, 222].

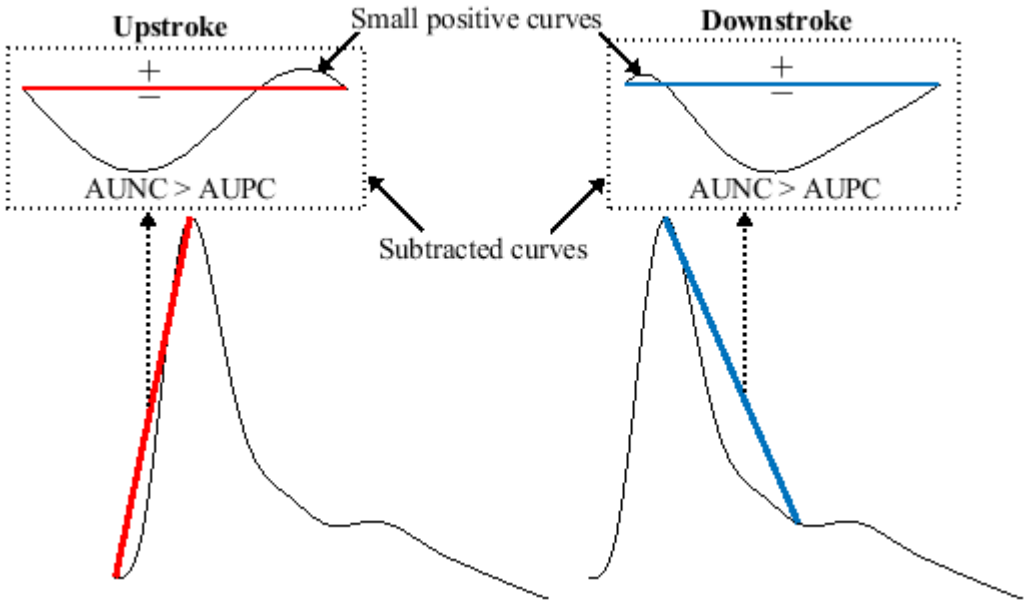

Figure III.20. Sharpness analysis in a water hammer model

Temporal analysis: *Boiteau et al. [214] emphasized that the UT in normal individuals is shortened and does not significantly differ from that observed in AR cases. However, upon further examination of the UT and ST measurements in their study, we observed that some AR subjects had UT values below the normal range reported in their study (0.11 s to 0.16 s). Interestingly, all AR subjects with UT values below 0.11 s had UTs that were less than one third of the ST (UT/ST < 34%), while the majority of the remaining subjects had UTs that were less than half of the ST [214]. Based on this observation, it is reasonable to assume that a short UT, particularly one that is less than one third of the ST, may be indicative of the suddenness in the upstroke of the WHP. Furthermore, the ST is another important feature in identifying a WHP, as it is typically prolonged in AR conditions, ranging between 0.28 s and 0.4 s [214].*

5.5. Tardus Model

Pulsus tardus, a pulse classification denoting a delayed peak, is the term used to describe a slow-rising pulse, and this condition may be further specified as pulsus parvus et tardus when it is accompanied by a diminished amplitude (**Figure III.21**). Pulsus tardus is a finding associated with AS disease, and its inclined upstroke o may be either smooth or interrupted by a notch, as previously described in the anacrotic pulse pattern [61]

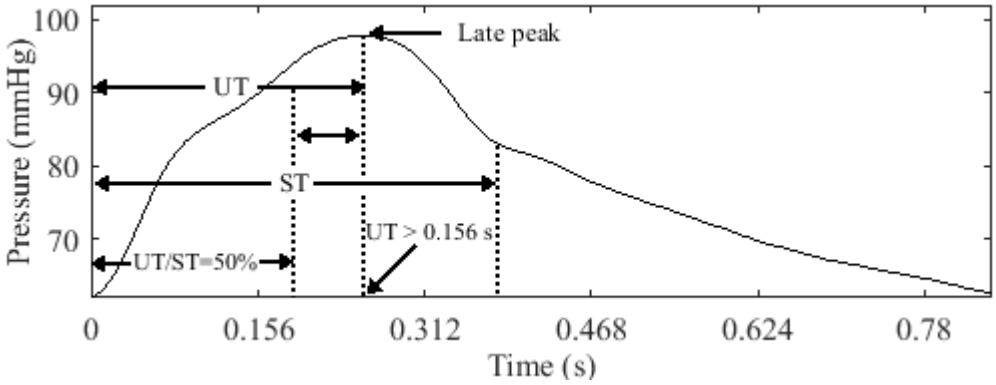

Figure III.21. Tardus model characteristic features

Temporal analysis: *We define pulsus tardus as having an UT greater than 0.156 s, based on a study conducted by Yoshioka et al. [223], in which the authors concluded that an UT exceeding 0.156 s indicates severe AS. In certain cases, pulsus tardus can be mistaken for a shallow HAP, as it can be associated with a high PP in the radial artery due to arterial stiffness [223]. Therefore, we define the pulsus tardus model as having an UT longer than the remaining ST, with an UT/ST ratio greater than 50%, as illustrated in* ***Figure III.21****.*

This definition is supported by the observation that the systolic peak in pulsus tardus often occurs near the second sound of the heart, which represents the closure of the aortic valve at the end of the systolic phase [28].

Amplitude analysis: *The term "parvus" is used to describe a pulse with low volume [224] or a narrow PP [225]. It can also refer to low peak systolic velocities [211]. In the context of pulse pressure, researchers investigated PP measurements in AS states to determine whether pulsus parvus is indicative of severe AS [223]. Thus, a narrow pulse pressure is one of the defining features of pulsus parvus. Accordingly, we define a narrow PP as being less than 40 mmHg [212, 213]. Therefore, pulsus parvus et tardus shares the same characteristics as pulsus tardus, except for the presence of a narrow PP.*

6. Experimental Dataset Configurations

6.1. Class Label Assignment

6.1.1. Abnormal Arterial Pulse Pattern Class Configuration

Table III.1 and **Table III.2** overview of the parameters utilized to model AAPs. **Table III.1** displays the contour configurations, whereas **Table III.2** displays the amplitude and time settings.

Table III.1. Pulse contour parameters used in AAP modeling process

Model	*DNL (%)*	*DWA (%)*	*USC*	*DSC*	*P wave*	*T wave*	*D wave*
Normal	*≥ 20*	*> 20*	*NS*	*NS*	*Prominent*	*Non-prominent*	*Prominent*
Bisferiens	*NS*	*NS*	*NS*	*NS*	*Prominent*	*Prominent*	*NS*
Anacrotic	*NS*	*NS*	*AUPC > AUNC*	*NS*	*Either*	*Prominent*	*NS*
Dicrotic	*< 20*	*> 20*	*NS*	*NS*	*Prominent*	*None*	*Prominent*
Deep	*< 20*	*≤ 20*	*NS*	*NS*	*Prominent*	*None*	*NS*
Water hammer	*NS*	*NS*	*AUPC < AUNC*	*AUPC < AUNC*	*Prominent*	*Non-prominent*	*Non-prominent*

Notes: 1. NS: Not specified. 2. P: Percussion. 3. T: Tidal. 4. D: Dicrotic. 5. USC: Upstroke subtracted curve. 6. DSC: Downstroke subtracted curve.

Table III.2. Time and amplitude parameters used in AAP modeling process

Model	*UT (s)*	*ST (s)*	*UT/ST (%)*	*PP (mmHg)*	*DBP (mmHg)*
Normal	*≤ 0.16*	*≥ 0.28*	*< 50*	*≤ 60*	*NS*
Bounding	*≤ 0.16*	*≥ 0.28*	*≤ 50*	*> 60*	*NS*
Shallow ↑	*> 0.16*	*NS*	*≤ 50*	*> 60*	*NS*
Water hammer	*≤ 0.11*	*≥ 0.28*	*< 34*	*≥ 80*	*≤ 50*
Shallow	*> 0.16*	*NS*	*≤ 50*	*≤ 60*	*NS*
Tardus	*> 0.156*	*≥ 0.28*	*> 50*	*≥ 40*	*NS*
Parvus et tardus	*> 0.156*	*≥ 0.28*	*> 50*	*< 40*	*NS*
Anacrotic	*PPT > OPT*	*NS*	*NS*	*NS*	*NS*

Note: ↑: High amplitude.

All resulting models were classified individually, except for the anacrotic models. Due to their limited appearance, the anacrotic pulses were sorted under the tardus category. Similarly, anacrotic pulses characterizing low amplitude were sorted under the parvus et tardus category. Additionally, a model that we refer to as "shallow pulse" was included to decrease the size of cases falling under the unidentified category. As **Table III.2** depicts, the shallow and shallow ↑ models share the same characteristics with the exception for the high amplitude.

6.1.2. Blood Pressure Class Level

The FSST-based features were sorted into three categories, each corresponding to a particular BP class label: HT, PHT, and NT, following the JNC7 guidelines [181]. It is crucial to acknowledge that a single BP reading is inadequate for establishing a hypertension diagnosis. Clinical literature emphasizes the need for multiple BP readings over time, as BP is known to fluctuate [226-227]. Therefore, the average SBP and DBP values ($(\overline{SBP})$, $(\overline{DBP})$) were calculated within each 1-minute ABP record. The BP class labels were then defined by comparing the computed $\overline{SBP}$ and $\overline{DBP}$ values against the clinical guidelines provided in the JNC7 report.

6.1.3. Blood Pressure Class Range

The PPG features were assigned different range-labels corresponding to SBP, DBP, and MAP values. The SBP interval spanning from 90 mmHg to 170 mmHg was divided into 5 mmHg ranges. Similarly, the DBP interval from 40 mmHg to 100 mmHg was divided into 5 mmHg ranges. Additionally, the MAP values ranging from 40 mmHg to 120 mmHg were divided into 5 mmHg ranges. The FSST-based features were sorted into categorical ranges, with each range corresponding to a particular class of the given BP interval. Specifically, the SBP values were calculated as the average of the systolic peaks from the ABP signal, while the DBP values represented the average of the trough values. The MAP values were computed by integrating the area under the curve of the given ABP signal.

6.2. Experiments

The present research investigates two distinct classification approaches. The first approach focuses on identifying AAP through the utilization of physiological PPG features. This approach was selected due to the potential for clinical implementation, given the inherent advantages in the interpretability of both the inputs and outputs, which were developed based on an evidence-based foundation.

The second experiment involves employing dimensionally-compressed FSST features to classify BP into categorical levels. This alternative approach is inherently geared towards the general population, particularly asymptomatic individuals who may benefit from earlier hypertension screening. Owing to the efficient and less complex preprocessing required, this approach holds the potential for implementation into affordable wearable or mobile PPG devices.

6.3. Data Preparation

To complete the data preparation, we assign class labels to each row of the input features based on its corresponding class label, as well as the specific classification task (AAP or BP levels). Next, we divide the input data into 80% training set and 20% test set. This division enables the classifiers to be trained on a majority of the data and evaluating their performance on unseen data during testing.

To address potential biases resulting from class imbalance, a data balancing process is applied to the training set. This involves oversampling the classes with low datasets by duplicating their instances until they reach a similar size to the class with the highest number of samples. This prevent the training model from favoring classes with larger datasets.

7. Evaluation Metrics

Different metrics are used to evaluate the classifiers' performances, including sensitivity (SE), specificity (SP), precision (PR), accuracy (AC) and F1 score (F1), and are defined as follows:

$$SE = \frac{TP}{TP + FN} \tag{34}$$

$$SP = \frac{TN}{TN + FP} \tag{35}$$

$$PR = \frac{TP}{TP + FP} \tag{36}$$

$$AC = \frac{TP + TN}{TP + FP + TN + FN} \tag{37}$$

$$F1 = \frac{2(SE \times PR)}{(SE + PR)} \tag{38}$$

In these equations, TP represents true positives, which are instances correctly identified as positive. TN represents true negatives, which are instances correctly identified as negative. FP represents false positives, which are instances incorrectly classified as positive. FN represents false negatives, which are instances incorrectly classified as negative.

Chapter IV

Classification Approach Assessment and its Implications for Applied Health Management

Reporting Key Insights and Findings from the Models and Discussing Opportunities for Improved Healthcare

1. Dataset Evaluation

1.1. Pulse Wave Features Detection

A core component of this research involved the extraction of PPG features through the segmentation of pulse waveform data. This segmentation process was facilitated by the implementation of customized algorithms designed to detect the dicrotic notch and pulse trough structures. Reliably identifying these temporal landmarks within the PPG morphology is crucial, as they delineate distinct physiological phases within the cardiac cycle. Additionally, retrospective analysis revealed a significant portion of signal records contained indistinct or absent dicrotic notch and trough features.

Furthermore, precisely locating troughs and dicrotic notches within the PPG waveform is equally indispensable for capturing critical hemodynamic parameters such as UT, ST, PP, DBP, AUNC, AUPC, DNL, DWA, OPT and PPT, all of which proved to be imperative inputs to the proposed AAP modeling frameworks. **Figure IV.1** displays sample outputs of the customized trough and dicrotic notch detection algorithms applied to ABP and PPG traces.

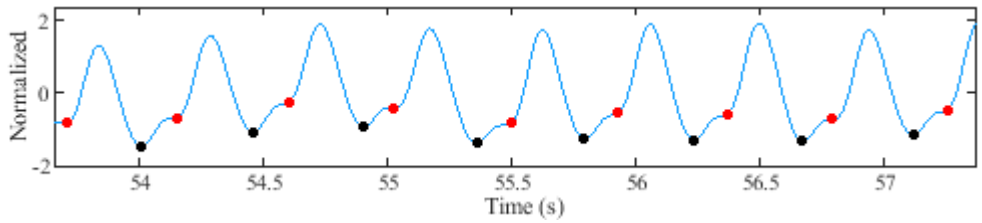

(a) Suppressed troughs in a PPG signal

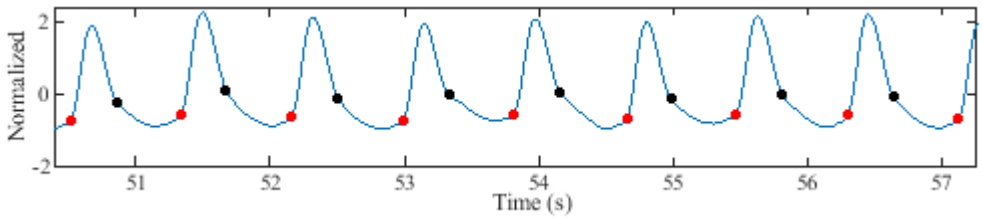

(b) Suppressed dicrotic noches in a PPG signal

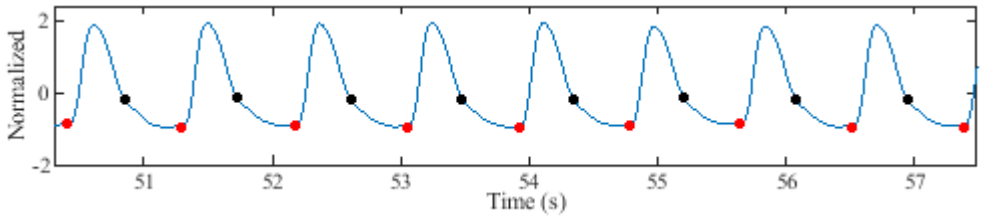

(c) Suppressed troughs and dicrotic noches in a PPG signal

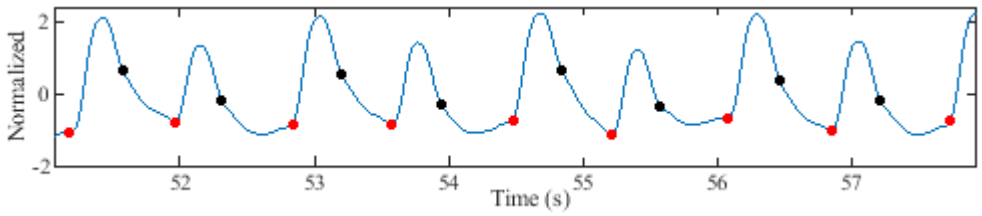

(d) A disturbing PPG signal with suppressed troughs and dicrotic notches

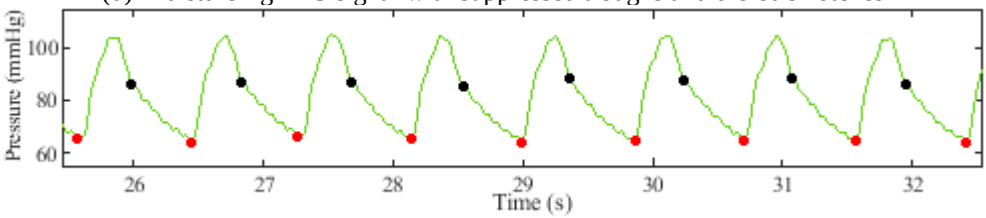

(e) Suppressed dicrotic notches in an ABP signal

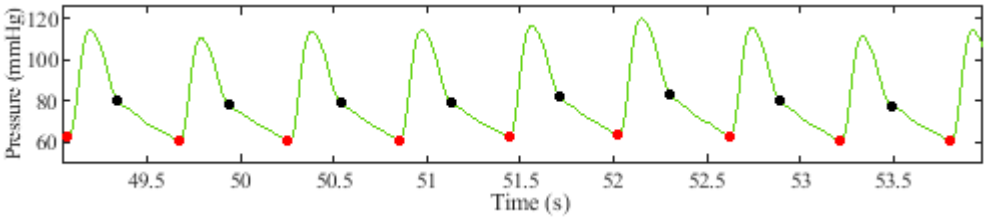

(f) Suppressed dicrotic notches in an ABP signal

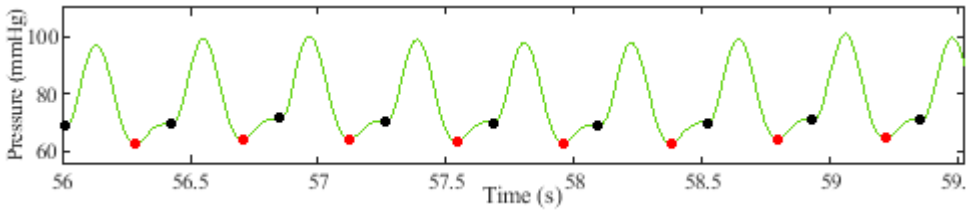

(g) Suppressed troughs in an ABP signal

Figure IV.1. Dicrotic notch and trough detection results

While **Figure IV.1** demonstrates that the proposed algorithms efficiently detect obscured troughs and dicrotic notches, visual validation alone is insufficient to fully assess their performance. This is because human physiology is dynamic, causing heartbeat features to vary within and across cardiac cycles in non-stationary ways [36].

Therefore, we proposed the SD metric to capture the temporal variation of dicrotic notches across the entire signal during the evaluation process. The underlying idea behind the SD metric was to ensure temporal consistency in the prevalence of dicrotic notches within a signal record. By enforcing this condition, the dicrotic notches occur in their natural positions even when the signal exhibits distinct morphological pulse patterns, as shown in **Figure IV.1 (d)**.

The SD metric can also be leveraged to evaluate the detected troughs by considering the variation in the length of pulses across the signal. To provide quantitative evaluation into the

detection performance, **Table IV.1** displays the average SD values for both detectors, extracted by analyzing over 200 signal-records during the detection process.

Table IV.1. SD metric evaluation results

Dicrotic notch		***Trough***	
PPG	***ABP***	***PPG***	***ABP***
1.22	*0.94*	*1.75*	*1.56*

Notably, the parameters used in the detection process addresses signals with Fs = 125 Hz, as in the MIMIC III database [182, 198]. Thus, it is imperative to perform further analysis when utilizing our approach for signals demonstrating higher sampling frequencies.

1.2. Class Labels

Thousands of AAP patterns were obtained from the modeling process across 9 AAP classes. The two remaining classes correspond to the normal and unidentified pulse patterns. **Figure IV.2** displays the sample sizes distribution among 11 classes, with each sample representing a group of models derived from a specific record.

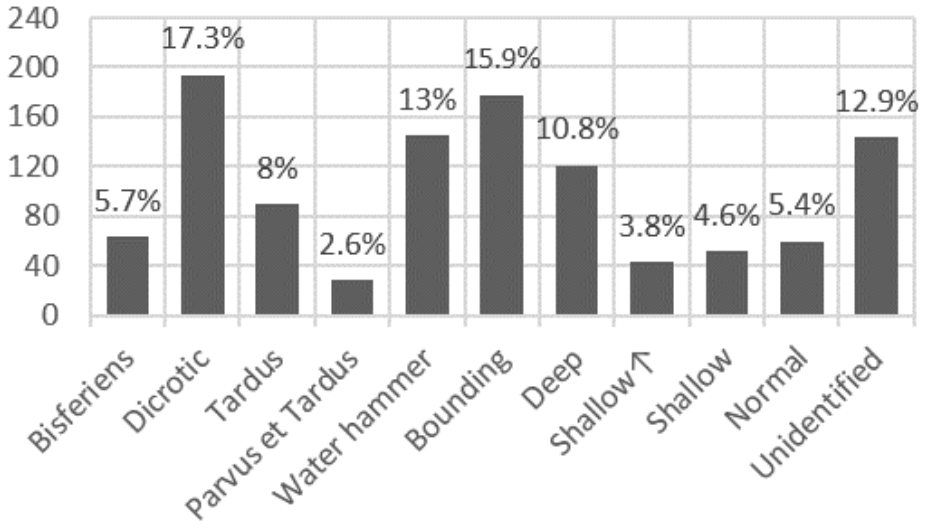

Figure IV.2. AAP classes distribution

The modeling process involved a total of 1120 ABP signal recordings. Analysis of the obtained records revealed a prevalence of similar pulse models within a given ABP signal, as depicted in **Figure IV.3**.

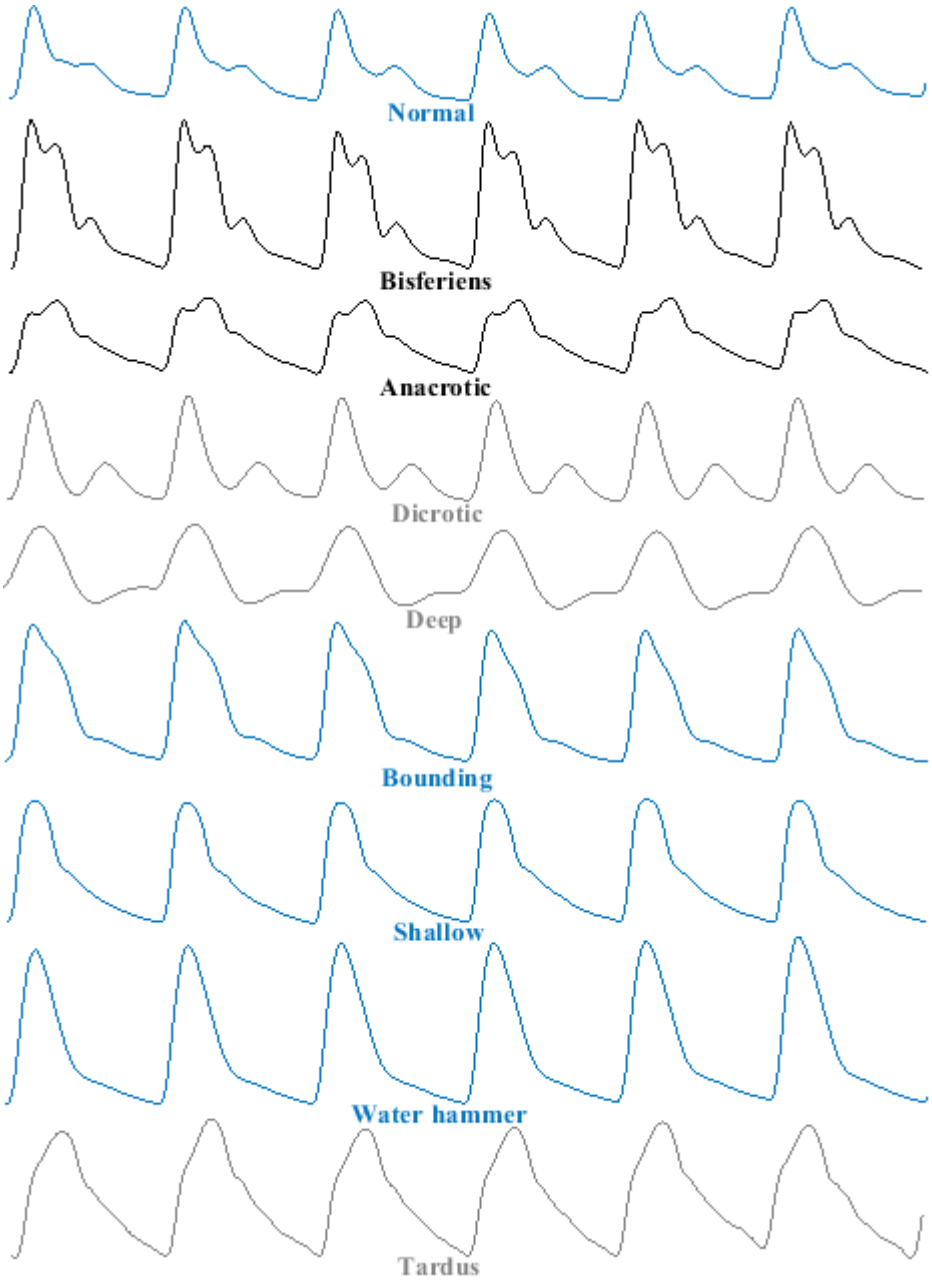

Figure IV.3. AAP model results taken from different ABP examples

Additionally, the collection process yielded ABP signals with SBP ranging 69-216 mmHg and DBP ranging 34-115 mmHg. **Figure IV.4** compares the diversity in BP values between the present dataset versus those used in prior works [36, 167], by considering the histogram's bin-widths as an evaluation metric.

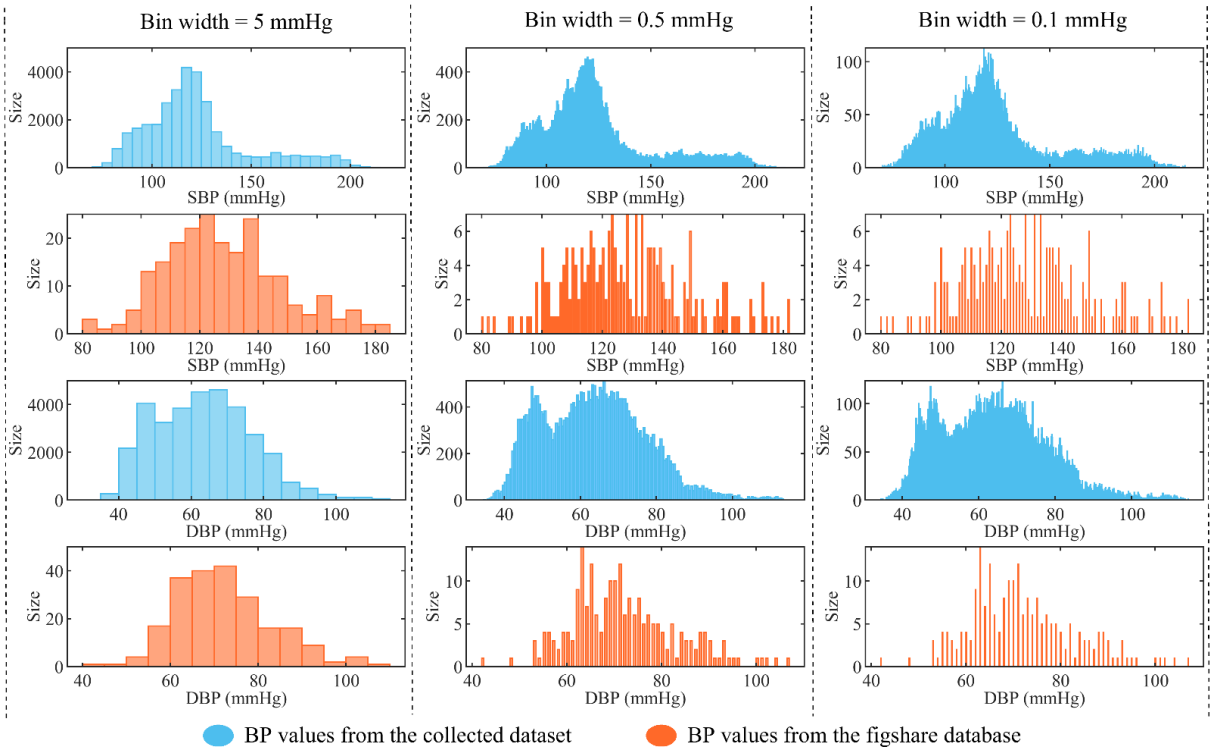

Figure IV.4. Blood pressure distribution comparison.

After categorizing the BP values following the jnc7 guidelines, the final dataset encompassed 6,068 hypertensive subjects, 9,010 prehypertensive subjects, and 16,024 normotensive subjects. The datasets were partitioned into separate training and test sets to allow for proper evaluation on new data. The training sets encompassed 5,568 HT subjects, 8,510 PHT subjects, and 15,524 NT subjects, Whereas the test sets comprised 500 subjects from each category. After balancing the training data, 15,524 subjects were obtained for each class.

1.3. Features Extraction

To capture meaningful physiological variations, features were extracted by identifying changes that occur at specific cardiac cycle landmarks. By segmenting the PPG pulse at these cardiac events six different sub-waves were obtained, each describing a particular cardiac event. Ultimately, four metrics - kurtosis, mean, slope and time - defined feature morphologies. Measurements were carried out from each segment, yielding 24 features per pulse (6 segments x 4 metrics). The features were then assigned to 11 AAP class labels created via a modeling process applied on pre-segmented ABP pulses. In total, the final dataset comprised 24 x 47,000 feature samples.

The FSST produced a 250 x 11 complex-valued matrix, with rows representing reassigned time instances and columns representing frequency bins. The 250 rows correspond to the

original 250 signal samples, indicating continuous time after reassignment. The 11 columns represent the unique frequency components needed to characterize the real input signal's spectrum. Specifically, due to conjugate symmetry of the FT of real signals, the full spectrum can be compactly represented using only 11 non-redundant frequency bins, rather than the full FFT length. Dimensionality reduction were performed following two optimizations approaches, including statistical and cuckoo search optimizations.

Statistical optimization involved processing each frequency bin column to extract four distinct features, rather than utilizing all 250 complex time values. This compacted the FSST dimensions into 4 x 11. As a result, 44 feature set will be employed for BP classification. Metaheuristic optimization involved applying a cuckoo search to reduce the feature space dimensions. This decreased the FSST dimensions to 40 samples during 30 iterations. The objective function used for this purpose is the KNN algorithm, with k=1.

2. Machine Learning Modeling

2.1. Classifiers Evaluation for AAP Prediction

We evaluated several ML models in MATLAB R2020a, including NB, LDA, SVM, KNN, DT, and BT. These classifiers were optimized following the Bayesian approach integrated in the software's classification learner toolbox. Models were developed using a subset of 27,000 samples from the full dataset, labeled with 11 classes. 80% of the data was used for training and the remaining 20% for testing. As illustrated in **Table IV.2**, KNN and BT significantly outperformed other models in terms of training time, accuracy, prediction speed, and test accuracy. This proves their effectiveness in addressing multiclass challenges and nonlinear relationships within the dataset.

Table IV.2. Models comparison performance in AAP classification

	KNN	***BT***	***DT***	***LDA***	***SVM***	***NB***
Training accuracy (%)	*98.2*	*97.7*	*69.7*	*59.6*	*61.5*	*54.3*
Training time (sec)	*79*	*11*	*9*	*8*	*1722*	*8*
Prediction speed (obs/sec)	*2000*	*69000*	*210000*	*130000*	*6800*	*87000*
Test accuracy	*92.5*	*90.2*	*67.5*	*61.5*	*35.6*	*57*

Notes: 1. obs: observation. 2. sec: second

The results in **Table IV.2** show that LDA and NB provided fast training times of 8 seconds and high prediction speeds up to 210,000 observations per second. However, their accuracy on both the training and test sets was relatively low. This likely occurred because the underlying

assumptions of these parametric models did not match the actual data distribution. This confirms that parametric models struggle with nonlinear relationships in data. SVM training took much longer at 1722 seconds to achieve only 61.5% and 35.6% accuracy on training and test sets respectively. In addition to its computational expense, SVM seems to have overfitted the data. Decision trees also learned patterns quickly in 9 seconds but had relatively low accuracies. Overall, the results indicate the models were not effective at handling the multi-class problems. With more classes, there is less average training data per class, making class boundaries harder to learn precisely.

To further analyze KNN and BT, their hyperparameters were tuned. K values for KNN ranged from 1 to 10, and learners varied for BT from 10 to 200. **Figure IV.5** shows how training and test accuracy changed with these different hyperparameters.

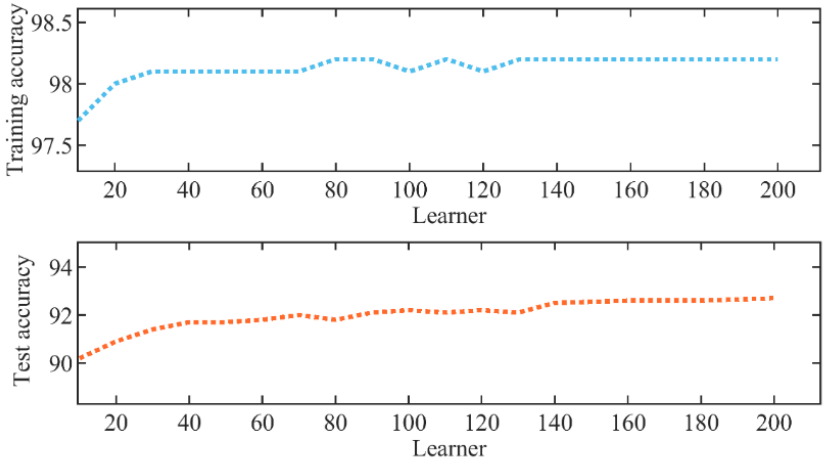

(a) Learner variation versus accuracies

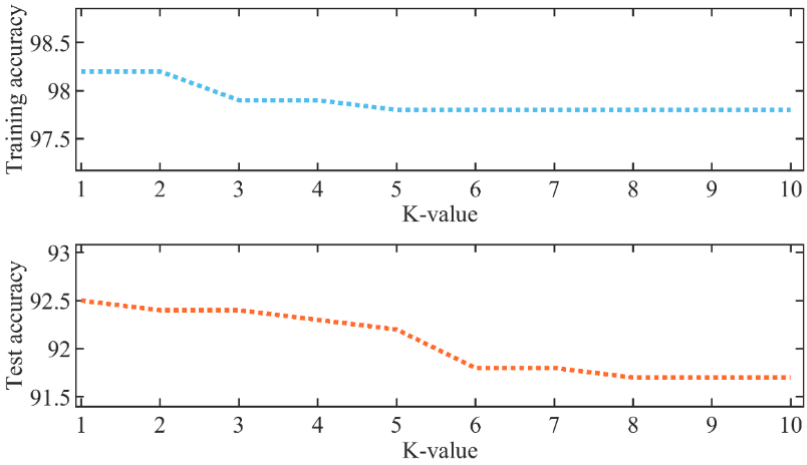

(b) K-value variation versus accuracies

Figure IV.5. KNN and BT parameter optimization

Figure IV.5 (a) shows that as the number of neighbors (K) increased for KNN, both the training and test accuracy progressively decreased. This indicates optimal performance was achieved with a single neighbor, emphasizing simpler KNN models can produce more accurate results. In contrast, **Figure IV.5 (b)** demonstrates that BT required 200 learners to reach the highest levels of accuracy. This emphasizes that more complex models are better suited for multiclass problems. Overall, the tuning process validated the suitability of both KNN and BT for addressing these nonlinear, multiclass classification challenges. KNN performed best with a simple single-neighbor implementation, while BT benefited from a more complex structure involving 200 learners.

3. Classification Performance Evaluation

3.1. Abnormal Arterial Pattern Classification

In the first stage of the present study, we sought to develop a PPG-based classification system for predicting different AAPs morphologies, clinically proven being disease indicators. Towards this goal, the MATLAB Classification Learner application was utilized to train and validate KNN and BT classifiers using a dataset comprised of 24 features across 47,000 samples. In accordance to MRMR importance scores (**Figure IV.6**), the six best parameters were fed into the classifiers for performance evaluation. Consistent with the hyperparameter optimization process, the KNN model was parameterized with K=1 while the BT model employed 200 learners. The results confirm that both ML algorithms, when implemented according to the respective tuned configurations, achieved sound predictive capabilities as evidenced in **Table IV.3**. This validates the utility of the proposed physiology-based approach for CVD management.

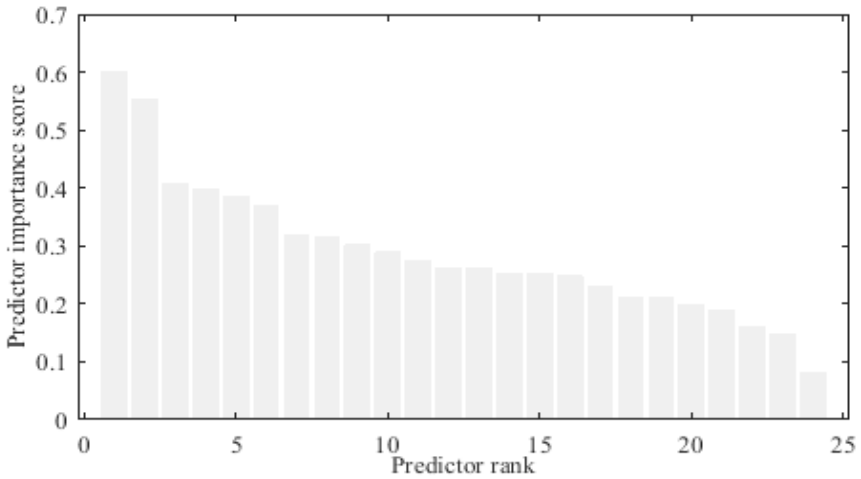

Figure IV.6. Feature importance analysis

Table IV.3. AAP classification results

Input parameters	***Training accuracy (%)***		***Test accuracy (%)***	
	BT	***KNN***	***BT***	***KNN***
All parameters	*97.6*	*97.5*	*91*	*90.9*
6-MRMR parameters	*93.5*	*93.6*	*90.5*	*90.5*

As shown in **Table IV.3**, the BT model achieved an overall training accuracy of 97.6% on the data, slightly outperforming the KNN model which attained a training accuracy of 97.5%. On independent testing data, the BT model maintained a testing accuracy of 91%, while KNN achieved 90.9% accuracy. Though the differences in performance are minor, it is apparent from these results that the BT classifier performed marginally better than KNN at both training and testing stages. Nonetheless, both ML models proved to be effective predictors of AAP patterns, with testing accuracies over 90%, validating the predictive capability of the proposed PPG-based classification framework implemented through these algorithms.

However, a more reliable evaluation of predictive performance relies primarily on analysis of testing results. Furthermore, to gain deeper insight, it is crucial to assess each class individually rather than solely reporting aggregate accuracy. This is particularly important when working with multiple classes, as achieving high overall accuracy can obscure poor prediction of specific classes. Metrics such as specificity and accuracy that incorporate true negative classes into their calculation are thus prone to inflating performance. Instead, sensitivity, precision and F1 score provide more suitable measures for assessing each class separately, as they focus only on true positives. As shown in **Table IV.4**, reporting these alternative metrics on a per-class basis offers valuable perspective, particularly when some classes may have relatively few samples. Such an analysis more rigorously substantiates the reliability and limitations of the classification system for predicting multiclass outputs.

Specifically, the BT model achieved a sensitivity of 95.1%, precision of 96.2% and F1 score of 95.6% for the 'deep' class, while the KNN model attained a sensitivity of 95.7%, precision of 95.4% and F1 score of 95.6% for the same class. Conversely, the 'shallow↑' class exhibited the lowest values for the BT model with a sensitivity of 83.7%, precision of 85.4% and F1 score of 84.5%. Similarly, the 'parvus et tardus' class displayed the weakest prediction for the KNN model, attaining a sensitivity, precision and F1 score of 84.8%. This in-depth evaluation on an individual class basis reveals some classes are predicted more reliably than

others, with 'deep' predicted best and 'shallow↑' or 'parvus et tardus' predicted most poorly depending on the classifier.

Table IV.4. AAP test performance results

Classes	*Sensitivity (%)*		*Specificity (%)*		*Precision (%)*		*Accuracy (%)*		*F1-Score (%)*	
	BT	***KNN***	***BT***	***KNN***	***BT***	***KNN***	***BT***	***KNN***	***BT***	***KNN***
Bisferiens	*93*	*92.3*	*99*	*99.3*	*89.8*	*92.3*	*98.5*	*98.6*	*91.4*	*92.3*
Dicrotic	*94.9*	*94*	*98.6*	*98.4*	*94.5*	*93.9*	*97.8*	*97.5*	*94.7*	*93.9*
Tardus	*91.7*	*91.3*	*98.9*	*99.2*	*86.6*	*90*	*98.3*	*98.6*	*89.1*	*90.6*
Parvus et tardus	*83*	*84.8*	*99.8*	*99.6*	*92.8*	*84.8*	*99.4*	*99.2*	*87.7*	*84.8*
Water hammer	*87.8*	*89.1*	*98.2*	*98.1*	*88.3*	*87.7*	*96.8*	*96.8*	*88.1*	*88.4*
Bounding	*86.8*	*86*	*98.1*	*98.3*	*88.8*	*90*	*96.4*	*96.5*	*87.8*	*88*
Deep	*95.1*	*95.7*	*99.3*	*99.2*	*96.2*	*95.4*	*98.7*	*98.6*	*95.6*	*95.6*
Shallow ↑	*83.7*	*84.2*	*99.6*	*99.6*	*85.4*	*85.9*	*99.1*	*99.1*	*84.5*	*85.1*
Shallow	*92*	*94.4*	*99.5*	*99.4*	*89.2*	*88.8*	*99.1*	*99.2*	*90.5*	*91.5*
Normal	*86.1*	*85.1*	*99.5*	*99.4*	*89.2*	*86.6*	*98.9*	*98.7*	*87.6*	*85.9*
Unidentified	*90.9*	*90.5*	*98.6*	*98.5*	*90.1*	*89.4*	*97.6*	*97.5*	*90.5*	*90*

Additionally, as seen in **Table IV.4**, certain classes such as 'dicrotic', 'bisferiens', 'shallow', and 'tardus' demonstrated sensitivity, precision and F1 score values close to those achieved for the 'deep' class by both the BT and KNN models. This suggests these classes were also predicted reliably. Conversely, classes including 'water hammer', 'bounding', and 'normal' showed performance metrics nearer to those of the 'shallow↑' and 'parvus et tardus' classes, implying weaker prediction. However, overall the findings demonstrate both models consistently exhibited comparable prediction capability across different classes, with some classes predicted more effectively than others. This consistent class-level performance, despite variation, indicates the proposed PPG-based approach shows promise as an effective detector of various types of arterial pressure abnormalities through both the BT and KNN classifiers.

3.2. Blood Pressure Level Classification

The second stage in this study presented a system designed to classify BP levels based on PPG signals. The system was evaluated experimentally using three separate models trained on

datasets comprising distinct features extracted via FSST. BT classifiers were employed to develop each experimental model. As shown in **Table IV.5**, training each model required approximately 4 minutes, a reasonable duration given the sizable datasets involved. Model performance was assessed based on overall accuracy, confusion matrices, and F1 score through focused classification tasks as outlined below.

Table IV.5. BP classification results

Input parameters	*Results*	*Model 1*	*Model 2*	*Model 3*
Statistical parameters	*Training accuracy (%)*	*100*	*100*	*100*
	Prediction speed (obs/s)	*6600*	*4700*	*4600*
	Training time (s)	*248*	*237*	*226*
	Test accuracy (%)	*96.9*	*95.7*	*96.1*
Cuckoo parameters	*Training accuracy (%)*	*100*	*100*	*100*
	Prediction speed (obs/s)	*8000*	*6200*	*5800*
	Training time (s)	*200*	*194*	*188*
	Test accuracy (%)	*97*	*96*	*95.3*

As shown in **Table IV.5**, the proposed methodology demonstrated effective performance across the three experimental models. Each model achieved 100% training accuracy, indicating the BT classifiers learned the training data perfectly. Upon testing, experiments 1, 2 and 3 attained accuracies ranging between 95.3% and 97% across different input parameters. It is apparent from these results that experiment 1 performed marginally better than the others at the testing stage, though all three models proved capable of accurately predicting BP levels, with testing accuracies over 95%. This validates the feasibility of the statistical and cuckoo-based optimizations for deriving distinguishable features from FSST data to classify BP values using tunable BT models.

The training and testing confusion matrices presented in Figures 6 and 7 offer meaningful perspective on model performance. Within the matrices, the diagonal blue cells represent true positives/true negatives, indicating instances where the predicted and actual classes matched. Meanwhile, the off-diagonal red cells reflect false positives/false negatives, where the predicted and actual classes differed. The columns denote the predicted classes along the output axis, and the rows indicate the true classes along the target axis. Additionally, the grey shaded cells convey important evaluation metrics - the positive predictive values are shown column-wise, while the true positive rates are depicted row-wise.

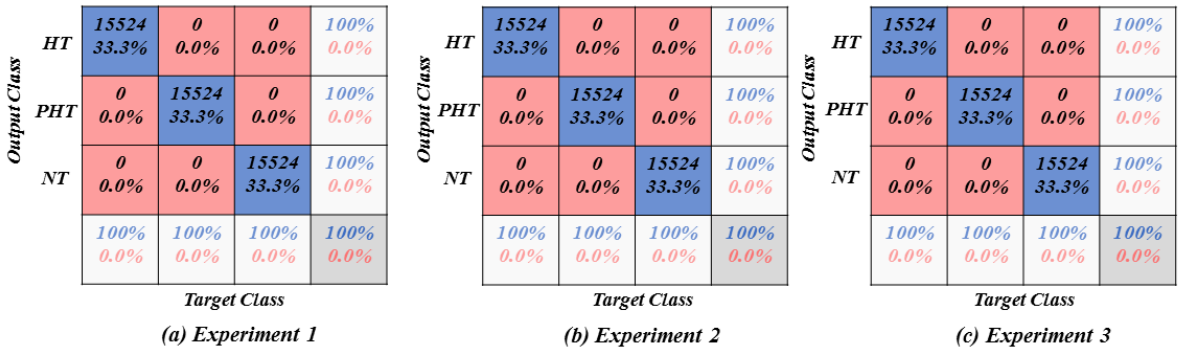

Figure IV.7. Training confusion matrices of the three experiments using cuckoo search and statistical analysis.

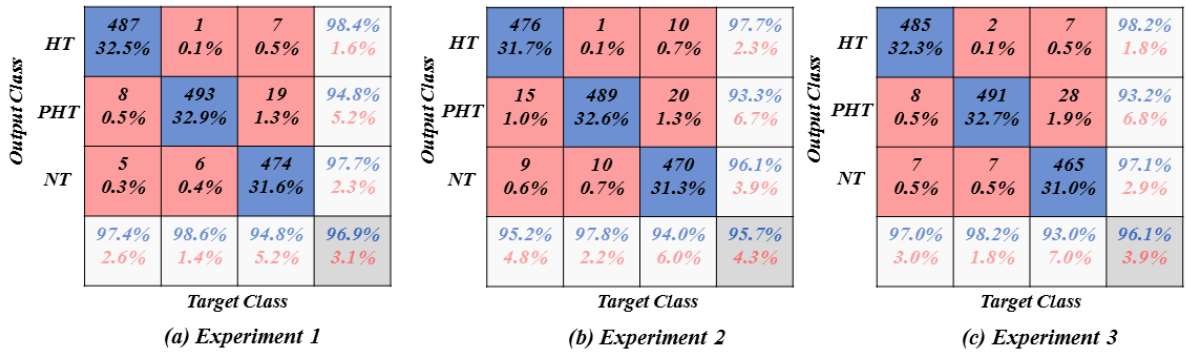

Figure IV.8. Test confusion matrices of the three experimental models using statistical analysis.

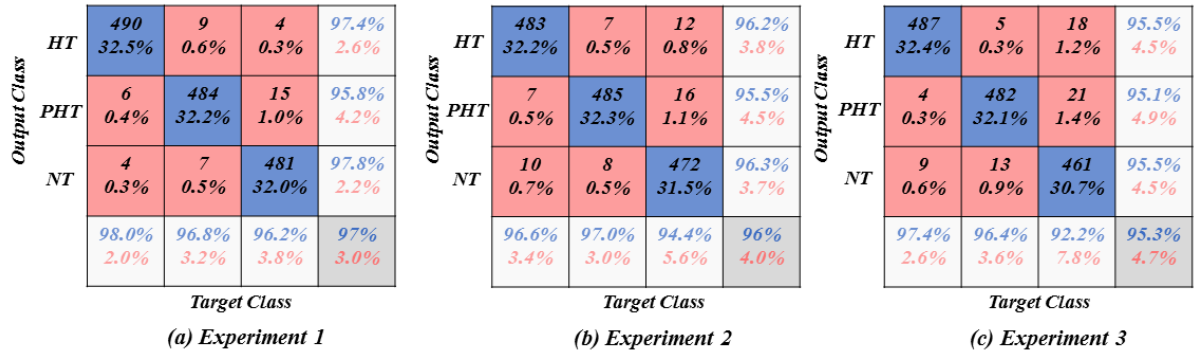

Figure IV.9. Test confusion matrices of the three experimental models using cuckoo search.

The above confusion matrices represent the results achieved using statistical and cuckoo search parameters across the three experiments. While the training confusion matrices confirmed 100% accuracy distinguishing between actual cases within each class and 100% correct classification of all predicted cases, a more reliable evaluation relies primarily on analysis of test performance.

Specifically, as shown in the testing confusion matrix for Experiment 1 in **Figure IV.7**, it correctly classified 97.4% of actual HT cases, 94.8% of actual PHT cases, and 98.6% of actual NT cases. Furthermore, of all HT, PHT and NT predictions made by Experiment 1, 98.4%,

97.7% and 94.8% were correctly classified, respectively. Similarly, Experiment 2 correctly classified 95.2% of actual HT cases, 94% of actual PHT cases, and 97.8% of actual NT cases, while indicating that of all HT, PHT and NT predictions, 97.7%, 96.1% and 93.3% were correctly classified, respectively. Furthermore, Experiment 3 correctly classified 97% of actual HT cases, 93% of actual PHT cases, and 98.2% of actual NT cases, while indicating that of all HT, PHT and NT predictions, 98.2%, 97.1% and 93.2% were correctly classified, respectively.

Similarly, in **Figure IV.8**, the testing confusion matrix for Experiment 1 correctly classified 98% of actual HT cases, 96.2% of actual PHT cases, and 96.8% of actual NT cases. Additionally, of all HT, PHT and NT predictions made by Experiment 1, 97.4%, 97.8% and 95.8% were correctly classified, respectively. Further, Experiment 2 correctly classified 96.6% of actual HT cases, 94.4% of actual PHT cases, and 97% of actual NT cases, while indicating that of all HT, PHT and NT predictions, 96.2%, 96.3% and 95.5% were correctly classified, respectively. Finally, Experiment 3 correctly classified 97.4% of actual HT cases, 92.2% of actual PHT cases, and 96.4% of actual NT cases, while indicating that of all HT, PHT and NT predictions, 95.5%, 95.5% and 95.1% were correctly classified, respectively.

To further evaluate classification performance, the proposed models underwent three classification trials in line with previous related work [31-34]: non-HT (NT + PHT) vs HT, NT vs HT, and NT vs PHT. **Table IV. 6-11** provide detailed performance metrics for Models 1-3 across each trial using both statistical and cuckoo search parameters. This including F1 score, precision, specificity and sensitivity.

When employing statistical parameters, model 3 attained the best F1 score reaching 99% for the NT vs HT task, while Models 1-2 scored 97.5-98%. Meanwhile, Model 1 outperformed for non-HT vs HT with an F1 score attaining 99%, and NT vs PHT at 99.1%, whereas Models 2-3 scored 98.9-96.6% and 98.8-98.8% respectively.

Table IV.6. The models' performances of experiment 1 using statistical parameters.

Trial	*TP*	*TN*	*FP*	*FN*	*Specificity (%)*	*Precision (%)*	*Sensitivity (%)*	*F1 score (%)*
PHT	*474*	*980*	*11*	*26*	*98.9*	*97.7*	*94.8*	*96.2*
HT	*487*	*967*	*8*	*13*	*99.2*	*98.4*	*97.4*	*97.9*
NT	*493*	*961*	*27*	*7*	*97.3*	*94.8*	*98.6*	*96.7*
NT vs PHT	*493*	*474*	*1*	*8*	*99.8*	*99.8*	*98.4*	*99.1*
NT vs HT	*493*	*487*	*19*	*6*	*96.3*	*96.3*	*98.8*	*97.5*
(NT + PHT) vs HT	*992*	*487*	*13*	*8*	*97.4*	*98.7*	*99.2*	*99*

Table IV.7. The models' performances of experiment 2 using statistical parameters.

Trial	*TP*	*TN*	*FP*	*FN*	*Specificity (%)*	*Precision (%)*	*Sensitivity (%)*	*F1 score (%)*
PHT	*470*	*965*	*19*	*30*	*98.1*	*96.1*	*94*	*95*
HT	*476*	*959*	*11*	*24*	*98.9*	*97.7*	*95.2*	*96.4*
NT	*489*	*946*	*35*	*11*	*96.4*	*93.3*	*97.8*	*95.5*
NT vs PHT	*489*	*470*	*20*	*10*	*96*	*99.8*	*98*	*98.9*
NT vs HT	*489*	*476*	*15*	*1*	*97*	*96.3*	*99.8*	*98*
(NT + PHT) vs HT	*989*	*476*	*24*	*11*	*97.1*	*98.6*	*98.9*	*98.8*

Table IV.8. The models' performances of experiment 3 using statistical parameters.

Trial	*TP*	*TN*	*FP*	*FN*	*Specificity (%)*	*Precision (%)*	*Sensitivity (%)*	*F1 score (%)*
PHT	*465*	*976*	*14*	*35*	*98.6*	*97.1*	*93*	*95*
HT	*485*	*956*	*9*	*15*	*99.1*	*98.2*	*97*	*97.6*
NT	*491*	*950*	*36*	*9*	*96.4*	*93.2*	*98.2*	*95.6*
NT vs PHT	*491*	*465*	*28*	*7*	*94.3*	*94.6*	*98.6*	*96.6*
NT vs HT	*491*	*485*	*8*	*2*	*98.4*	*98.4*	*99.6*	*99*
(NT + PHT) vs HT	*991*	*485*	*15*	*9*	*97*	*98.5*	*99.1*	*98.8*

When employing cuckoo search parameters, model 1 attained the best F1 score reaching 99.2% for the NT vs HT task, while Models 2-3 scored 97.7-99%. Additionally, Model 1 outperformed for non-HT vs HT with an F1 score attaining 98.9%, and NT vs PHT at 97.8%, whereas Models 2-3 scored 98.2-97.1% and 97.3-96.4% respectively. Overall, the models demonstrated comparable performance across all trials, validating their impressive abilities for detecting different BP levels.

Table IV.9. The models' performances of experiment 1 using cuckoo search parameters.

Trial	*TP*	*TN*	*FP*	*FN*	*Specificity (%)*	*Precision (%)*	*Sensitivity (%)*	*F1 score (%)*
PHT	*484*	*971*	*21*	*16*	*97.9*	*95.8*	*96.8*	*96.3*
HT	*490*	*965*	*13*	*10*	*98.7*	*97.4*	*98*	*97.7*
NT	*481*	*974*	*11*	*19*	*98.9*	*97.7*	*96.2*	*96.9*
NT vs PHT	*481*	*484*	*15*	*7*	*97*	*97*	*98.6*	*97.8*
NT vs HT	*481*	*490*	*4*	*4*	*99.2*	*99.2*	*99.2*	*99.2*
(NT + PHT) vs HT	*987*	*490*	*10*	*13*	*98*	*99*	*98.7*	*98.9*

Table IV.10. The models' performances of experiment 2 using cuckoo search parameters.

Trial	*TP*	*TN*	*FP*	*FN*	*Specificity (%)*	*Precision (%)*	*Sensitivity (%)*	*F1 score (%)*
PHT	*485*	*955*	*23*	*15*	*97.7*	*95.5*	*97*	*96.2*
HT	*483*	*957*	*19*	*17*	*98.1*	*96.2*	*96.6*	*96.4*
NT	*472*	*968*	*18*	*28*	*98.2*	*93.3*	*94.4*	*93.5*
NT vs PHT	*472*	*485*	*16*	*8*	*96.8*	*96.3*	*98.3*	*97.3*
NT vs HT	*472*	*483*	*12*	*10*	*97.6*	*97.5*	*97.9*	*97.7*
(NT + PHT) vs HT	*957*	*483*	*17*	*19*	*96.6*	*98.3*	*98.1*	*98.2*

Table IV.11. The models' performances of experiment 3 using cuckoo search parameters.

Trial	*TP*	*TN*	*FP*	*FN*	*Specificity (%)*	*Precision (%)*	*Sensitivity (%)*	*F1 score (%)*
PHT	*482*	*948*	*25*	*18*	*97.4*	*95.1*	*96.4*	*95.8*
HT	*487*	*943*	*23*	*13*	*97.6*	*95.5*	*97.4*	*96.4*
NT	*461*	*969*	*22*	*39*	*97.8*	*95.5*	*92.2*	*93.8*
NT vs PHT	*461*	*482*	*21*	*13*	*95.8*	*95.6*	*97.3*	*96.4*
NT vs HT	*461*	*487*	*18*	*9*	*96.4*	*96.2*	*98.1*	*99*
(NT + PHT) vs HT	*943*	*487*	*13*	*23*	*97.4*	*98.6*	*97.6*	*97.1*

3.3. Blood Pressure Ranges Classification

BP range classification was conducted by training FSST-derived features using a BT classifier. SBP and MAP classification involved 16 categorical classes each, while DBP encompassed 12 classes. The BT classifier achieved 100% training accuracy according to results reported in **Tables IV.12-14**, effectively distinguishing between multiple BP range classes during model fitting. However, test set accuracies were relatively lower. Specifically, statistical BT parameters yielded classification accuracies of 92.4-93% for SBP ranges, 90-92.2% for DBP ranges, and 90.4-92.3% for MAP ranges. Metaheuristic BT parameters optimized via cuckoo search algorithms achieved test accuracies of 91.8-93.1% for SBP, 90.6-90.9% for DBP, and 92.1-93.6% for MAP range classification.

Table IV.12. SBP ranges classification results

Input parameters	*Results*	*Model 1*	*Model 2*	*Model 3*
Statistical parameters	*Training accuracy (%)*	*100*	*100*	*100*
	Test accuracy (%)	*93*	*92.8*	*92.4*
Cuckoo parameters	*Training accuracy (%)*	*100*	*100*	*100*
	Test accuracy (%)	*92.7*	*91.8*	*93.1*

Table IV.13. DBP ranges classification results

Input parameters	*Results*	*Model 1*	*Model 2*	*Model 3*
Statistical parameters	*Training accuracy (%)*	*100*	*100*	*100*
	Test accuracy (%)	*91*	*90*	*92.2*
Cuckoo parameters	*Training accuracy (%)*	*100*	*100*	*100*
	Test accuracy (%)	*90.9*	*90.7*	*90.6*

Table IV.14. MAP ranges classification results

Input parameters	*Metric*	*Model 1*	*Model 2*	*Model 3*
Statistical parameters	*Training accuracy (%)*	*100*	*100*	*100*
	Test accuracy (%)	*91.5*	*92.3*	*90.4*
Cuckoo parameters	*Training accuracy (%)*	*100*	*100*	*100*
	Test accuracy (%)	*92.5*	*93.6*	*92.1*

The results demonstrated that FSST transformation coupled with BT ensembles provided an effective supervised learning framework for distinguishing between multiple discrete BP levels based on classification of BP range categories. Perfect training accuracy was achieved by all models, whereas test set performance was relatively lower. This suggests the models may have overfit the training data, as evidenced by decreased generalization to novel test examples not seen during fitting.

The potential for overfitting has important implications for constraining the utility of BP range classification in downstream BP estimation tasks. Misclassification errors would provide regression models with incorrect BP value ranges as inputs, resulting in irrelevant BP predictions that do not accurately reflect the patients' true hemodynamic states. Hence, further parameter optimization is warranted to enhance test set classification accuracy and minimize overfitting. Reducing the gap between training and testing metrics is crucial for developing classification frameworks with robust predictive capabilities on independent data.

3.4. Feature redundancy optimization results

While the developed models demonstrated potential utility for arterial pressure prediction tasks, overfitting challenges necessitated further methodological refinement to enhance generalizability. Accordingly, FRV approach was carried out to improve the test accuracies of the models, as reported in **Table IV.15**. FRV was applied to the models exhibiting the lowest initial performance. This included the AAP model constructed with 6-MRMR features; the BP level model utilizing FSST experimental configuration 3 with cuckoo search parameters; and the MAP range classifier leveraging FSST experiment 1 optimized via cuckoo search.

Table IV.15. FRV classification results

Redundant parameters	*AAPs*	*BP ranges*	*BP levels*
1	*90.5 %*	*90.9 %*	*95.3 %*
15	*92.8 %*	*91.7 %*	*96.8 %*
20	*95.9 %*	*93.4 %*	*97.3 %*
25	*96.0 %*	*95.1 %*	*97.9 %*

As shown in **Table IV.15**, FRV successfully enhanced test accuracies across these classifiers by increasing parameter redundancy. For the AAP, BP level, and MAP models, classification performance improved from 90.5% to 96.0%, 95.3% to 97.9%, and 90.9% to 95.1%, respectively. This validation of FRV's ability to mitigate overfitting and enhance generalization validates its potential as a performance-boosting approach.

4. Comparative Analysis with Prior Work

4.1. Blood Pressure Level Classification

This section assesses the system's classification performance in comparison to previous research. **Table IV.16** contrasts F1 scores from the current work against other studies [36, 104, 105, 167] for classification tasks involving normal and pre-hypertensive subjects versus hypertensive subjects, normal versus pre-hypertensive subjects, and normal versus hypertensive subjects. Based on the comparison findings, the proposed models in this work show greater robustness and efficiency. A key reason is that the models have learned from a much more significant and diverse dataset incorporating a broader range of BP values, an element not taken into account in earlier studies.

Table IV.16. BP results comparison against previous studies

Approach	*Classification task*	*Features*	*Research subjects*	*Classifier*	*F1 score*		
PAT features [105] (PPG and ECG signals)	*NT (46 TS) vs HT (34 TS)* *NT (46 TS) vs PHT (41 TS)* *(NT + PHT) (87 TS) vs HT (34 TS)*	*PAT and 10 PPG features*	*121 subjects*	*KNN*	*84.34 %* *94.84 %* *88.49%*		
PPG features [105] (only PPG signals)	*NT (46 TS) vs HT (34 TS)* *NT (46 TS) vs PHT (41 TS)* *(NT + PHT) (87 TS) vs HT (34 TS)*	*10 PPG features*	*121 subjects*	*KNN*	*78.62 %* *86.94 %* *78.44 %*		
Raw PPG Signal [104]	*NT (46 TS) vs HT (34 TS)* *NT (46 TS) vs PHT (41 TS)* *(NT + PHT) (87 TS) vs HT (34 TS)*	*RGB images using CWT (scalogram)*	*2904 subjects (images)*	*CNN*	*80.52 %* *92.55 %* *82.95 %*		
Raw PPG Signal [167]	*NT (46 TS) vs HT (34 TS)* *NT (46 TS) vs PHT (41 TS)* *(NT + PHT) (87 TS) vs HT (34 TS)*	*2100 PPG features points*	*900 subjects*	*KNN*	*100 %* *100 %* *90. 80 %*		
Raw PPG Signal [36]	*NT (38 TS) vs HT (38 TS)* *NT (38 TS) vs PHT (38 TS)* *(NT + PHT) (76 TS) vs HT (38 TS)*	*TF-features using STFT*	*900 subjects*	*BLSTM*	*97.29 %* *97.39 %* *93.93 %*		
This study	*NT (500 TS) vs HT (500 TS)* *NT (500 TS) vs PHT (500 TS)* *(NT + PHT) (1000 TS) vs HT (500 TS)*	*44 FSST features using statistical analysis*	*48,072 subjects*	*BT*	***EXP1*** *97.5 %* *99.1 %* *99 %*	***EXP2*** *98 %* *98.9 %* *98.8 %*	***EXP3*** *99 %* *96.6 %* *98.8 %*

This study	*NT (500 TS) vs HT (500 TS)* *NT (500 TS) vs PHT (500 TS)* *(NT + PHT) (1000 TS) vs HT (500 TS)*	*40 FSST features using metaheuristic*	*48,072 subjects*	*BT*	***EXP1*** *98 %* *99.4 %* *99.2 %*	***EXP2*** *98.3 %* *99 %* *98.9 %*	***EXP3*** *97.3 %* *95.7 %* *97.5 %*

Furthermore, even though the dataset was large in size, it took around 4 minutes only to train each of the experimental models in our study, significantly faster than prior methods. For instance, the BLSTM model from Tjahjadi et al. [36] needed over 30 minutes to train using a smaller 786 data samples. Liang et al.'s CNN model [104] was even slower, exceeding 350 minutes using 2323 samples. This validates the superior learning speed of the BT classifier compared to previous approaches.

In terms of feature extraction, earlier studies had some limitations that our work aimed to address. For instance, a study by Liang et al. [105] evaluated KNN models using PPG data with and without PAT features. While the results were promising, utilizing PAT requires an extra sensor beyond just PPG. Additionally, extracting morphological shape features necessitates high quality PPG signals [104], as they can be impacted by motion artifacts [38]. In our work, we were able to achieve high performance using few TF features directly calculated from the PPG signal, without needing special morphological preprocessing to locate specific features.

In comparison to prior work, this study aimed to address some limitations in feature extraction. For instance, one paper evaluated KNN models utilizing PPG data both with and without PAT features [105]. While the results were promising, incorporating PAT necessitated an extra sensor beyond PPG. Separately, deriving morphological characteristics necessitated high-quality PPG recordings [104], since they can be impacted by movement interference [38]. Alternatively, the proposed system in this research achieved high performance relying solely on 44 statistical features or 40 metaheuristic features directly computed from the transformed PPG signals, without needing specialized preprocessing to locate features. This obviated the requirement for supplemental sensors or dependence on high quality PPG signals.

In addition, although the studies in [36, 167] achieved the highest F1 scores up to that point, their datasets lacked variety in BP ranges (as shown in **Figure IV.4)** and the models were assessed on small test sets. In contrast, our models kept consistent F1 scores for all tasks while addressing limitations of previous works, such as complex preprocessing needs, lengthy training times, and limited amount of data.

4.2. Cardiovascular Disease Management

Table IV.17 summarizes various methods employed in developing CVD diagnostic systems, outlining their respective outputs, associated medical conditions, classification algorithms, input data features, and accuracy levels. The present system's key strength lies in its capability to handle multiple tasks simultaneously, as demonstrated by the range of related pathologies it can address. Nonetheless, transparency is an indispensable factor in healthcare systems, necessitating a balanced approach between performance and simplicity at both the component and individual case levels. Despite previous studies attaining high accuracy rates, their chosen features and models involved trade-offs in terms of complexity.

Table IV.17. AAP results comparison against previous studies

Authors	*Classification output*	*Input features*	*Related pathologies*	*Classifier*	*Accuracy*
Putra et al. [19]	*Healthy vs. CHD*	*Frequency band features and statistical features*	*• Coronary Heart Disease*	*KNN*	*90.9%*
Hackstein et al. [18]	*Control Group vs. Aneurysms*	*Parameter estimation of ARMAX models and frequency response features*	*• Aneurysms*	*KNN*	*60%*
Hosseini et al. [20]	*High Risk CAD vs. Low Risk CAD*	*Statistical, time-interval and time-domain features*	*• Coronary Artery Disease*	*KNN*	*81.5%*
De Moraes et al. [21]	*Cardiopathies vs. Healthy*	*Time domain and statistical features*	*• Idiopathic Dilated Cardiomyopathy • Chagas Cardiomyopathy • Ischemic Cardiomyopathy*	*KNN MLP K-means SOM*	*88.57-100% 90-100% 91.85-100% 87.5-100%*
Divya et al. [24]	*Cardiac-risk level 1 vs. Cardiac- risk level 2 vs. Respiratory disorder vs. Normal*	*Statistical features, DWT coefficients, dimensionally reduced features via SVD*	*• Risk assessment*	*GMM SDC*	*96.64 97.88%*
Prabhakar et al. [23]	*CVD-risk vs. Normal*	*Dimensionally reduced features via metaheuristic optimization algorithms*	*• Risk assessment*	*LR SVM NB ANN*	*99.48% 98.96% 98.96% 98.96%*
Palanisamy and Rajaguru [22]	*CVD-risk vs. Normal*	*Dimensionally reduced features via heuristic- and transformation-based techniques*	*• Risk assessment*	*HS*	*98.31%*
Tjahjadi et al. [36]	*Hypertension vs. Pre-hypertension vs. Normotension*	*Time-Frequency analysis*	*• Hypertension*	*BLSTM*	*93%*
Tjahjadi and Ramli. [167]	*Hypertension vs. Pre-hypertension vs. Normotension*	*2100 PPG samples*	*• Hypertension*	*KNN*	*93%*
This study	*9 AAPs vs. Normal vs. Unidentified*	*Time-domain & morphological features*	*• Hypertrophic obstructive cardiomyopathy • Aortic stenosis • Aortic regurgitation • Mixt valvular diseases*	*KNN BT*	*90.9% 91%*

	• *Pulmonary embolism* • *Constrictive pericarditis* • *Pericardial tamponade* • *Cardiomyopathies* • *Arteriovenous fistula* • *Sepsis* • *Anemia* • *Thyrotoxicosis* • *Severe bradycardia*

For instance, the heuristic and transformational feature extraction approaches employed in [18, 19, 22-24, 36] yielded abstract representations that could prove challenging to rationalize within a clinical context. Algorithms such as swarm intelligence [23] and transformations [22,24] frequently entail intricate mathematical operations or optimization techniques. Furthermore, classifiers like SVM, ANN, GMM, and BLSTM may undermine modular simplicity, due to their complex internal structure. Although LR and NB models created in [23] offer interpretability through their parametric nature, dimensionally reduced features introduce instance-level trade-offs.

The present work used physiological input parameters obtained from time duration, slope and SCs, all together defining pulse wave characteristics. This resulted in 24 predictors, a reasonable feature subset when considering the number of classes involved. In terms of modular design, the KNN model was developed using simpler hyperparameters, requiring a single neighbor for multi-target classification. However, depending solely on the closest data point may lead to erratic predictions if the neighbor is an outlier. In contrast, employing 200 DT learners for the BT model undermines its simplicity despite encompassing interpretable individual models. A performance focused tuning process may thus compromise simplicity.

5. Opportunities and Challenges for Healthcare Integration

5.1. Clinical Perspectives and Considerations

The proposed AAP classification framework shows promise as a cost-effective adjunctive tool in clinical settings by facilitating the discrimination between specific pulse abnormalities and their potential underlying etiologies. For example, the identification of AAP waveforms such as pulsus tardus, pulsus parvus et tardus, bisferiens pulse, and water hammer pulse could aid in the detection of various valvular defects (VHDs) [61, 68, 223]. Likewise, the appearance of a dicrotic pulse may indicate conditions associated with low CO [65, 228]. Meanwhile, a

deep pulse profile could be indicative of sepsis or reduced peripheral resistance [59, 66]. Furthermore, pathologies typically connected with a bounding pulse or shallow HAP include anemia, thyrotoxicosis, severe bradycardia, arteriovenous fistula, or AR [28].

While AAPs have historically been connected to specific cardiovascular conditions [27, 29, 65, 206, 207, 217], there remain no standardized hemodynamic criteria for categorizing their waveform patterns. Clinicians tend to utilize AAP terminology only when an association with particular CVDs exists. For instance, terms such as anacrotic, pulsus tardus, and pulsus parvus et tardus are often employed in the analysis of AS waveforms [29, 223]. Similarly, descriptors like bisferiens, water hammer, and bounding are commonly applied when examining AR tracings [68, 216]. Furthermore, despite the radial artery being considered the gold standard site for acquiring ABP signals, literature addressing the normal hemodynamic characteristics defining the radial pulse morphology is scarce. Currently, the evaluation methods involve either visual examination of pulse waveforms or palpation of an artery [28].

Given these limitations, we aimed to develop a modeling approach for identifying AAP patterns based on three analytic approaches. Contour analysis incorporated criteria, theories, and descriptions from previous studies examining AAP morphologies to determine suitable contour parameters. Amplitude and temporal analyses synthesized metrics and criteria from studies of pathologies exhibiting specific morphologies to derive time and amplitude parameters. Together, these three analytic components sought to objectively characterize AAP patterns through consideration of morphological descriptions, hemodynamic indicators, and pathological evidence, with the goal of generating parameterized AAP models.

Associating arterial pressure waveform morphologies with cardiovascular conditions based on established hemodynamic mechanisms could bolster clinician confidence in assessments compared to approaches lacking underlying causal relationships. Integrating such a system into wearable biosensing devices [84] may enable several potential benefits:

(1) Clinical decision support: Direct physician involvement could be triggered if cardiovascular condition is suspected, allowing non-invasive verification of abnormalities and review of pathologies commonly linked to a patient's morphological profile.

(2) Post-operative monitoring: Remote surveillance of postoperative patients dismissed from the clinic via an integrated patient portal in the EHR system may aid recovery oversight and early intervention for emerging issues.

(3) Nursing alerts: Automated notifications of any detected aberrations in a patient's pulse wave patterns (AAPs) could support nursing staff.

(4) Timely communication: Concerning patterns may prompt alerts to patients and clinicians to enable prompt response if warranted.

However, a successful clinical adoption relies on addressing some challenges:

(1) Motion artifact sensitivity: PPG susceptibility to motion artifacts [38] poses a challenge. Automatic identification and removal of corrupted signals using techniques like signal quality indexing (SSQI) can help mitigate motion interference [229], but excessive rejection may limit system usability. Strategies like customizable reminders to notify users/clinicians prompting reduced movement during screening or strategic sensor placement at less prone sites, such as the chest, could also be explored as it is less impacted by movement. Strategies like customizable reminders to notify users/clinicians prompting reduced movement during screening or strategic sensor placement at less prone sites, e.g. chest, could also be explored as it is less impacted by movement.

(2) Model updates: Continuous clinically annotated arterial pressure data collection is necessary to refine the model overtime. However, guidelines and dedicated collection programs are currently lacking. Raising awareness among biomedical engineers to facilitate collaborations with clinics may support data collection initiatives. Beyond clinics, smartwatch/fitness tracker integration may enhance global health awareness.

(3) Clinical transparency: Gaining physician and patient trust necessitates model explainability [37]. Interactive interfaces visualizing predicted patient pulse patterns linked to accompanying hemodynamic animations could illustrate prediction logic. Further, adjusting inputs in "what if" scenario simulations where feature values are manipulated to observe risk/disease probability changes may elucidate model grounding in medical evidence via transparent visualization and simulation approaches. Together, such explainability features foster understanding and confidence in predictions through transparency.

5.2. Consumer-Oriented Deployment

PPG allows for a non-invasive and convenient means of measuring pulsatile blood volume changes via its periodic waveform, which provides insights into cardiovascular health status [118]. However, extracting meaningful features from PPG signals proves challenging due to their non-stationary nature, as the statistical properties fluctuate dynamically over time. To

address this, FSST was employed to decompose the signals into the time-frequency domain, generating high-resolution TFRs that revealed transient cardiovascular variabilities related to BP regulation. These TFRs were then subjected to statistical and metaheuristic optimization techniques to engineer features capturing pressure-dependent changes not delineated by basic approaches. This optimized set of time-frequency domain signal characteristics constituted the input parameterization for the BP classification model. It furnished a robust representation of the non-stationary signal dynamics within the PPG data that considers its time-varying properties. In essence, this signal processing and feature engineering methodology aimed to develop an input characterization capable of handling the non-stationary nature of PPG signals for BP prediction applications.

For the classification task, an ensemble methodology was implemented utilizing 200 BT-learners to improve accuracy and robustness over solitary models by minimizing variance [195]. Bagging provides an efficient means of leveraging extensive training datasets as the constituent models can be fitted in parallel on data subsets. Specifically, the model was trained on a sizable dataset encompassing diverse BP ranges [198]. This variety aimed to foster generalizability to real-world settings and reduce biases relative to models trained on a narrow BP distribution. The low computational complexity enabled training completion within only minutes per experiment on a dataset of this scale. Moreover, testing on a balanced dataset enables better evaluation of performance across the full spectrum of population subgroups. The ensemble approach aimed to develop a model capable of handling variability in both training data composition and target variable distributions for BP classification in practical applications.

The proposed approach holds promise as an affordable aid in clinical settings, as the experimental models achieved F1 scores ranging from 96.6% to 99.1% for classifications of non-HT vs. HT, NT vs. HT, and NT vs. PHT. Such trials play an important role in routine prehypertension and hypertension detection, which in turn contribute to early diagnosis and management of hypertension [104]. Additionally, these results validate the employment of the proposed system in real-world scenarios where various sources of perturbation could interfere, owing to the synchrosqueezing transform's stability in handling signals contaminated with artifacts [184]. This level of robustness is reasonable given that the PPG signals were captured from patients in intensive care unit wards [55], environments prone to introducing noise into physiological recordings.

This approach utilizing BT offers several advantages for BP monitoring via wearable devices compared DNN-based systems:

(1) Convenient implementation: As the approach only requires raw PPG inputs, it provides a convenient way for implementation in wearable devices. The BT models can be deployed locally on the wearable device without the need for cloud computing resources.

(2) Low computational and storage demands: BT methods are well-suited for wearables due to their lower computational complexity and storage requirements compared to DNNs. This allows housing the full model on-device, avoiding the latency, costs, and privacy issues associated with cloud-based solutions. In contrast, deep networks require vast storage that is better suited to cloud-based deployment.

(3) Efficient prediction: BT models can make predictions efficiently using typical processors without the need for specialized GPUs, which helps to lower the overall costs of the wearable device. Deep networks, on the other hand, require powerful GPU processing, which is often infeasible for affordable wearables.

(4) Adaptability to continuous learning: BT models are adaptable to incremental, continuous learning through regularly updating the on-device ensemble as additional training data becomes available. This is in contrast to deep networks, where retraining to update the weights is much more computationally expensive, making regular updates on wearables impractical.

This approach could make BP monitoring more affordable and accessible by allowing it to be done directly through popular wearable devices, rather than relying on expensive medical equipment. The lightweight system is simple enough to use that people could monitor their BP anywhere, even in areas with limited resources. This helps address a common problem - many individuals don't actually know what BP levels are considered normal or concerning. Currently, people usually only find out during occasional doctor visits.

If more widely applied, this method may enhance early detection and management of high BP. It could also lead to better outcomes by preventing damage to organs over time from uncontrolled hypertension. With more widespread monitoring, higher risk cases could be identified sooner. Then, lifestyle changes or treatment could be started earlier to better control the condition. All of this may help reduce healthcare costs associated with complications later on.

By facilitating convenient BP self-tracking using wearable technologies, this approach aims to improve global health by making monitoring more accessible. It seeks to fill gaps and overcome barriers related to screening and management of hypertension. The goal is to eventually help more individuals maintain normal BP and avoid issues through increased awareness and monitoring opportunities.

Conclusions

Summarizing Contributions, Limitations, and Future Directions

This thesis introduced a non-invasive arterial pressure classification framework optimized for the purpose of predicting AAPs, classifying hypertension status, and distinguishing between discrete BP intervals, all solely from PPG signal data. The AAP classifiers were modelled with the aim of addressing existing gaps in the literature pertaining to cardiovascular disease classification for effective clinical translation, as their evidence-based classifications provide clinically-relevant insights that can directly inform diagnostic formulation. In contrast to prior investigations, the proposed AAP methodology presents an approach that is more amenable to integration within clinical practice settings due its ability to classify multiple conditions while maintaining direct links between predictions and potential cardiovascular implications. This addresses limitation of previous research focused only on broad risk profiling or narrow disease taxonomies. The hypertension classifiers adopt a divergent research orientation aligned with the intended objective of facilitating widespread public access to monitoring via integration within wearable PPG devices. Given hypertension's asymptomatic nature and high prevalence rates, this goal aims to enable expanded global monitoring opportunities to enhance prevention through raised individual awareness. The BP interval classifiers are designed to predict discrete ranges for systolic, diastolic and mean arterial pressures, delineated at 5mmHg thresholds, with the intention of enabling ML model training within well-defined physiological boundaries while deliberately controlling for prediction error. Reporting outputs as constrained BP categorizations in this manner permits constrained BP estimation.

The dataset utilized in this thesis was sourced from the MIMIC-III database, as it contains over 3 million hours of simultaneously recorded ABP and PPG signals from thousands of ICU patients. Thousands of subject recordings were extracted from this extensive clinical dataset. AAPs were initially identified from ABP records by referencing known pathophysiological exemplars understood to manifest such anomalies, resulting in 9 models. BP levels were deduced from ABP signals according to clinical guidelines established by the JNC7, conceptualizing 3 categorical groups including HT, PHT, and NT. Systolic (SBP), diastolic (DBP) and mean arterial pressure (MAP) intervals were discretized into 5mmHg ranges, yielding 16 categorical classes for SBP and MAP while DBP encompassed 12 classes. A key methodological aspect of this work involved optimizing classifier parameters to better analyze the aforementioned arterial pressure waveforms and characteristics. However, differentiating intended system end-users, whether clinical decision support tools or individual self-screening applications, was indispensable for parameterizing models concordant with targeted deployment contexts. Hence, classifiers were carefully selected and tailored through targeted

optimization of parameters according to the usability requirements of each environment. This specialized modeling design addressed barriers that have hindered prior efforts from successfully translating into real-world clinical or consumer-focused applications.

From a clinical perspective, BT and KNN classifiers were selected for AAP classification to accommodate PPG nonlinear characteristics while maintaining a simply algorithmic structure, as less complex models tend to be more readily explainable and interpretable compared to sophisticated models like DNNs. By design, BT and KNN inherently favor interpretability due to decision trees' logical architecture and KNN's statistical basis. Several ML algorithms were evaluated to validate BT and KNN's utility, demonstrating superior AAP classification performance. The classifiers were optimized using both internal and external techniques. Internal optimization focused on hyperparameter fine-tuning via Bayesian optimization to identify optimal configurations. In contrast, external optimization aimed to enhance input parameters by extracting 44 physiological metrics from PPG signals, reducing these to the top 6 most salient features according to MRMR analysis. The models successfully discriminated AAP classes with over 90% accuracy. However, internal tuning resulted in BT employing 200 learners, compromising its simplicity advantage, while KNN's reliance on a single neighbor risks random outlier prediction due to sensitivity to abnormal data points.

For consumer-oriented applications, considerations for designing an affordable blood pressure monitoring system were paramount. DNNs' requirement for powerful GPUs to rapidly compute their computationally intensive layers introduces deployment barriers, especially when handling large datasets. This rendered ML classifiers a preferable candidate for engineering a cost-effective solution due to their lightweight hyperparameters. In particular, the BT classifier was evaluated for BP prediction tasks, categorizing measurements into ranges as well as levels including HT, PHT, and NT. Mirroring optimizations employed for clinical systems, the BT model was refined internally following Bayesian optimization procedures. Meanwhile, input parameters were derived from PPG signals' synchrosqueezing transform utilizing statistical analysis and cuckoo search optimization. Results demonstrated impressive performance with over 95% accuracy classifying hypertension status and over 90% accuracy classifying BP ranges. The lighter resource requirements of ML classifiers relative to DNNs addressed feasibility challenges for designing an affordable, scalable consumer BP monitoring system. Performance validation established proof-of-concept for leveraging these algorithms in real-world wearable applications.

While the developed models demonstrated potential utility for arterial pressure prediction, overfitting challenges necessitated refinement. Accordingly, FRV was applied to enhance model testing accuracies. FRV successfully improved test set accuracy across classifiers by augmenting feature space redundancy. Although FRV proved an efficient approach, its capabilities were limited due to low redundancy levels. To more fully leverage FRV's potential, it is hypothesized that higher redundancy levels above 50% would yield additional benefits. While initial experiments validated FRV efficacy, addressing overfitting necessitates further exploration of enhancing redundancy. Pushing redundancy beyond previous thresholds may strengthen model generalization, an ongoing priority as predictive performance and robustness are balanced through continued algorithm development and validation.

A core strength of this study was leveraging novel trough and dicrotic notch detection tools, essential for extracting PPG features and modeling AAPs. However, to strengthen the reliability of findings, further analysis is needed to define more coherent parameters optimized for higher sampling frequency signals. Additionally, PPG signals' sensitivity to motion artifacts may negatively impact algorithm accuracy. The dicrotic notch detector may also struggle with pulse waves exhibiting multiple systolic peaks. While increasing evaluation process iterations could address this issue, over-minimization may also result. To build upon initial work, future efforts should explore parameter refinement suited to varying sampling rates. Addressing motion artifact impacts through hardware/software solutions could enhance reliability.

In BP classification systems, the methodology demonstrates potential as an accessible, affordable self-screening tool to enable early hypertension detection through consumer wearables. By facilitating convenient BP monitoring ubiquitously, this approach may help optimize health outcomes worldwide through personalized notifications and hypertension management afforded by timely data. Further research should focus on evaluating real-world predictive performance across diverse populations and age demographics to strengthen generalizability insights. With refinements to enhance robustness, this technique could empower both patients and providers by furnishing convenient means for early hypertension detection and mitigation of otherwise asymptomatic cardiovascular risks. Validating predictive capabilities on out-of-sample cohorts, and assessing model recalibration over time, will be important next steps to clarify translational viability. If predictive accuracy can be sustained longitudinally across demography, wearable-enabled BP classification may represent a promising avenue for scalable prevention through low-cost continuous screening and tracking aligned with on-the-go lifestyles.

The AAP classification system also shows promise as a practical, cost-effective diagnostic tool. Its ability to detect and link abnormalities to specific CVDs enables more informed care planning relative to generic risk profiling. This offers potential value in early detection and prevention through integration into wearables. Possible applications include clinical decision support via disease verification, remote postoperative monitoring via electronic health records, nursing alerts for anomalies, and timely notifications. However, successful clinical adoption depends on addressing challenges such as motion artifact susceptibility through signal quality indexing techniques like SSQI. Continuous collection of clinically annotated data is also important for model refinement, though guidelines currently lack dedicated programs. Raising awareness among biomedical engineers could facilitate data partnerships with clinical sites. Ensuring predictive explanations through interactive tools linking patterns to disease animations and allowing adjustments to visualize predicted changes helps establish trust by conveying prediction logic. Addressing technical and adoption barriers will be crucial to realizing this system's potential across various healthcare uses. Ongoing efforts refining techniques, collaborating on data acquisition protocols, and strengthening model transparency will determine translational viability.

This study contributes promising advancements to the field of arterial blood pressure prediction. However, further research is needed to validate the results using larger and more diverse datasets, as well as potentially extending the approach to integrate other physiological signals and health conditions. Future work could include the collection of multi-site PPG datasets recorded at different body locations to uncover novel morphological features. Synchronizing higher sampling rate PPG with additional signals, such as ECG, may enhance the cardiovascular representation. Classifying pulse morphologies from central or proximal arterial sites may reveal patterns that are indistinct in distal recordings. The approach also shows potential for detecting various health conditions through advanced pressure wave analyses. For example, renal artery stenosis could be assessed by comparing upstream and downstream wave differences, while vascular dementia may be detected through analyzing the long-term consequences of chronic hypertension. Focusing on acquiring more reliable pulse characterization metrics could assist in the modeling of AAP patterns. Advancing the integration of diverse datasets, signals, and health contexts will deepen the understanding and broaden the applications of arterial pulse prediction in clinical management. Conducting larger validation studies across diverse populations remains important to substantiate the initial findings and spur the translation of this research into practical applications.

References

[1] "Cardiovascular diseases (CVDs)," World Health Organization. Accessed: Apr. 15, 2023. [Online]. Available: https://www.who.int/news-room/fact-sheets/detail/cardiovascular-diseases-(cvds)

[2] M. Jafari *et al.*, "Automated diagnosis of cardiovascular diseases from cardiac magnetic resonance imaging using deep learning models: A review," *Computers in Biology and Medicine*, vol. 160, p. 106998, Jun. 2023, doi: 10.1016/j.compbiomed.2023.106998.

[3] D. P. Zipes and H. J. J. Wellens, "Sudden Cardiac Death," *Circulation*, vol. 98, no. 21, pp. 2334–2351, Nov. 1998, doi: 10.1161/01.CIR.98.21.2334.

[4] K. V. V. Reddy, I. Elamvazuthi, A. A. Aziz, S. Paramasivam, H. N. Chua, and S. Pranavanand, "Heart Disease Risk Prediction Using Machine Learning Classifiers with Attribute Evaluators," *Applied Sciences*, vol. 11, no. 18, p. 8352, Sep. 2021, doi: 10.3390/app11188352.

[5] P. K. Sinha, E. S. Sinha, and J. Kaur, "Biomarkers of Cardiac Health and Disease," *Crit Rev Biomed Eng*, vol. 47, no. 5, pp. 395–407, 2019, doi: 10.1615/CritRevBiomedEng.2019031097.

[6] A. S. Maisel *et al.*, "Timing of Immunoreactive B-Type Natriuretic Peptide Levels and Treatment Delay in Acute Decompensated Heart Failure," *Journal of the American College of Cardiology*, vol. 52, no. 7, pp. 534–540, Aug. 2008, doi: 10.1016/j.jacc.2008.05.010.

[7] T. S. Polonsky and P. Greenland, "CVD screening in low-risk, asymptomatic adults: clinical trials needed," *Nat Rev Cardiol*, vol. 9, no. 10, pp. 599–604, Oct. 2012, doi: 10.1038/nrcardio.2012.114.

[8] M. A. Naser, A. A. Majeed, M. Alsabah, T. R. Al-Shaikhli, and K. M. Kaky, "A Review of Machine Learning's Role in Cardiovascular Disease Prediction: Recent Advances and Future Challenges," *Algorithms*, vol. 17, no. 2, p. 78, Feb. 2024, doi: 10.3390/a17020078.

[9] J. Xu, X. Xi, J. Chen, V. S. Sheng, J. Ma, and Z. Cui, "A Survey of Deep Learning for Electronic Health Records," *Applied Sciences*, vol. 12, no. 22, p. 11709, Nov. 2022, doi: 10.3390/app122211709.

[10] G. Varoquaux and V. Cheplygina, "Machine learning for medical imaging: methodological failures and recommendations for the future," *npj Digit. Med.*, vol. 5, no. 1, p. 48, Apr. 2022, doi: 10.1038/s41746-022-00592-y.

[11] N. Rabbani, G. Y. E. Kim, C. J. Suarez, and J. H. Chen, "Applications of machine learning in routine laboratory medicine: Current state and future directions," *Clinical Biochemistry*, vol. 103, pp. 1–7, May 2022, doi: 10.1016/j.clinbiochem.2022.02.011.

[12] S. Dubey, G. Tiwari, S. Singh, S. Goldberg, and E. Pinsky, “Using machine learning for healthcare treatment planning,” *Front. Artif. Intell.*, vol. 6, p. 1124182, Apr. 2023, doi: 10.3389/frai.2023.1124182.

[13] F. Cui, Y. Yue, Y. Zhang, Z. Zhang, and H. S. Zhou, “Advancing Biosensors with Machine Learning,” *ACS Sens.*, vol. 5, no. 11, pp. 3346–3364, Nov. 2020, doi: 10.1021/acssensors.0c01424.

[14] M. Barash, D. McNevin, V. Fedorenko, and P. Giverts, “Machine learning applications in forensic DNA profiling: A critical review,” *Forensic Science International: Genetics*, vol. 69, p. 102994, Mar. 2024, doi: 10.1016/j.fsigen.2023.102994.

[15] O. A. Victor, Y. Chen, and X. Ding, “Non-Invasive Heart Failure Evaluation Using Machine Learning Algorithms,” *Sensors*, vol. 24, no. 7, p. 2248, Mar. 2024, doi: 10.3390/s24072248.

[16] A. Chakraborty, D. Sadhukhan, S. Pal, and M. Mitra, “Automated myocardial infarction identification based on interbeat variability analysis of the photoplethysmographic data,” *Biomedical Signal Processing and Control*, vol. 57, p. 101747, Mar. 2020, doi: 10.1016/j.bspc.2019.101747.

[17] Q. Qananwah, M. Ababneh, and A. Dagamseh, “Cardiac arrhythmias classification using photoplethysmography database,” *Sci Rep*, vol. 14, no. 1, p. 3355, Feb. 2024, doi: 10.1038/s41598-024-53142-9.

[18] U. Hackstein *et al.*, “Early diagnosis of aortic aneurysms based on the classification of transfer function parameters estimated from two photoplethysmographic signals,” *Informatics in Medicine Unlocked*, vol. 25, p. 100652, 2021, doi: 10.1016/j.imu.2021.100652.

[19] F. A. Putra, S. Mandala, and M. Pramudyo, “A Study of Feature Selection Method to Detect Coronary Heart Disease (CHD) on Photoplethysmography (PPG) Signals,” *bits*, vol. 4, no. 2, Sep. 2022, doi: 10.47065/bits.v4i2.2259.

[20] Z. S. Hosseini, E. Zahedi, H. Movahedian Attar, H. Fakhrzadeh, and M. H. Parsafar, “Discrimination between different degrees of coronary artery disease using time-domain features of the finger photoplethysmogram in response to reactive hyperemia,” *Biomedical Signal Processing and Control*, vol. 18, pp. 282–292, Apr. 2015, doi: 10.1016/j.bspc.2014.12.011.

[21] J. L. De Moraes, T. L. De Oliveira, M. X. Rocha, G. G. Vasconcelos, and A. R. De Alexandria, “Stratification of cardiopathies using photoplethysmographic signals,” *Informatics in Medicine Unlocked*, vol. 20, p. 100417, 2020, doi: 10.1016/j.imu.2020.100417.

[22] S. Palanisamy and H. Rajaguru, “Machine Learning Techniques for the Performance Enhancement of Multiple Classifiers in the Detection of Cardiovascular Disease from PPG Signals,” *Bioengineering*, vol. 10, no. 6, p. 678, Jun. 2023, doi: 10.3390/bioengineering10060678.

[23] S. K. Prabhakar, H. Rajaguru, and S.-W. Lee, “Metaheuristic-Based Dimensionality Reduction and Classification Analysis of PPG Signals for Interpreting Cardiovascular Disease,” *IEEE Access*, vol. 7, pp. 165181–165206, 2019, doi: 10.1109/ACCESS.2019.2950220.

[24] D. Ramachandran, V. Ponnusamy Thangapandian, and H. Rajaguru, “Computerized approach for cardiovascular risk level detection using photoplethysmography signals,” *Measurement*, vol. 150, p. 107048, Jan. 2020, doi: 10.1016/j.measurement.2019.107048.

[25] W. Karlen, M. Turner, E. Cooke, G. Dumont, and J. M. Ansermino, “CapnoBase: Signal database and tools to collect, share and annotate respiratory signals,” 2010, doi: 10.3929/ETHZ-B-000087887.

[26] M. M. Hamza, B. Noreddine, B. Z. Abdeslem, Y. Benyssaad, and B. S. Ilham, “Classifying Abnormal Arterial Pulse Patterns in Cardiovascular Diseases: A Photoplethysmography and Machine Learning Approach,” *TS*, vol. 41, no. 2, Apr. 2024, doi: 10.18280/ts.410201.

[27] R. C. Schlant and J. M. Felner, “The arterial pulse— clinical manifestations,” *Current Problems in Cardiology*, vol. 2, no. 5, pp. 1–50, Aug. 1977, doi: 10.1016/0146-2806(77)90013-5.

[28] J. Maddury, “Arterial Pulse,” *Ind J Car Dis Wom*, vol. 02, no. 04, pp. 099–110, Dec. 2017, doi: 10.1055/s-0038-1636691.

[29] P. Wood, “Aortic stenosis∗,” *The American Journal of Cardiology*, vol. 1, no. 5, pp. 553–571, May 1958, doi: 10.1016/0002-9149(58)90138-3.

[30] World Health Organization, “Hypertension,” World Health Organization. [Online]. Available: https://www.who.int/news-room/fact-sheets/detail/hypertension

[31] World Health Organization, “A global brief on hypertension : silent killer, global public health crisis: World Health Day 2013,” World Health Organization. [Online]. Available: https://apps.who.int/iris/handle/10665/79059

[32] G. Martínez, N. Howard, D. Abbott, K. Lim, R. Ward, and M. Elgendi, “Can Photoplethysmography Replace Arterial Blood Pressure in the Assessment of Blood Pressure?,” *JCM*, vol. 7, no. 10, p. 316, Sep. 2018, doi: 10.3390/jcm7100316.

[33] T. Tamura, Y. Maeda, M. Sekine, and M. Yoshida, “Wearable Photoplethysmographic Sensors—Past and Present,” *Electronics*, vol. 3, no. 2, pp. 282–302, Apr. 2014, doi: 10.3390/electronics3020282.

[34] B. Alexander, M. Cannesson, and T. J. Quill, “Blood Pressure Monitoring,” in *Anesthesia equipment: principles and applications*, Second edition., J. Ehrenwerth, J. B. Eisenkraft, and J. M. Berry, Eds., Philadelphia, PA: Saunders, 2013, pp. 273–282.

[35] L. Wang, W. Zhou, Y. Xing, and X. Zhou, “A Novel Neural Network Model for Blood Pressure Estimation Using Photoplethesmography without Electrocardiogram,” *Journal of Healthcare Engineering*, vol. 2018, pp. 1–9, 2018, doi: 10.1155/2018/7804243.

[36] H. Tjahjadi, K. Ramli, and H. Murfi, “Noninvasive Classification of Blood Pressure Based on Photoplethysmography Signals Using Bidirectional Long Short-Term Memory and Time-Frequency Analysis,” *IEEE Access*, vol. 8, pp. 20735–20748, 2020, doi: 10.1109/ACCESS.2020.2968967.

[37] A. I. F. Poon and J. J. Y. Sung, “Opening the black box of AI-Medicine,” *J of Gastro and Hepatol*, vol. 36, no. 3, pp. 581–584, Mar. 2021, doi: 10.1111/jgh.15384.

[38] D. Seok, S. Lee, M. Kim, J. Cho, and C. Kim, “Motion Artifact Removal Techniques for Wearable EEG and PPG Sensor Systems,” *Front.Electron.*, vol. 2, p. 685513, May 2021, doi: 10.3389/felec.2021.685513.

[39] J. G. A. Barbedo, “Impact of dataset size and variety on the effectiveness of deep learning and transfer learning for plant disease classification,” *Computers and Electronics in Agriculture*, vol. 153, pp. 46–53, Oct. 2018, doi: 10.1016/j.compag.2018.08.013.

[40] K. Y. Chan *et al.*, “Deep neural networks in the cloud: Review, applications, challenges and research directions,” *Neurocomputing*, vol. 545, p. 126327, Aug. 2023, doi: 10.1016/j.neucom.2023.126327.

[41] E. Brochu, V. M. Cora, and N. de Freitas, “A Tutorial on Bayesian Optimization of Expensive Cost Functions, with Application to Active User Modeling and Hierarchical Reinforcement Learning.” arXiv, 2010. doi: 10.48550/ARXIV.1012.2599.

[42] D. R. Jones, “A taxonomy of global optimization methods based on response surfaces,” *Journal of Global Optimization*, vol. 21, no. 4, pp. 345–383, 2001, doi: 10.1023/A:1012771025575.

[43] M. M. Madani and E. Golts, “Cardiovascular Anatomy,” in *Reference Module in Biomedical Sciences*, Elsevier, 2014, p. B9780128012383001963. doi: 10.1016/B978-0-12-801238-3.00196-3.

[44] A. D. Padsalgikar, “Cardiovascular System: Structure, Assessment, and Diseases,” in *Plastics in Medical Devices for Cardiovascular Applications*, Elsevier, 2017, pp. 103–132. doi: 10.1016/B978-0-323-35885-9.00005-9.

[45] R. Moreau *et al.*, “Blood metabolomics uncovers inflammation-associated mitochondrial dysfunction as a potential mechanism underlying ACLF,” *Journal of Hepatology*, vol. 72, no. 4, pp. 688–701, Apr. 2020, doi: 10.1016/j.jhep.2019.11.009.

[46] I. Peate, “The heart: an amazing organ,” *British Journal of Healthcare Assistants*, vol. 15, no. 2, pp. 72–77, Mar. 2021, doi: 10.12968/bjha.2021.15.2.72.

[47] M. T. Keating and M. C. Sanguinetti, “Molecular and Cellular Mechanisms of Cardiac Arrhythmias,” *Cell*, vol. 104, no. 4, pp. 569–580, Feb. 2001, doi: 10.1016/S0092-8674(01)00243-4.

[48] H. Fukuta and W. C. Little, “The Cardiac Cycle and the Physiologic Basis of Left Ventricular Contraction, Ejection, Relaxation, and Filling,” *Heart Failure Clinics*, vol. 4, no. 1, pp. 1–11, Jan. 2008, doi: 10.1016/j.hfc.2007.10.004.

[49] J. King and D. R. Lowery, “Physiology, Cardiac Output,” in *StatPearls*, Treasure Island (FL): StatPearls Publishing, 2024. Accessed: Jun. 04, 2024. [Online]. Available: http://www.ncbi.nlm.nih.gov/books/NBK470455/

[50] J. O. Wedin *et al.*, “Patients With Bicuspid Aortic Stenosis Demonstrate Adverse Left Ventricular Remodeling and Impaired Cardiac Function Before Surgery With Increased Risk of Postoperative Heart Failure,” *Circulation*, vol. 146, no. 17, pp. 1310–1322, Oct. 2022, doi: 10.1161/CIRCULATIONAHA.122.060125.

[51] I. Stadiotti *et al.*, “Pressure Overload Activates DNA-Damage Response in Cardiac Stromal Cells: A Novel Mechanism Behind Heart Failure With Preserved Ejection Fraction?,” *Front. Cardiovasc. Med.*, vol. 9, p. 878268, Jun. 2022, doi: 10.3389/fcvm.2022.878268.

[52] H. Antoni, “Electrical Properties of the Heart,” in *Applied Bioelectricity*, New York, NY: Springer New York, 1998, pp. 148–193. doi: 10.1007/978-1-4612-1664-3_5.

[53] D. Corrado, A. Biffi, C. Basso, A. Pelliccia, and G. Thiene, “12-lead ECG in the athlete: physiological versus pathological abnormalities,” *Br J Sports Med*, vol. 43, no. 9, pp. 669–676, Sep. 2009, doi: 10.1136/bjsm.2008.054759.

[54] G. Youssef *et al.*, “Familial history of hypertension as a predictor of increased arterial stiffness in normotensive offspring,” *The Egyptian Heart Journal*, vol. 69, no. 1, pp. 37–44, Mar. 2017, doi: 10.1016/j.ehj.2016.07.003.

[55] S. H. Johnsen, S. H. Forsdahl, K. Singh, and B. K. Jacobsen, “Atherosclerosis in Abdominal Aortic Aneurysms: A Causal Event or a Process Running in Parallel? The Tromsø Study,” *ATVB*, vol. 30, no. 6, pp. 1263–1268, Jun. 2010, doi: 10.1161/ATVBAHA.110.203588.

[56] N. F. Kassell, T. Sasaki, A. R. Colohan, and G. Nazar, “Cerebral vasospasm following aneurysmal subarachnoid hemorrhage.,” *Stroke*, vol. 16, no. 4, pp. 562–572, Jul. 1985, doi: 10.1161/01.STR.16.4.562.

[57] P. Salvi, “Vascular Hemodynamics and Blood Pressure,” in *Pulse Waves*, Cham: Springer International Publishing, 2017, pp. 1–17. doi: 10.1007/978-3-319-40501-8_1.

[58] K. J. Liu *et al.*, “Lithium phthalocyanine: a probe for electron paramagnetic resonance oximetry in viable biological systems.,” *Proc. Natl. Acad. Sci. U.S.A.*, vol. 90, no. 12, pp. 5438–5442, Jun. 1993, doi: 10.1073/pnas.90.12.5438.

[59] D. Chambers, C. Huang, and G. Matthews, *Basic Physiology for Anaesthetists*, 2nd ed. Cambridge University Press, 2019. doi: 10.1017/9781108565011.

[60] M. R. Nelson, J. Stepanek, M. Cevette, M. Covalciuc, R. T. Hurst, and A. J. Tajik, “Noninvasive Measurement of Central Vascular Pressures With Arterial Tonometry: Clinical Revival of the Pulse Pressure Waveform?,” *Mayo Clinic Proceedings*, vol. 85, no. 5, pp. 460–472, May 2010, doi: 10.4065/mcp.2009.0336.

[61] I. Moxham, “Understanding Arterial Pressure Waveforms,” *Southern African Journal of Anaesthesia and Analgesia*, vol. 9, no. 1, pp. 40–42, Feb. 2003, doi: 10.1080/22201173.2003.10872991.

[62] James. Merritt and Christine. Abshire, Eds., “The Heart,” in *Textbook of physical diagnosis: history and examination*, 6th ed., Philadelphia, PA: Saunders/Elsevier, 2010, pp. 391–437.

[63] R. C. Orchard and E. Craige, “Dicrotic pulse after open heart surgery.,” *Circulation*, vol. 62, no. 5, pp. 1107–1114, Nov. 1980, doi: 10.1161/01.CIR.62.5.1107.

[64] G. A. Ewy, J. C. Rios, and F. I. Marcus, “The Dicrotic Arterial Pulse,” *Circulation*, vol. 39, no. 5, pp. 655–662, May 1969, doi: 10.1161/01.CIR.39.5.655.

[65] W. R. Meadows, R. A. Draur, and C. E. Osadjan, “Dicrotism in heart disease,” *American Heart Journal*, vol. 82, no. 5, pp. 596–608, Nov. 1971, doi: 10.1016/0002-8703(71)90328-0.

[66] A. Morelli *et al.*, “Systolic-dicrotic notch pressure difference can identify tachycardic patients with septic shock at risk of cardiovascular decompensation following pharmacological heart rate reduction,” *British Journal of Anaesthesia*, vol. 125, no. 6, pp. 1018–1024, Dec. 2020, doi: 10.1016/j.bja.2020.05.058.

[67] J. Constant, “Arterial Pulses and Pressures,” in *Essentials of bedside cardiology: with a complete course in heart sounds on CD*, 2nd ed., Totowa, N.J.: Humana Press, 2003, pp. 29–62.

[68] J. A. Chirinos, S. R. Akers, J. A. Vierendeels, and P. Segers, “A unified mechanism for the water hammer pulse and pulsus bisferiens in severe aortic regurgitation: Insights from wave intensity analysis,” *ARTRES*, vol. 21, no. C, p. 9, 2017, doi: 10.1016/j.artres.2017.12.002.

[69] J. Szocik, M. Teig, and K. K. Tremper, “ANESTHETIC MONITORING,” in *Basics of anesthesia*, Seventh edition., M. C. Pardo and R. D. Miller, Eds., Philadelphia: Elsevier, 2018, pp. 337–362.

[70] A. Murray *et al.*, “Variability in Blood Pressure Measurements from Recorded Auscultation Sounds,” presented at the 2019 Computing in Cardiology Conference, Dec. 2019. doi: 10.22489/CinC.2019.183.

[71] T. S. Schoot, M. Weenk, T. H. Van De Belt, L. J. Engelen, H. Van Goor, and S. J. Bredie, “A New Cuffless Device for Measuring Blood Pressure: A Real-Life Validation Study,” *J Med Internet Res*, vol. 18, no. 5, p. e85, May 2016, doi: 10.2196/jmir.5414.

[72] D. Nachman *et al.*, “Twenty-Four-Hour Ambulatory Blood Pressure Measurement Using a Novel Noninvasive, Cuffless, Wireless Device,” *American Journal of Hypertension*, p. hpab095, Jun. 2021, doi: 10.1093/ajh/hpab095.

[73] F. Pan *et al.*, “Development and validation of a deep learning-based automatic auscultatory blood pressure measurement method,” *Biomedical Signal Processing and Control*, vol. 68, p. 102742, Jul. 2021, doi: 10.1016/j.bspc.2021.102742.

[74] P. Muntner *et al.*, “Measurement of Blood Pressure in Humans: A Scientific Statement From the American Heart Association,” *Hypertension*, vol. 73, no. 5, May 2019, doi: 10.1161/HYP.0000000000000087.

[75] Department of Surgical Nursing, , Division of Nursing, Necmettin Erbakan University Faculty of Nursing, Konya, Turkey *et al.*, “The Effect of Cuff Size on Blood Pressure Measurement in Obese Surgical Patients: A Prospective Crossover Clinical Trial,” *FNJN*, vol. 28, no. 2, pp. 205–212, Sep. 2020, doi: 10.5152/FNJN.2020.19119.

[76] M. Sharma *et al.*, “Cuff-Less and Continuous Blood Pressure Monitoring: A Methodological Review,” *Technologies*, vol. 5, no. 2, p. 21, May 2017, doi: 10.3390/technologies5020021.

[77] J. Penäz, “Photoelectric measurement of blood pressure, volume and flow in the finger,” in *Digest of the 10th International Conference on Medical and Biological Engineering*, Dresden, 1973, p. 104.

[78] T. Athaya and S. Choi, “A Review of Noninvasive Methodologies to Estimate the Blood Pressure Waveform,” *Sensors*, vol. 22, no. 10, p. 3953, May 2022, doi: 10.3390/s22103953.

[79] M. Javaid, A. Haleem, R. Pratap Singh, R. Suman, and S. Rab, “Significance of machine learning in healthcare: Features, pillars and applications,” *International Journal of Intelligent Networks*, vol. 3, pp. 58–73, 2022, doi: 10.1016/j.ijin.2022.05.002.

[80] X. Ying, “An Overview of Overfitting and its Solutions,” *J. Phys.: Conf. Ser.*, vol. 1168, p. 022022, Feb. 2019, doi: 10.1088/1742-6596/1168/2/022022.

[81] H. K. Jabbar and R. Z. Khan, “Methods to Avoid Over-Fitting and Under-Fitting in Supervised Machine Learning (Comparative Study),” in *Computer Science, Communication and Instrumentation Devices*, Research Publishing Services, 2014, pp. 163–172. doi: 10.3850/978-981-09-5247-1_017.

[82] Department of Computer Science and Informatics, University of Energy and Natural Resources, Sunyani, Ghana, I. K. Nti, O. Nyarko-Boateng, and J. Aning, “Performance of Machine Learning Algorithms with

Different K Values in K-fold CrossValidation," *IJITCS*, vol. 13, no. 6, pp. 61–71, Dec. 2021, doi: 10.5815/ijitcs.2021.06.05.

[83] M. Elgendi *et al.*, "The use of photoplethysmography for assessing hypertension," *npj Digit. Med.*, vol. 2, no. 1, p. 60, Jun. 2019, doi: 10.1038/s41746-019-0136-7.

[84] D. Castaneda, A. Esparza, M. Ghamari, C. Soltanpur, and H. Nazeran, "A review on wearable photoplethysmography sensors and their potential future applications in health care," *IJBSBE*, vol. 4, no. 4, 2018, doi: 10.15406/ijbsbe.2018.04.00125.

[85] S. Kuntamalla and R. G. R. Lekkala, "Quantification of error between the heartbeat intervals measured form photoplethysmogram and electrocardiogram by synchronisation," *Journal of Medical Engineering & Technology*, vol. 42, no. 5, pp. 389–396, Jul. 2018, doi: 10.1080/03091902.2018.1513578.

[86] C. Lee, H. Sik Shin, and M. Lee, "Relations between ac-dc components and optical path length in photoplethysmography," *J. Biomed. Opt.*, vol. 16, no. 7, p. 077012, 2011, doi: 10.1117/1.3600769.

[87] N. Utami, A. W. Setiawan, H. Zakaria, T. R. Mengko, and R. Mengko, "Extracting blood flow parameters from Photoplethysmograph signals: A review," in *2013 3rd International Conference on Instrumentation, Communications, Information Technology and Biomedical Engineering (ICICI-BME)*, Bandung, Indonesia: IEEE, Nov. 2013, pp. 403–407. doi: 10.1109/ICICI-BME.2013.6698535.

[88] M. Elgendi, "On the Analysis of Fingertip Photoplethysmogram Signals," *CCR*, vol. 8, no. 1, pp. 14–25, Jun. 2012, doi: 10.2174/157340312801215782.

[89] J. Allen, "Photoplethysmography and its application in clinical physiological measurement," *Physiol. Meas.*, vol. 28, no. 3, pp. R1–R39, Mar. 2007, doi: 10.1088/0967-3334/28/3/R01.

[90] H. W. Loh *et al.*, "Application of photoplethysmography signals for healthcare systems: An in-depth review," *Computer Methods and Programs in Biomedicine*, vol. 216, p. 106677, Apr. 2022, doi: 10.1016/j.cmpb.2022.106677.

[91] M. Lokharan, K. C. Lokesh Kumar, V. Harish Kumar, N. Kayalvizhi, and R. Aryalekshmi, "Measurement of Pulse Transit Time (PTT) Using Photoplethysmography," in *The 16th International Conference on Biomedical Engineering*, vol. 61, J. Goh, C. T. Lim, and H. L. Leo, Eds., in IFMBE Proceedings, vol. 61. , Singapore: Springer Singapore, 2017, pp. 130–134. doi: 10.1007/978-981-10-4220-1_24.

[92] Q. Xie, G. Wang, Z. Peng, and Y. Lian, "Machine Learning Methods for Real-Time Blood Pressure Measurement Based on Photoplethysmography," in *2018 IEEE 23rd International Conference on Digital Signal Processing (DSP)*, Shanghai, China: IEEE, Nov. 2018, pp. 1–5. doi: 10.1109/ICDSP.2018.8631690.

[93] G. Slapničar, N. Mlakar, and M. Luštrek, "Blood Pressure Estimation from Photoplethysmogram Using a Spectro-Temporal Deep Neural Network," *Sensors*, vol. 19, no. 15, p. 3420, Aug. 2019, doi: 10.3390/s19153420.

[94] S. Shimazaki, H. Kawanaka, H. Ishikawa, K. Inoue, and K. Oguri, "Cuffless Blood Pressure Estimation from only the Waveform of Photoplethysmography using CNN," in *2019 41st Annual International Conference of the IEEE Engineering in Medicine and Biology Society (EMBC)*, Berlin, Germany: IEEE, Jul. 2019, pp. 5042–5045. doi: 10.1109/EMBC.2019.8856706.

[95] C. El Hajj and P. A. Kyriacou, "Cuffless and Continuous Blood Pressure Estimation From PPG Signals Using Recurrent Neural Networks," in *2020 42nd Annual International Conference of the IEEE Engineering in Medicine & Biology Society (EMBC)*, Montreal, QC, Canada: IEEE, Jul. 2020, pp. 4269–4272. doi: 10.1109/EMBC44109.2020.9175699.

[96] N. Ibtehaz *et al.*, "PPG2ABP: Translating Photoplethysmogram (PPG) Signals to Arterial Blood Pressure (ABP) Waveforms," *Bioengineering*, vol. 9, no. 11, p. 692, Nov. 2022, doi: 10.3390/bioengineering9110692.

[97] M. Kachuee, M. M. Kiani, H. Mohammadzade, and M. Shabany, "Cuff-less high-accuracy calibration-free blood pressure estimation using pulse transit time," in *2015 IEEE International Symposium on Circuits and Systems (ISCAS)*, Lisbon, Portugal: IEEE, May 2015, pp. 1006–1009. doi: 10.1109/ISCAS.2015.7168806.

[98] M. Kachuee, M. M. Kiani, H. Mohammadzade, and M. Shabany, "Cuffless Blood Pressure Estimation Algorithms for Continuous Health-Care Monitoring," *IEEE Trans. Biomed. Eng.*, vol. 64, no. 4, pp. 859–869, Apr. 2017, doi: 10.1109/TBME.2016.2580904.

[99] T. Athaya and S. Choi, "An Estimation Method of Continuous Non-Invasive Arterial Blood Pressure Waveform Using Photoplethysmography: A U-Net Architecture-Based Approach," *Sensors*, vol. 21, no. 5, p. 1867, Mar. 2021, doi: 10.3390/s21051867.

[100] K. Qin, W. Huang, and T. Zhang, "Deep generative model with domain adversarial training for predicting arterial blood pressure waveform from photoplethysmogram signal," *Biomedical Signal Processing and Control*, vol. 70, p. 102972, Sep. 2021, doi: 10.1016/j.bspc.2021.102972.

[101] W. Wang, L. Zhu, F. Marefat, P. Mohseni, K. Kilgore, and L. Najafizadeh, "Photoplethysmography-Based Blood Pressure Estimation Using Deep Learning," in *2020 54th Asilomar Conference on Signals, Systems, and Computers*, Pacific Grove, CA, USA: IEEE, Nov. 2020, pp. 945–949. doi: 10.1109/IEEECONF51394.2020.9443447.

[102] N. Maher, G. A. Elsheikh, W. R. Anis, and T. Emara, "Enhancement of blood pressure estimation method via machine learning," *Alexandria Engineering Journal*, vol. 60, no. 6, pp. 5779–5796, Dec. 2021, doi: 10.1016/j.aej.2021.04.035.

[103] Tjahjadi and Ramli, “Noninvasive Blood Pressure Classification Based on Photoplethysmography Using K-Nearest Neighbors Algorithm: A Feasibility Study,” *Information*, vol. 11, no. 2, p. 93, Feb. 2020, doi: 10.3390/info11020093.

[104] Y. Liang, Z. Chen, R. Ward, and M. Elgendi, “Photoplethysmography and Deep Learning: Enhancing Hypertension Risk Stratification,” *Biosensors*, vol. 8, no. 4, p. 101, Oct. 2018, doi: 10.3390/bios8040101.

[105] Y. Liang, Z. Chen, R. Ward, and M. Elgendi, “Hypertension Assessment via ECG and PPG Signals: An Evaluation Using MIMIC Database,” *Diagnostics*, vol. 8, no. 3, p. 65, Sep. 2018, doi: 10.3390/diagnostics8030065.

[106] E. O??Brien *et al.*, “The British Hypertension Society protocol for the evaluation of automated and semi-automated blood pressure measuring devices with special reference to ambulatory systems:,” *Journal of Hypertension*, vol. 8, no. 7, pp. 607–619, Jul. 1990, doi: 10.1097/00004872-199007000-00004.

[107] W. B. White *et al.*, “National standard for measurement of resting and ambulatory blood pressures with automated sphygmomanometers.,” *Hypertension*, vol. 21, no. 4, pp. 504–509, Apr. 1993, doi: 10.1161/01.HYP.21.4.504.

[108] S. Yang, W. S. W. Zaki, S. P. Morgan, S.-Y. Cho, R. Correia, and Y. Zhang, “Blood pressure estimation with complexity features from electrocardiogram and photoplethysmogram signals,” *Opt Quant Electron*, vol. 52, no. 3, p. 135, Mar. 2020, doi: 10.1007/s11082-020-2260-7.

[109] G. Thambiraj, U. Gandhi, U. Mangalanathan, V. J. M. Jose, and M. Anand, “Investigation on the effect of Womersley number, ECG and PPG features for cuff less blood pressure estimation using machine learning,” *Biomedical Signal Processing and Control*, vol. 60, p. 101942, Jul. 2020, doi: 10.1016/j.bspc.2020.101942.

[110] M. H. Chowdhury *et al.*, “Estimating Blood Pressure from the Photoplethysmogram Signal and Demographic Features Using Machine Learning Techniques,” *Sensors*, vol. 20, no. 11, p. 3127, Jun. 2020, doi: 10.3390/s20113127.

[111] City University of Hong Kong, Hong Kong SAR, China. He is now with the Department of Computer Science, Chu Hai College of Higher Education, Hong Kong SAR, China, M. Liu, L.-M. Po, and H. Fu, “Cuffless Blood Pressure Estimation Based on Photoplethysmography Signal and Its Second Derivative,” *IJCTE*, vol. 9, no. 3, pp. 202–206, 2017, doi: 10.7763/IJCTE.2017.V9.1138.

[112] Y.-C. Hsu, Y.-H. Li, C.-C. Chang, and L. N. Harfiya, “Generalized Deep Neural Network Model for Cuffless Blood Pressure Estimation with Photoplethysmogram Signal Only,” *Sensors*, vol. 20, no. 19, p. 5668, Oct. 2020, doi: 10.3390/s20195668.

[113] X. Xing and M. Sun, “Optical blood pressure estimation with photoplethysmography and FFT-based neural networks,” *Biomed. Opt. Express*, vol. 7, no. 8, p. 3007, Aug. 2016, doi: 10.1364/BOE.7.003007.

[114] S. Kuntamalla and R. G. R. Lekkala, “Quantification of error between the heartbeat intervals measured form photoplethysmogram and electrocardiogram by synchronisation,” *Journal of Medical Engineering & Technology*, vol. 42, no. 5, pp. 389–396, Jul. 2018, doi: 10.1080/03091902.2018.1513578.

[115] J. Li, Q. Ma, A. Hs. Chan, and S. S. Man, “Health monitoring through wearable technologies for older adults: Smart wearables acceptance model,” *Applied Ergonomics*, vol. 75, pp. 162–169, Feb. 2019, doi: 10.1016/j.apergo.2018.10.006.

[116] H. W. Loh *et al.*, “Application of photoplethysmography signals for healthcare systems: An in-depth review,” *Computer Methods and Programs in Biomedicine*, vol. 216, p. 106677, Apr. 2022, doi: 10.1016/j.cmpb.2022.106677.

[117] M. Ghamari, “A review on wearable photoplethysmography sensors and their potential future applications in health care,” *IJBSBE*, vol. 4, no. 4, 2018, doi: 10.15406/ijbsbe.2018.04.00125.

[118] L. N. Harfiya, C.-C. Chang, and Y.-H. Li, “Continuous Blood Pressure Estimation Using Exclusively Photopletysmography by LSTM-Based Signal-to-Signal Translation,” *Sensors*, vol. 21, no. 9, p. 2952, Apr. 2021, doi: 10.3390/s21092952.

[119] W. B. White *et al.*, “National standard for measurement of resting and ambulatory blood pressures with automated sphygmomanometers.,” *Hypertension*, vol. 21, no. 4, pp. 504–509, Apr. 1993, doi: 10.1161/01.HYP.21.4.504.

[120] S. Z. Li, *Pulse Diagnosis*. Paradigm Publications, 1985.

[121] D. Zhang, W. Zuo, D. Zhang, Y. Li, and N. Li, “Gaussian ERP Kernel Classifier for Pulse Waveforms Classification,” in *2010 20th International Conference on Pattern Recognition*, Istanbul, Turkey: IEEE, 2010, pp. 2736–2739. doi: 10.1109/ICPR.2010.670.

[122] D. Jia, D. Zhang, and N. Li, “Pulse Waveform Classification Using Support Vector Machine with Gaussian Time Warp Edit Distance Kernel,” *Computational and Mathematical Methods in Medicine*, vol. 2014, pp. 1–10, 2014, doi: 10.1155/2014/947254.

[123] J. Slark, M. S. Khan, P. Bentley, and P. Sharma, “Knowledge of blood pressure in a UK general public population,” *J Hum Hypertens*, vol. 28, no. 8, pp. 500–503, Aug. 2014, doi: 10.1038/jhh.2013.136.

[124] J. A. Wright-Nunes, J. M. Luther, T. A. Ikizler, and K. L. Cavanaugh, “Patient knowledge of blood pressure target is associated with improved blood pressure control in chronic kidney disease,” *Patient Education and Counseling*, vol. 88, no. 2, pp. 184–188, Aug. 2012, doi: 10.1016/j.pec.2012.02.015.

[125] Z. Liu *et al.*, “Multiclass Arrhythmia Detection and Classification From Photoplethysmography Signals Using a Deep Convolutional Neural Network,” *JAHA*, vol. 11, no. 7, p. e023555, Apr. 2022, doi: 10.1161/JAHA.121.023555.

[126] A. S. Al Fahoum, A. O. Abu Al-Haija, and H. A. Alshraideh, “Identification of Coronary Artery Diseases Using Photoplethysmography Signals and Practical Feature Selection Process,” *Bioengineering*, vol. 10, no. 2, p. 249, Feb. 2023, doi: 10.3390/bioengineering10020249.

[127] Chiang *et al.*, “Machine Learning Classification for Assessing the Degree of Stenosis and Blood Flow Volume at Arteriovenous Fistulas of Hemodialysis Patients Using a New Photoplethysmography Sensor Device,” *Sensors*, vol. 19, no. 15, p. 3422, Aug. 2019, doi: 10.3390/s19153422.

[128] H. G. Kang, S. Lee, H. U. Ryu, and Y. Shin, “Identification of Cerebral Artery Stenosis Using Bilateral Photoplethysmography,” *Journal of Healthcare Engineering*, vol. 2018, pp. 1–9, 2018, doi: 10.1155/2018/3253519.

[129] E.-S. Väliaho *et al.*, “Wrist Band Photoplethysmography Autocorrelation Analysis Enables Detection of Atrial Fibrillation Without Pulse Detection,” *Front. Physiol.*, vol. 12, p. 654555, May 2021, doi: 10.3389/fphys.2021.654555.

[130] M. Soltane, M. Ismail, and Z. A. Rashid, “Artificial Neural Network (ANN) Approach to PPG signal Classification,” *Int J Comput Inf Sci*, no. 2, pp. 58–65, 2004.

[131] Shobitha S, Sandhya R, Niranjana Krupa B, and Mohd. A. Mohd. Ali, “Recognizing cardiovascular risk from photoplethysmogram signals using ELM,” in *2016 Second International Conference on Cognitive Computing and Information Processing (CCIP)*, Mysuru, India: IEEE, Aug. 2016, pp. 1–5. doi: 10.1109/CCIP.2016.7802864.

[132] S. K. Prabhakar, H. Rajaguru, and S.-H. Kim, “Fuzzy-Inspired Photoplethysmography Signal Classification with Bio-Inspired Optimization for Analyzing Cardiovascular Disorders,” *Diagnostics*, vol. 10, no. 10, p. 763, Sep. 2020, doi: 10.3390/diagnostics10100763.

[133] M. A. Almarshad, M. S. Islam, S. Al-Ahmadi, and A. S. BaHammam, “Diagnostic Features and Potential Applications of PPG Signal in Healthcare: A Systematic Review,” *Healthcare*, vol. 10, no. 3, p. 547, Mar. 2022, doi: 10.3390/healthcare10030547.

[134] P. Wackel and B. Cannon, “Heart Rate and Rhythm Disorders,” *Pediatrics In Review*, vol. 38, no. 6, pp. 243–253, Jun. 2017, doi: 10.1542/pir.2016-0119.

[135] E. Mejía-Mejía, K. Budidha, T. Y. Abay, J. M. May, and P. A. Kyriacou, “Heart Rate Variability (HRV) and Pulse Rate Variability (PRV) for the Assessment of Autonomic Responses,” *Front. Physiol.*, vol. 11, p. 779, Jul. 2020, doi: 10.3389/fphys.2020.00779.

[136] S.-C. Fang, Y.-L. Wu, and P.-S. Tsai, “Heart Rate Variability and Risk of All-Cause Death and Cardiovascular Events in Patients With Cardiovascular Disease: A Meta-Analysis of Cohort Studies,” *Biological Research For Nursing*, vol. 22, no. 1, pp. 45–56, Jan. 2020, doi: 10.1177/1099800419877442.

[137] I. Goldenberg *et al.*, “Heart Rate Variability for Risk Assessment of Myocardial Ischemia in Patients Without Known Coronary Artery Disease: The HRV-DETECT (Heart Rate Variability for the Detection of Myocardial Ischemia) Study,” *JAHA*, vol. 8, no. 24, p. e014540, Dec. 2019, doi: 10.1161/JAHA.119.014540.

[138] Y. Kubota, L. Y. Chen, E. A. Whitsel, and A. R. Folsom, “Heart rate variability and lifetime risk of cardiovascular disease: the Atherosclerosis Risk in Communities Study,” *Annals of Epidemiology*, vol. 27, no. 10, pp. 619-625.e2, Oct. 2017, doi: 10.1016/j.annepidem.2017.08.024.

[139] C. Park and B. Lee, “Real-time estimation of respiratory rate from a photoplethysmogram using an adaptive lattice notch filter,” *BioMed Eng OnLine*, vol. 13, no. 1, p. 170, 2014, doi: 10.1186/1475-925X-13-170.

[140] R. Lei, B. W.-K. Ling, P. Feng, and J. Chen, “Estimation of Heart Rate and Respiratory Rate from PPG Signal Using Complementary Ensemble Empirical Mode Decomposition with both Independent Component Analysis and Non-Negative Matrix Factorization,” *Sensors*, vol. 20, no. 11, p. 3238, Jun. 2020, doi: 10.3390/s20113238.

[141] P. H. Charlton *et al.*, “Extraction of respiratory signals from the electrocardiogram and photoplethysmogram: technical and physiological determinants,” *Physiol. Meas.*, vol. 38, no. 5, pp. 669–690, May 2017, doi: 10.1088/1361-6579/aa670e.

[142] P. Dehkordi, A. Garde, B. Molavi, J. M. Ansermino, and G. A. Dumont, “Extracting Instantaneous Respiratory Rate From Multiple Photoplethysmogram Respiratory-Induced Variations,” *Front. Physiol.*, vol. 9, p. 948, Jul. 2018, doi: 10.3389/fphys.2018.00948.

[143] T. J. Cross, C.-H. Kim, B. D. Johnson, and S. Lalande, “The interactions between respiratory and cardiovascular systems in systolic heart failure,” *Journal of Applied Physiology*, vol. 128, no. 1, pp. 214–224, Jan. 2020, doi: 10.1152/japplphysiol.00113.2019.

[144] A. Mortara *et al.*, “Abnormal Awake Respiratory Patterns Are Common in Chronic Heart Failure and May Prevent Evaluation of Autonomic Tone by Measures of Heart Rate Variability,” *Circulation*, vol. 96, no. 1, pp. 246–252, Jul. 1997, doi: 10.1161/01.CIR.96.1.246.

[145] D. G. Brillante, A. J. O’sullivan, and L. G. Howes, “Arterial stiffness indices in healthy volunteers using non-invasive digital photoplethysmography,” *Blood Pressure*, vol. 17, no. 2, pp. 116–123, Jan. 2008, doi: 10.1080/08037050802059225.

[146] C. F. Clarenbach *et al.*, “Comparison of photoplethysmographic and arterial tonometry-derived indices of arterial stiffness,” *Hypertens Res*, vol. 35, no. 2, pp. 228–233, Feb. 2012, doi: 10.1038/hr.2011.168.

[147] N. Arnold *et al.*, “Relation between Arterial Stiffness and Markers of Inflammation and Hemostasis – Data from the Population-based Gutenberg Health Study,” *Sci Rep*, vol. 7, no. 1, p. 6346, Jul. 2017, doi: 10.1038/s41598-017-06175-2.

[148] I. García-López and E. Rodriguez-Villegas, “Extracting the Jugular Venous Pulse from Anterior Neck Contact Photoplethysmography,” *Sci Rep*, vol. 10, no. 1, p. 3466, Feb. 2020, doi: 10.1038/s41598-020-60317-7.

[149] R. Amelard *et al.*, “Non-contact hemodynamic imaging reveals the jugular venous pulse waveform,” *Sci Rep*, vol. 7, no. 1, p. 40150, Jan. 2017, doi: 10.1038/srep40150.

[150] E. J. Lam Po Tang, A. HajiRassouliha, M. P. Nash, P. M. F. Nielsen, A. J. Taberner, and Y. O. Cakmak, “Non-contact Quantification of Jugular Venous Pulse Waveforms from Skin Displacements,” *Sci Rep*, vol. 8, no. 1, p. 17236, Nov. 2018, doi: 10.1038/s41598-018-35483-4.

[151] A. V. Moço, L. Z. Mondragon, W. Wang, S. Stuijk, and G. De Haan, “Camera-based assessment of arterial stiffness and wave reflection parameters from neck micro-motion,” *Physiol. Meas.*, vol. 38, no. 8, pp. 1576–1598, Jul. 2017, doi: 10.1088/1361-6579/aa7d43.

[152] J. Cho and H. J. Baek, “A Comparative Study of Brachial–Ankle Pulse Wave Velocity and Heart–Finger Pulse Wave Velocity in Korean Adults,” *Sensors*, vol. 20, no. 7, p. 2073, Apr. 2020, doi: 10.3390/s20072073.

[153] D. Perpetuini *et al.*, “Photoplethysmographic Prediction of the Ankle-Brachial Pressure Index through a Machine Learning Approach,” *Applied Sciences*, vol. 10, no. 6, p. 2137, Mar. 2020, doi: 10.3390/app10062137.

[154] “Ankle Brachial Index Test,” JOHNS HOPKINS medicine. [Online]. Available: https://www.hopkinsmedicine.org/health/treatment-tests-and-therapies/ankle-brachial-index-test

[155] H. Miyashita, “The time is ripe to reevaluate the second derivative of the digital photoplethysmogram (SDPTG), originating in Japan, as an important tool for cardiovascular risk and central hemodynamic assessment,” *Hypertens Res*, vol. 40, no. 5, pp. 429–431, May 2017, doi: 10.1038/hr.2016.175.

[156] G. Baldoumas *et al.*, “A Prototype Photoplethysmography Electronic Device that Distinguishes Congestive Heart Failure from Healthy Individuals by Applying Natural Time Analysis,” *Electronics*, vol. 8, no. 11, p. 1288, Nov. 2019, doi: 10.3390/electronics8111288.

[157] Y. Kaneko *et al.*, “Cardiovascular Effects of Continuous Positive Airway Pressure in Patients with Heart Failure and Obstructive Sleep Apnea,” *N Engl J Med*, vol. 348, no. 13, pp. 1233–1241, Mar. 2003, doi: 10.1056/NEJMoa022479.

[158] F. Abnousi *et al.*, “A novel noninvasive method for remote heart failure monitoring: the EuleriAn video Magnification apPLications In heart Failure studY (AMPLIFY),” *npj Digit. Med.*, vol. 2, no. 1, p. 80, Aug. 2019, doi: 10.1038/s41746-019-0159-0.

[159] A. A. Kamshilin, V. V. Zaytsev, and O. V. Mamontov, “Novel contactless approach for assessment of venous occlusion plethysmography by video recordings at the green illumination,” *Sci Rep*, vol. 7, no. 1, p. 464, Mar. 2017, doi: 10.1038/s41598-017-00552-7.

[160] E. M. Green, R. Van Mourik, C. Wolfus, S. B. Heitner, O. Dur, and M. J. Semigran, “Machine learning detection of obstructive hypertrophic cardiomyopathy using a wearable biosensor,” *npj Digit. Med.*, vol. 2, no. 1, p. 57, Jun. 2019, doi: 10.1038/s41746-019-0130-0.

[161] Y. Sheu, “Illuminating the Black Box: Interpreting Deep Neural Network Models for Psychiatric Research,” *Front. Psychiatry*, vol. 11, p. 551299, Oct. 2020, doi: 10.3389/fpsyt.2020.551299.

[162] A. Ceni, “Random orthogonal additive filters: a solution to the vanishing/exploding gradient of deep neural networks.” arXiv, 2022. doi: 10.48550/ARXIV.2210.01245.

[163] Yangwei Liu and J. Xu, “One-pass online SVM with extremely small space complexity,” in *2016 23rd International Conference on Pattern Recognition (ICPR)*, Cancun: IEEE, Dec. 2016, pp. 3482–3487. doi: 10.1109/ICPR.2016.7900173.

[164] M. Hartwig, M. Gehrke, and R. Moller, “Approximate Query Answering in Complex Gaussian Mixture Models,” in *2019 IEEE International Conference on Big Knowledge (ICBK)*, Beijing, China: IEEE, Nov. 2019, pp. 81–86. doi: 10.1109/ICBK.2019.00019.

[165] E. Azeraf, E. Monfrini, and W. Pieczynski, “Improving Usual Naive Bayes Classifier Performances with Neural Naive Bayes based Models:,” in *Proceedings of the 11th International Conference on Pattern Recognition Applications and Methods*, Online Streaming, --- Select a Country ---: SCITEPRESS - Science and Technology Publications, 2022, pp. 315–322. doi: 10.5220/0010890400003122.

[166] D. R. Wilson and T. R. Martinez, “An Integrated Instance-Based Learning Algorithm,” *Computational Intelligence*, vol. 16, no. 1, pp. 1–28, Feb. 2000, doi: 10.1111/0824-7935.00103.

[167] Tjahjadi and Ramli, “Noninvasive Blood Pressure Classification Based on Photoplethysmography Using K-Nearest Neighbors Algorithm: A Feasibility Study,” *Information*, vol. 11, no. 2, p. 93, Feb. 2020, doi: 10.3390/info11020093.

[168] A. Andrzejak, F. Langner, and S. Zabala, “Interpretable models from distributed data via merging of decision trees,” in *2013 IEEE Symposium on Computational Intelligence and Data Mining (CIDM)*, Singapore, Singapore: IEEE, Apr. 2013, pp. 1–9. doi: 10.1109/CIDM.2013.6597210.

[169] M. Czajkowski, K. Jurczuk, and M. Kretowski, “Steering the interpretability of decision trees using lasso regression - an evolutionary perspective,” *Information Sciences*, vol. 638, p. 118944, Aug. 2023, doi: 10.1016/j.ins.2023.118944.

[170] D. Li and E. Kanoulas, “Bayesian Optimization for Optimizing Retrieval Systems,” in *Proceedings of the Eleventh ACM International Conference on Web Search and Data Mining*, Marina Del Rey CA USA: ACM, Feb. 2018, pp. 360–368. doi: 10.1145/3159652.3159665.

[171] J. H.-S. Wang, M.-H. Yeh, P. C.-P. Chao, T.-Y. Tu, Y.-H. Kao, and R. Pandey, "A fast digital chip implementing a real-time noise-resistant algorithm for estimating blood pressure using a non-invasive, cuffless PPG sensor," *Microsyst Technol*, vol. 26, no. 11, pp. 3501–3516, Nov. 2020, doi: 10.1007/s00542-020-04946-y.

[172] H. Shin and S. D. Min, "Feasibility study for the non-invasive blood pressure estimation based on ppg morphology: normotensive subject study," *BioMed Eng OnLine*, vol. 16, no. 1, p. 10, Dec. 2017, doi: 10.1186/s12938-016-0302-y.

[173] K. Takazawa and M. Fujita, "Clinical efficacy of the second derivative of a plethysmogram (accelerationplethysmogram)," *Journal of Cardiol*, vol. 23, pp. 207–217, 1993.

[174] P. S. Addison, "Slope Transit Time (STT): A Pulse Transit Time Proxy requiring Only a Single Signal Fiducial Point," *IEEE Trans. Biomed. Eng.*, vol. 63, no. 11, pp. 2441–2444, Nov. 2016, doi: 10.1109/TBME.2016.2528507.

[175] Q. Xie, G. Wang, Z. Peng, and Y. Lian, "Machine Learning Methods for Real-Time Blood Pressure Measurement Based on Photoplethysmography," in *2018 IEEE 23rd International Conference on Digital Signal Processing (DSP)*, Shanghai, China: IEEE, Nov. 2018, pp. 1–5. doi: 10.1109/ICDSP.2018.8631690.

[176] J. M. Ahn, "New Aging Index Using Signal Features of Both Photoplethysmograms and Acceleration Plethysmograms," *Healthc Inform Res*, vol. 23, no. 1, p. 53, 2017, doi: 10.4258/hir.2017.23.1.53.

[177] M. Ghamari, "A review on wearable photoplethysmography sensors and their potential future applications in health care," *IJBSBE*, vol. 4, no. 4, 2018, doi: 10.15406/ijbsbe.2018.04.00125.

[178] S. Meignen, T. Oberlin, and D.-H. Pham, "Synchrosqueezing transforms: From low- to high-frequency modulations and perspectives," *Comptes Rendus Physique*, vol. 20, no. 5, pp. 449–460, Jul. 2019, doi: 10.1016/j.crhy.2019.07.001.

[179] C. Mateo and J. A. Talavera, "Bridging the gap between the short-time Fourier transform (STFT), wavelets, the constant-Q transform and multi-resolution STFT," *SIViP*, vol. 14, no. 8, pp. 1535–1543, Nov. 2020, doi: 10.1007/s11760-020-01701-8.

[180] P. Flandrin, F. Auger, and E. Chassande-Mottin, "Time-Frequency Reassignment: From Principles to Algorithms," in *Applications in Time-Frequency Signal Processing*, 1st ed., A. Papandreou-Suppappola, Ed., CRC Press, 2018, pp. 179–204. doi: 10.1201/9781315220017-5.

[181] A. V. Chobanian *et al.*, "Seventh Report of the Joint National Committee on Prevention, Detection, Evaluation, and Treatment of High Blood Pressure," *Hypertension*, vol. 42, no. 6, pp. 1206–1252, Dec. 2003, doi: 10.1161/01.HYP.0000107251.49515.c2.

[182] A. E. W. Johnson *et al.*, “MIMIC-III, a freely accessible critical care database,” *Sci Data*, vol. 3, no. 1, p. 160035, May 2016, doi: 10.1038/sdata.2016.35.

[183] J. E. Cohen, R. A. Davis, and G. Samorodnitsky, “Heavy-tailed distributions, correlations, kurtosis and Taylor’s Law of fluctuation scaling,” *Proc. R. Soc. A.*, vol. 476, no. 2244, p. 20200610, Dec. 2020, doi: 10.1098/rspa.2020.0610.

[184] G. Thakur, “The Synchrosqueezing transform for instantaneous spectral analysis,” in *Excursions in Harmonic Analysis, Volume 4*, R. Balan, M. Begué, J. J. Benedetto, W. Czaja, and K. A. Okoudjou, Eds., in Applied and Numerical Harmonic Analysis. , Cham: Springer International Publishing, 2015, pp. 397–406. doi: 10.1007/978-3-319-20188-7_15.

[185] F. Auger *et al.*, “Time-Frequency Reassignment and Synchrosqueezing: An Overview,” *IEEE Signal Process. Mag.*, vol. 30, no. 6, pp. 32–41, Nov. 2013, doi: 10.1109/MSP.2013.2265316.

[186] M. Guerrero, O. Castillo, and M. García, “Cuckoo Search via Lévy Flights and a Comparison with Genetic Algorithms,” in *Fuzzy Logic Augmentation of Nature-Inspired Optimization Metaheuristics*, vol. 574, O. Castillo and P. Melin, Eds., in Studies in Computational Intelligence, vol. 574. , Cham: Springer International Publishing, 2015, pp. 91–103. doi: 10.1007/978-3-319-10960-2_6.

[187] C. Ding and H. Peng, “MINIMUM REDUNDANCY FEATURE SELECTION FROM MICROARRAY GENE EXPRESSION DATA,” *J. Bioinform. Comput. Biol.*, vol. 03, no. 02, pp. 185–205, Apr. 2005, doi: 10.1142/S0219720005001004.

[188] Y. Vivek and P. S. V. S. S. Prasad, “Scalable mRMR feature selection to handle high dimensional datasets: Vertical partitioning based Iterative MapReduce framework.” arXiv, 2022. doi: 10.48550/ARXIV.2208.09901.

[189] I. Jo, S. Lee, and S. Oh, “Improved Measures of Redundancy and Relevance for mRMR Feature Selection,” *Computers*, vol. 8, no. 2, p. 42, May 2019, doi: 10.3390/computers8020042.

[190] C. Ding and H. Peng, “MINIMUM REDUNDANCY FEATURE SELECTION FROM MICROARRAY GENE EXPRESSION DATA,” *J. Bioinform. Comput. Biol.*, vol. 03, no. 02, pp. 185–205, Apr. 2005, doi: 10.1142/S0219720005001004.

[191] S. K. Mandala, “XAI Renaissance: Redefining Interpretability in Medical Diagnostic Models.” arXiv, 2023. doi: 10.48550/ARXIV.2306.01668.

[192] N. Sani, J. Lee, R. Nabi, and I. Shpitser, “A Semiparametric Approach to Interpretable Machine Learning.” arXiv, 2020. doi: 10.48550/ARXIV.2006.04732.

[193] K. Elkhalil, A. Kammoun, R. Couillet, T. Y. Al-Naffouri, and M.-S. Alouini, "A Large Dimensional Study of Regularized Discriminant Analysis," *IEEE Trans. Signal Process.*, vol. 68, pp. 2464–2479, 2020, doi: 10.1109/TSP.2020.2984160.

[194] A. Karanikola, S. Karlos, V. Kazllarof, and S. Kotsiantis, "An incrementally updateable ensemble learner," in *Proceedings of the 22nd Pan-Hellenic Conference on Informatics*, Athens Greece: ACM, Nov. 2018, pp. 243–248. doi: 10.1145/3291533.3291536.

[195] H. Liu, A. Gegov, and M. Cocea, "Collaborative rule generation: An ensemble learning approach," *IFS*, vol. 30, no. 4, pp. 2277–2287, Mar. 2016, doi: 10.3233/IFS-151997.

[196] S. Zhang, "Challenges in KNN Classification," *IEEE Trans. Knowl. Data Eng.*, vol. 34, no. 10, pp. 4663–4675, Oct. 2022, doi: 10.1109/TKDE.2021.3049250.

[197] J. Wu, X.-Y. Chen, H. Zhang, L.-D. Xiong, H. Lei, and S.-H. Deng, "Hyperparameter Optimization for Machine Learning Models Based on Bayesian Optimization," vol. 17, no. 1, pp. 26–40, 2019, doi: 10.11989/JEST.1674-862X.80904120.

[198] B. Moody, G. Moody, M. Villarroel, G. Clifford, and I. Silva, "MIMIC-III Waveform Database." PhysioNet, 2017. doi: 10.13026/C2607M.

[199] Y. Liang, Z. Chen, G. Liu, and M. Elgendi, "A new, short-recorded photoplethysmogram dataset for blood pressure monitoring in China," *Sci Data*, vol. 5, no. 1, p. 180020, Feb. 2018, doi: 10.1038/sdata.2018.20.

[200] C. Orphanidou, "Quality Assessment for the Photoplethysmogram (PPG)," in *Signal Quality Assessment in Physiological Monitoring*, in SpringerBriefs in Bioengineering. , Cham: Springer International Publishing, 2018, pp. 41–63. doi: 10.1007/978-3-319-68415-4_3.

[201] Y. Liang, M. Elgendi, Z. Chen, and R. Ward, "An optimal filter for short photoplethysmogram signals," *Sci Data*, vol. 5, no. 1, p. 180076, May 2018, doi: 10.1038/sdata.2018.76.

[202] A. K. Singh, L. P. Gewali, and J. Khatiwada, "New Measures of Skewness of a Probability Distribution," *OJS*, vol. 09, no. 05, pp. 601–621, 2019, doi: 10.4236/ojs.2019.95039.

[203] P. Čisar and S. M. Čisar, "Skewness and Kurtosis in Function of Selection of Network Traffic Distribution," *Acta Polytechnica Hungarica*, vol. 7, no. 2, pp. 95–106, 2010.

[204] M. Elgendi, I. Norton, M. Brearley, D. Abbott, and D. Schuurmans, "Systolic Peak Detection in Acceleration Photoplethysmograms Measured from Emergency Responders in Tropical Conditions," *PLoS ONE*, vol. 8, no. 10, p. e76585, Oct. 2013, doi: 10.1371/journal.pone.0076585.

[205] A. R. Feinstein *et al.*, “Glossary of Cardiologic Terms Related to Physical Diagnosis Part IV. Arterial Pulses Committee on Standardized Terminology, American College of Cardiology and American Heart Association,” *Chest*, vol. 59, no. 6, pp. 671–672, Jun. 1971, doi: 10.1378/chest.59.6.671.

[206] M. F. O’Rourke, “The arterial pulse in health and disease,” *American Heart Journal*, vol. 82, no. 5, pp. 687–702, Nov. 1971, doi: 10.1016/0002-8703(71)90340-1.

[207] P. R. Fleming, “THE MECHANISM OF THE PULSUS BISFERIENS,” *Heart*, vol. 19, no. 4, pp. 519–524, Oct. 1957, doi: 10.1136/hrt.19.4.519.

[208] J. K. Perloff, “The Arterial Pulse,” in *Physical Examination of the Heart and Circulation*, Fourth edition., SHELTON: PEOPLE’S MEDICAL PUBLISHING HOUSE, 2009, pp. 55–92.

[209] H. Ikram, P. G. F. Nixon, and J. A. Fox, “THE HAeMODYNAMIC IMPLICATIONS OF THE BISFERIENS PULSE,” *Heart*, vol. 26, no. 4, pp. 452–459, Jul. 1964, doi: 10.1136/hrt.26.4.452.

[210] C. A. Pickett, J. L. Jackson, B. A. Hemann, and J. E. Atwood, “Carotid Artery Examination, An Important Tool in Patient Evaluation:,” *Southern Medical Journal*, vol. 104, no. 7, pp. 526–532, Jul. 2011, doi: 10.1097/SMJ.0b013e31821e9493.

[211] E. Roter and A. Y. Denault, “Radial artery reliability using arterial Doppler assessment prior to arterial cannulation,” *Can J Anesth/J Can Anesth*, vol. 66, no. 10, pp. 1272–1273, Oct. 2019, doi: 10.1007/s12630-019-01443-3.

[212] M. E. Safar, S. St Laurent, A. L. Safavian, B. M. Pannier, and G. M. London, “Pulse Pressure in Sustained Essential Hypertension: A Haemodynamic Study:,” *Journal of Hypertension*, vol. 5, no. 2, pp. 213–218, Apr. 1987, doi: 10.1097/00004872-198704000-00013.

[213] J. Seladi-Schulman and K. Weiss, “Pulse Pressure Calculation Explained,” Healthline. Accessed: Apr. 28, 2023. [Online]. Available: https://www.healthline.com/health/pulse-pressure

[214] G. M. Boiteau, A. J. Libanoff, and B. J. Allenstein, “Upstroke time ratio in valvular aortic insufficiency,” *The American Journal of Cardiology*, vol. 14, no. 2, pp. 162–168, Aug. 1964, doi: 10.1016/0002-9149(64)90127-4.

[215] T. Nagai, Y. Tabara, M. Igase, J. Nakura, T. Miki, and K. Kohara, “Migraine Is Associated with Enhanced Arterial Stiffness,” *Hypertens Res*, vol. 30, no. 7, pp. 577–583, 2007, doi: 10.1291/hypres.30.577.

[216] J. Suvarna, “Watson’s water hammer pulse,” *J Postgrad Med*, vol. 54, no. 2, p. 163, 2008, doi: 10.4103/0022-3859.40791.

[217] A. L. Galabin, “On the Causation of the Water-Hammer Pulse, and its Transformation in Different Arteries as Illustrated by the Graphic Method,” *Med Chir Trans.*, vol. MCT-59, no. 1, pp. 361–388, Jan. 1876, doi: 10.1177/095952877605900122.

[218] S. R. McGee, “Aortic Regurgitation,” in *Evidence-based physical diagnosis*, 4th edition., Philadelphia, PA: Elsevier, 2018, pp. 385–392.

[219] J.-H. Bae and Y. J. Jeon, “Pulse sharpness as a quantitative index of vascular aging,” *Sci Rep*, vol. 11, no. 1, p. 19895, Oct. 2021, doi: 10.1038/s41598-021-99315-8.

[220] M. J. Frank, “The Clinical Evaluation of Aortic Regurgitation: With Special Reference to a Neglected Sign: the Popliteal-Brachial Pressure Gradient,” *Arch Intern Med*, vol. 116, no. 3, p. 357, Sep. 1965, doi: 10.1001/archinte.1965.03870030037008.

[221] J. W. Linhart, “Aortic Regurgitation: Clinical, Hemodynamic, Surgical, and Angiographic Correlations,” *The Annals of Thoracic Surgery*, vol. 11, no. 1, pp. 27–37, Jan. 1971, doi: 10.1016/S0003-4975(10)65410-0.

[222] C. A. Warnes, P. C. Harris, and H. W. Fritts, “Effect of elevating the wrist on the radial pulse in aortic regurgitation: Corrigan revisited,” *The American Journal of Cardiology*, vol. 51, no. 9, pp. 1551–1553, May 1983, doi: 10.1016/0002-9149(83)90675-6.

[223] N. Yoshioka *et al.*, “Do radial arterial pressure curves have diagnostic validity for identify severe aortic stenosis?,” *J Anesth*, vol. 24, no. 1, pp. 7–10, Feb. 2010, doi: 10.1007/s00540-009-0837-1.

[224] C. M. Halley and B. P. Griffin, “Physical Examination in Valvular Heart Disease,” in *Valvular Heart Disease*, A. Wang and T. M. Bashore, Eds., Totowa, NJ: Humana Press, 2009, pp. 73–92. doi: 10.1007/978-1-59745-411-7_4.

[225] A. T. Askari and A. W. Messerli, Eds., *Cardiovascular Hemodynamics: An Introductory Guide*. in Contemporary Cardiology. Cham: Springer International Publishing, 2019. doi: 10.1007/978-3-030-19131-3.

[226] J. C. O’Shea and R. M. Califf, “24-Hour ambulatory blood pressure monitoring,” *American Heart Journal*, vol. 151, no. 5, pp. 962–968, May 2006, doi: 10.1016/j.ahj.2005.03.020.

[227] G. Parati and H. Schumacher, “Blood pressure variability over 24 h: prognostic implications and treatment perspectives. An assessment using the smoothness index with telmisartan–amlodipine monotherapy and combination,” *Hypertens Res*, vol. 37, no. 3, pp. 187–193, Mar. 2014, doi: 10.1038/hr.2013.145.

[228] R. C. Orchard and E. Craige, “Dicrotic pulse after open heart surgery.,” *Circulation*, vol. 62, no. 5, pp. 1107–1114, Nov. 1980, doi: 10.1161/01.CIR.62.5.1107

[229] M. Elgendi, “Optimal Signal Quality Index for Photoplethysmogram Signals,” *Bioengineering*, vol. 3, no. 4, p. 21, Sep. 2016, doi: 10.3390/bioengineering3040021.